Engineered, Functional, Human Microvasculature in a Perfusable Fluidic Device

by

Jordan Ari Whisler

B.S. Mechanical Engineering (2009), Washington University in St. Louis
S.M. Mechanical Engineering (2013), M.I.T.

Submitted to the Department of Mechanical Engineering
in Partial Fulfillment of the Requirements for the Degree of

Doctor of Philosophy in Mechanical Engineering

at the

MASSACHUSETTS INSTITUTE OF TECHNOLOGY

September 2017

Signature of Author: Signature redacted
Department of Mechanical Engineering
August 03, 2017

Certified by: Signature redacted
Roger D. Kamm
Professor of Mechanical Engineering
Professor of Biological Engineering
Thesis Supervisor

Accepted by: Signature redacted
Rohan Abeyaratne
Professor of Mechanical Engineering
Graduate Officer

Engineered, Functional, Human Microvasculature in a Perfusable Fluidic Device

by

Jordan Ari Whisler

Submitted to the Department of Mechanical Engineering
on August 03, 2017 in Partial Fulfillment of the Requirements for the Degree of

Doctor of Philosophy in Mechanical Engineering

ABSTRACT

Engineered, human tissue models will enable us to study disease more accurately, and develop treatments more economically, than ever before. Functional tissue grown in the laboratory will also provide a much-needed source for the clinical replacement of diseased or damaged tissues. A major hindrance to the development of these technologies has been the inability to vascularize tissue-engineered constructs, resulting in limited size and biological complexity.

In this thesis, we report the development of a novel 3D fluidic platform for the generation of functional, human, microvasculature. Using different fabrication methods, we developed both a micro-fluidic system (0.1 – 1 mm tissue dimensions) – used for high throughput disease modeling assays, and a meso-fluidic system (1 – 10 mm tissue dimensions) – for generating removable tissue-engineered constructs. These systems were validated by their successful use in a metastasis model - to elucidate the mechanism of cancer cell extravasation, and in the formation of a vascularized, perfusable tissue construct containing pancreatic islets, respectively.

Vascularization, in our system, was achieved by encapsulating endothelial cells in a 3D fibrin matrix and relying on their inherent ability to collectively self-assemble into a functional vasculature – as they do during embryonic development. To better understand and characterize this process, we measured the morphological, functional, mechanical, and biological properties of the tissue as they emerged during vascular morphogenesis. We found that juxtacrine interactions between endothelial cells and fibroblasts enhanced the functionality and stability of the newly formed vasculature – as characterized via vascular permeability and gene expression. Under optimal co-culture conditions, the tissue stiffness increased 10-fold, mainly due to organized cellular contraction. Additionally, over the course of 2-weeks, the cells deposited over 50 new extracellular matrix (ECM) proteins, accounting for roughly 1/3 of the total ECM.

These results shed light on the mechanisms underlying vascular morphogenesis and will be useful in further developing vascularization strategies for tissue engineering and regenerative medicine applications.

Key words:
Tissue Engineering, Vascularization, Microfluidics, *In Vitro* Model

Thesis Advisor:
Roger D. Kamm, Professor of Mechanical and Biological Engineering, MIT

Thesis Committee Members:
Harry Asada, Professor of Mechanical Engineering, MIT
Linda Griffith, Professor of Biological Engineering, MIT
Kara McCloskey, Professor of Engineering, UC Merced

Acknowledgements

Thank you first and foremost to my thesis advisor, Professor Roger D. Kamm, whose unwavering support enabled me to complete this work. I consider it a great privilege to have had the opportunity to learn from a world-renowned researcher and scientist of his caliber. His kindness and care for each individual student is boundless.

One of the benefits of being Roger's student has been access to the expansive network of collaborators that he has cultivated. Of the many collaborators I have been fortunate to work with, I would like to especially thank the following people who directly contributed to the work in this thesis: Hesham Azizgolshani, Michelle Chen, Emad Moeendarbary, Andrea Malandrino, Amanda Del Rosario, Michelle Griffin, Kunle Demuren, Vincent Butty, and Marianna Sofman.

Thank you to the members of my cohort – Vivek Sivathanu and Ran Li – for your contributions to my successful completion of this degree. I deeply value the scientific and personal relationships we have developed over these years.

I can say with confidence that the two people most responsible for my accomplishments are my parents. Mom and Dad – thank you for instilling within me the values of hard work and perseverance and having the utmost confidence in me every step of the way.

My dear wife – Rena. I dedicate this thesis to you. Thank you for standing with me and supporting me as I completed this project while we began a project of our own. Your unconditional love and encouragement have been invaluable. Only now do I understand the saying, "What is mine, and what is yours, is hers."

Table of Contents

Introduction

Engineered, human tissue models will enable us to study disease more accurately, and develop treatments more economically, than ever before. Functional tissue grown in the laboratory will also provide a much-needed source for the clinical replacement of diseased or damaged tissues. A major hindrance to the development of these technologies has been the inability to vascularize tissue-engineered constructs, resulting in their limited size and biological complexity. The objective of this thesis was to engineer functional, lab grown microvascular tissue by (1) developing a quantitative, 3D microfluidic platform to study the effects of environmental inputs on the formation of microvascular networks, and (2) use the acquired knowledge to engineer scaled up (> 1mm) constructs for use in tissue engineering applications.

In **Chapter 1**, we present the relevant biological background information and describe the natural methods employed by the body to form vasculature *in vivo*. We also survey the current state of the art in engineered microvascular models, focusing on their ability to accurately replicate the physiological properties of the microvasculature.

Readers are directed to the author's Master's thesis[1] and related publication[2] for the full description of a microfluidic platform we developed to study the effects of environmental factors on microvascular network formation. Specifically, we quantified the effects of cell seeding density, extracellular matrix composition, and angiogenic growth factors on the morphological properties of self-assembled microvasculature. These results subsequently served as a guide for controlling the morphological characteristics of engineered microvasculature in our scaled-up, tissue-engineering platform. The microfluidic model was also incorporated into a 3D cancer metastasis assay for the study of tumor cell extravasation[3,4].

Using the above system, our research focused on the effects of external, environmental cues on vascularization. Vascular morphogenesis, however, is a dynamic process in which new functional, mechanical, biological, and chemical properties emerge through intrinsic cell-cell and cell-matrix interactions from within the system. To study these tissue level properties, we re-designed the platform to be compatible with standard mechanical and biological assays. The new, scaled up, 'meso'-fluidic device enabled real-time, 3D visualization of vascular network formation in a perfusable system – similar to the micro-fluidic version,

but also provided two key additional features, namely: (1) removal of the intact tissue to perform mechanical testing, and (2) sufficient cell and matrix yield per sample to perform transcriptional and proteomic analysis, respectively.

The increased height of the meso-fluidic device from 0.1 to 1 mm, resulted in improved 3-dimensional distribution of the vasculature. This necessitated the development of fully 3D morphological and functional quantification methods, something lacking from previous studies with *in vitro*, engineered microvascular models. In **Chapter 2**, we present these methods and their use to quantify vascular morphology – vessel diameters and lengths, and vascular function – perfusability and permeability.

In **Chapter 3**, we examined the heterotypic cell-cell interactions between endothelial cells (ECs) and fibroblasts (FBs) that promote enhanced vascular morphogenesis and stabilization. Comparing the effects of paracrine vs. juxtacrine interactions between the two cell types, we identified that physical interaction (juxtacrine) was necessary to achieve peak enhancement. With this optimal configuration, the engineered vasculature remained viable and functional throughout 3 weeks of culture, and its permeability approached the values measured for *in vivo* microvasculature.

As vascular morphogenesis progressed, we observed an increase in the rigidity and structural integrity of the tissue. To quantify these changes in mechanical properties, we measured the tissue stiffness with atomic force microscopy (AFM). These results are presented in **Chapter 4**. We found that the tissue stiffness increased 10-fold with respect to its value at day 1. We determined that the increase was due to contributions from active cellular force generation, passive cellular material properties, and stiffening of the ECM.

In **Chapter 5**, we further examined the structural and compositional changes that occur in the ECM. Confocal reflectance microscopy revealed thick bundles of ECM fibers aligned along the surface of the vessels that likely contribute to the observed matrix stiffening. We then performed mass spectrometry on the decellularized matrix and identified the presence of over 50 proteins that were synthesized and deposited by the cells.

In **Chapter 6**, we present the results of transcriptional analysis, obtained by isolating and sequencing the RNA of ECs or FBs at different stages of vascular morphogenesis. These results shed light on the internal biological programs associated with the properties

measured in previous chapters. Specifically, we found that inhibition of the inflammatory response correlates with vascular stability in ECs, and that heterotypic cell-cell interactions promote the onset of a contractile vascular smooth muscle phenotype in FBs.

Finally, in **Chapter 7**, we lay out our future plans to develop this system into a constant perfusion, organ specific, patient specific model of the microvasculature based on successful proof of concept experiments with a custom designed flow system, pancreatic islets, and human induced pluripotent stem cells (IPSCs).

1 Background

1.1 Mechanisms of Microvasculature Formation In vivo

The formation of vasculature *in vivo* occurs mainly through one of two mechanisms: vasculogenesis or angiogenesis. Vasculogenesis accounts for the initial vascular plexus that forms in the developing embryo. It involves the differentiation of precursor cells within isolated 'blood islands' into endothelial cells and their subsequent migration and collective assembly into a functional vascular network.

At later developmental stages and throughout adult life, new vessels are formed from pre-existing ones through the process of angiogenesis. In angiogenesis, environmental cues initiate the activation of an endothelial tip cell that locally degrades the interstitial extracellular matrix as it migrates away from its parent vessel. The tip cell is followed by stalk endothelial cells, which proliferate and migrate to form the new vessel wall. Finally, pericytes are recruited to stabilize the new sprout as it anastomoses with the existing vasculature to convey blood flow.

Both processes result from the coordinated integration of signals initiated through the binding of soluble growth factors and extracellular matrix (ECM) ligands, interactions with accessory cells, and exposure to physical forces. For in-depth reviews of the molecular mechanisms governing vasculogenesis, angiogenesis, and vessel maturation *in vivo*, see Risau and Flamme[5] , Risau[6], and Jain[7], respectively.

Microvascular formation was first recapitulated i*n vitro* by simply plating capillary endothelial cells on a two-dimensional substrate. Folkman and Haudenschild[8] that endothelial cells (EC) self-assembled into interconnected tubular structures and developed lumens by the formation and fusion of intracellular vacuoles. Montesano and Orci[9] later plated ECs on the surface of a 3D collagen gel and observed invasion of angiogenic sprouts into the underlying matrix. Davis and colleagues[10] have performed systematic studies of ECs undergoing lumen formation and tubulogenesis in 3D hydrogels to uncover the specific matrix-integrin interactions[11], signaling transduction pathways[12] and gene expression profiles[13] responsible for these processes *in vitro*. For a comprehensive review of *in vitro* models of vasculogenesis and angiogenesis, see Vailhe et. al.[14].

1.2 Microfluidic Microvascular Models (MMMs)

1.2.1 Microfluidic Platform - Hardware

Microfluidic platforms provide additional advantages for the study and modeling of microvasculature, not available in standard *in vitro* assays. These include the geometric patterning of ECM and various cell types, the ability to visualize vascular formation in real-time, and significantly – the ability to perfuse the vasculature and perform functional studies.

A microfluidic device for microvascular modeling typically consists of an array of hollow channels formed within a transparent and biocompatible 3D substrate (Figure 1-1). The channels are engineered with cross-sectional dimensions on the order of 100 microns and are filled with combinations of cells, hydrogel, and growth media. PDMS is the most commonly used substrate material because it is inexpensive, and can be shaped to a mold by simple polymerization at elevated temperature. However, because drugs and other small molecules are readily absorbed by PDMS, it can be advantageous to use other suitable materials such as hard plastics.

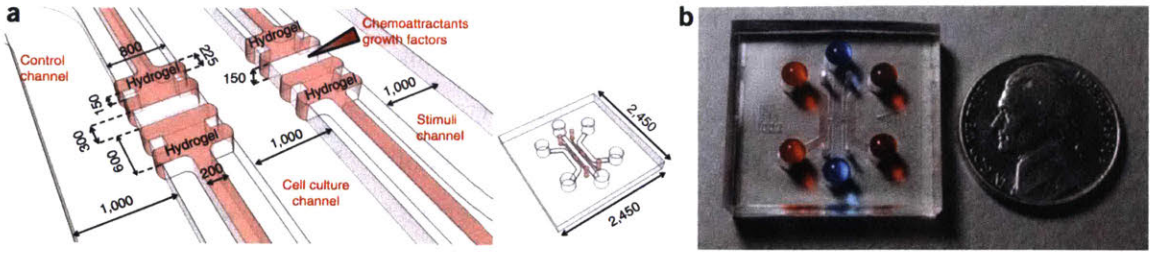

Figure 1-1 Typical PDMS based device used for microfluidic microvascular models. (a) Diagram of a device with multiple medium and hydrogel channels in parallel; units in microns. (b) Photograph of the device from (a) filled with medium (red and blue liquid) and hydrogel (pink). Reprinted from[15].

Figure 1-2 demonstrates the manufacturing and assembly process involved for a typical microfluidic microvascular platform - a detailed protocol can be found in Shin et. al.[15]. Briefly, a mold is created with raised features corresponding to the hollow microfluidic channels. PDMS is polymerized around the mold and when peeled off, the hollow channels are exposed. Media and gel filling ports are punched through the top of the device to provide external access to the cell culture region. A glass coverslip is then bonded to the bottom of the device to enclose the channels and allow for visualization with a microscope. Cells, pre-polymerized hydrogel solution, and growth media are introduced into the device through their respective ports and are kept in adjacent channels through the use of surface tension. Finally, the device can be connected to a flow system to maintain chemical gradients or apply shear flow through the vasculature during culture.

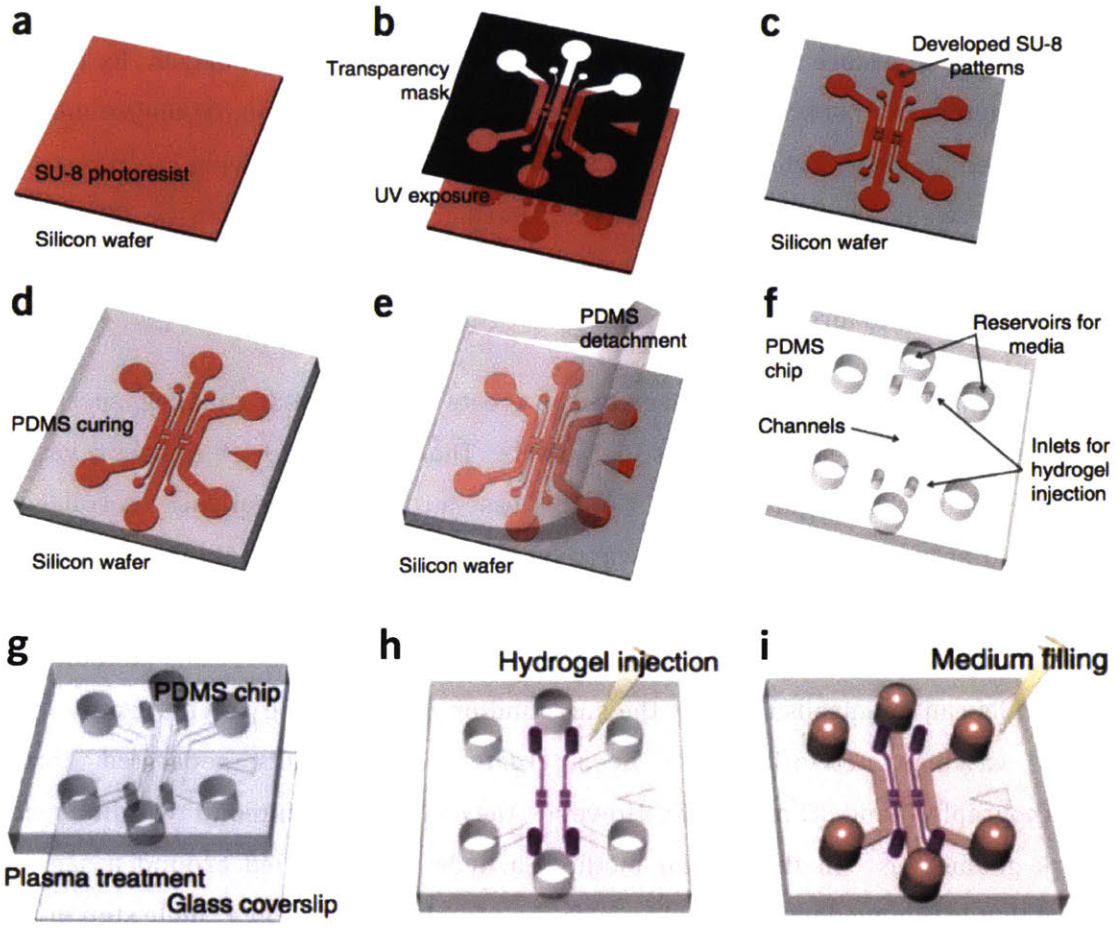

Figure 1-2 Schematic of microfluidic device fabrication and assembly. (a-c) Raised pattern of microfluidic channels formed on a silicon wafer by photo-curing of SU-8 to create positive mold. (d-e) PDMS poured over the mold, cured, and peeled off to reveal open channels. (f) Gel filling and medium ports punched through PDMS. (g) Plasma surface treatment and bonding of PDMS to glass coverslip. (h) Pre-polymer hydrogel injection into gel channels. (i) Growth medium injection into medium channels after hydrogel polymerization. Adapted from[15].

1.2.2 Methods of Microvasculature Formation

1.2.2.1 Engineered Methods

Coated Channel

The coated channel method for microfluidic microvascular engineering involves seeding endothelial cells on to the walls of microfabricated vascular channels[16–18] (Fig1-3a). ECM

proteins such as collagen[19], fibronectin[20-24] or gelatin[25] have been used to coat the inorganic channel surface to ensure the formation of a confluent endothelial monolayer. By inserting a porous membrane between two adjacent microfluidic channels, individual monolayers can be seeded on either side to form a bi-layer vessel wall while studying the transport of molecules between the two chambers[21,24]. Alternatively, hydrogel can be filled into a channel adjacent to the vascular channel and endothelial cells seeded as a monolayer on the gel-media interface to form the vessel wall[26,27].

Two general methods have been developed to create microvascular channels surrounded entirely by a three-dimensional interstitial matrix. The first method[28-31] utilizes a vascular mold similar to above Figure 1-2c, but in this case an ECM hydrogel such as collagen is polymerized around the mold and the vascular channels are formed upon its removal. A second layer of hydrogel is then assembled to the bottom of the first layer to enclose the vascular channels before seeding with endothelial cells. An advantage of this method is that stromal cells can be encapsulated in the surrounding matrix during polymerization. Also, complex vascular networks have been created using molds generated through photolithography[32] and 3D printing[33]. However, they have been limited to two-dimensional network geometries. In the second method, a hydrogel is formed around a sacrificial material that is removed or dissolved to form the vascular channels in a single step process. Cylindrical objects such a needle[34-40], glass capillary[41,42], or fiber[43,44] can be removed to form channels with circular cross sections. Using stereo-lithography with a photopolymer[45,46], or 3D printing with a carbohydrate-glass ink[47], complex three-dimensional vascular templates have been fabricated to form interconnected vascular channels in a 3D hydrogel when dissolved.

The introduction of endothelial cells and subsequent formation of a confluent monolayer is a critical step when using the coated channel method. After seeding, the cells are typically cultured for 2-3 days before performing experiments[27,38,41]. Methods developed to achieve uniform cell seeding include injection of the cell suspension under constant slow flow conditions[22], and rotation of the device during multiple cell seedings[43], or both[38]. A novel method to achieve instantaneous and uniform monolayer formation is the cell electrochemical detachment approach, or CED[48-50]. In this variation of the sacrificial method, an EC monolayer is first formed around a gold rod that is coated with an electro-

sensitive peptide. After hydrogel is polymerized around the rod, an electrical potential is applied to release the peptides and monolayer, transferring them to the hydrogel surface.

A major limitation of the coated channel method has been the inability to model small vessels of the microcirculation such as capillaries, which typically have diameters smaller than 10 microns. This is due, in part, to the limitation of many current technologies to fabricate features smaller than 100 microns. Additionally, it is difficult to form an endothelial monolayer in channels less than 30 microns in diameter because cells aggregate and plug the channel during seeding. Linville et. al.[39] found that applying reverse flow after the initial cell seeding induced ECs to migrate and form a monolayer along the length of the channel for diameters as low as 20 microns. They also reported chemical, mechanical, and physical cues that aid in stabilizing the monolayer once it has formed.

1.2.2.2 Natural Methods

Sprouting

Microfluidic models of capillary scale microvasculature have been achieved by recapitulating the physiological processes of vascularization described earlier. Using any of the coated channel methods in which the endothelium is surrounded by hydrogel, ECs can be induced to sprout into the surrounding interstitial matrix through stimulation with angiogenic growth factors[51-55] (Figure 1-3b). In a three channel microfluidic device with hydrogel in the middle channel, ECs seeded on the surface of the gel formed sprouts with patent lumens that spanned the entire length of the gel and could be readily perfused[56-58]. An advantage of this method is that sprouting occurs in the horizontal plane, making it easy to image the sprout dynamics in real time. Alternatively, ECs formed into spheroids[59-62] (Figure 1-3d) or seeded on the surface of micro-carrier beads[63,64] (Figure 1-3c) and encapsulated within the hydrogel can be induced to sprout and form interconnected networks. Use of the sprouting method to form functional microvasculature is limited by the speed of sprout growth, which is typically on the order of 100 microns per day.

Self-Assembly

The self-assembly method[3,65-72] resembles the *in vivo* process of vasculogenesis. Although biologically complex, this method is experimentally straightforward. Vascular cells are

homogeneously dispersed and encapsulated within a hydrogel channel (Figure 1-3e). Soluble and insoluble signaling transmitted through growth factors in the medium and ECM ligands, respectively, activates the inherent ability of ECs to elongate, connect, and form intracellular vacuoles that coalesce to form vascular lumens. This entire process occurs within 96 hours and results in functional, perfusable microvasculature. Initial seeding density is an important factor that determines the ability of ECs to self-assemble as well as the resulting microvascular morphology[72]. Typical seeding densities used are on the order of millions of ECs per milliliter of hydrogel. Also of significant consequence are the mechanical and biochemical properties of the hydrogel. For both the self-assembly and sprouting methods, cells must be able to degrade, migrate through, and adhere to the 3D matrix.

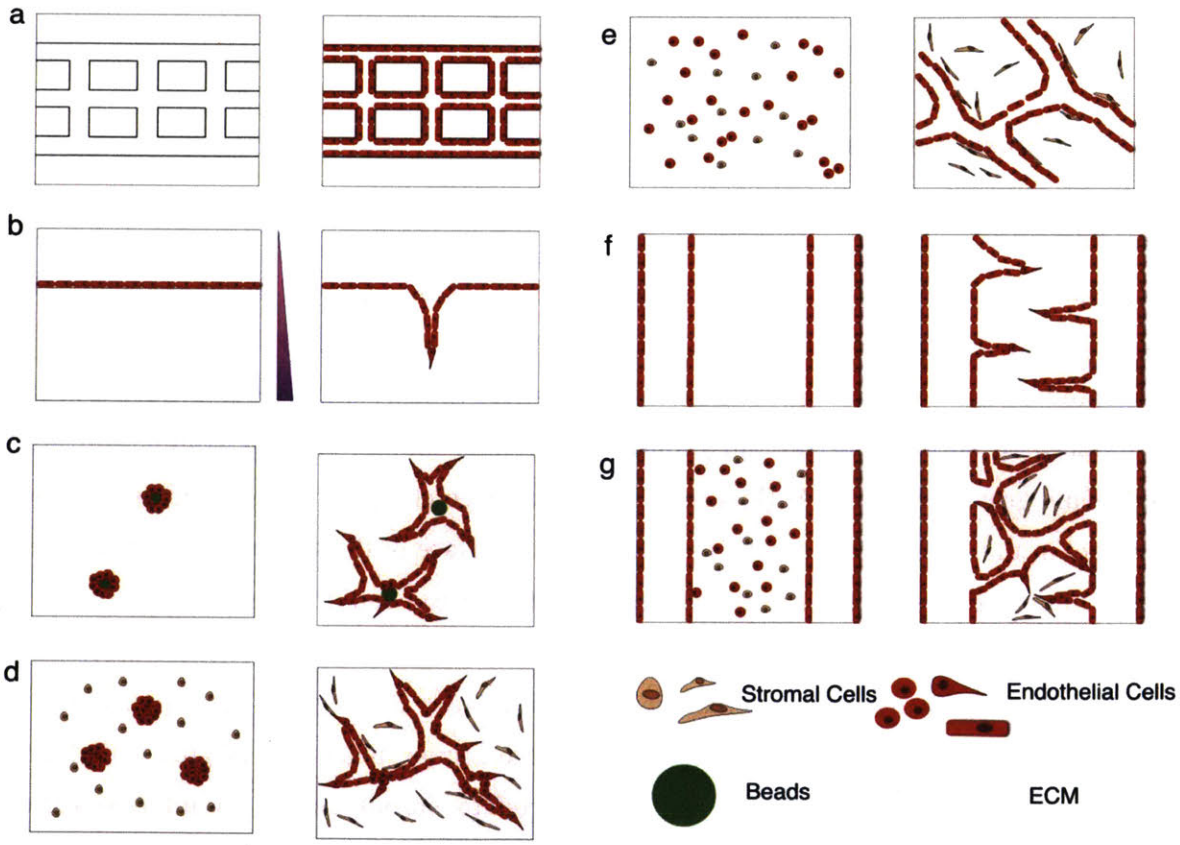

Figure 1-3 Methods of microfluidic microvasculature formation. (a) coated channel, (b) angiogenic sprouting with a growth factor gradient, (c) sprouting from EC coated beads, (d) sprouting from EC spheroids, (e) self-assembly, (f) coated channel + sprouting, (g) coated channel + sprouting + self-assembly.

1.2.2.3 Method Selection

The sprouting and self-assembly methods generate microvasculature that morphologically resembles their *in vivo* counterparts, with small diameters and complex network structures. These processes are, however, inherently stochastic and the resulting vasculature contains morphologic variability. The inability to precisely control characteristics such as vessel diameter and length can confound parametric studies of vascular function. Additionally, the complex network geometries make it difficult to analyze and predict flow profiles for perfusion studies – especially when compared to the simple, well-defined geometries associated with the coated channel methods.

Therefore, factors such as ease of fabrication, time required for vascularization, and desired vascular morphology will help determine the appropriate microvascular microfluidic platform for a given application. In some instances it is desirable to combine multiple methods within a single platform as has been done with coated-channel and sprouting [32,48,49](Figure 1-3f), coated-channel and self-assembly[47], sprouting and self-assembly[73], and a combination of all three methods[50] (Figure 1-3g).

Until this point, we have discussed the strategies and hardware that enable microvascular microfluidic modeling. The following sections explore, in detail, the individual biological components – cells, matrix, and growth factors – used in these systems to create physiologically representative microvasculature.

1.2.3 Biological/Biochemical Components

Vessel Wall – Structure and Composition

In general, the blood vessel wall is composed of three layers (Figure 1-4): the tunica intima – a single layer of endothelial cells resting on a basement membrane; the tunica media – an elastin rich elastic layer containing contractile vascular smooth muscle cells; and the tunica adventitia – a collagenous loose connective tissue containing resident fibroblasts. The relative contributions of each layer vary depending on the vessel type. The smallest vessels of the microvasculature – capillaries – comprise only a tunica intima and are surrounded by

mural cells – pericytes and smooth muscle cells – that regulate vessel diameter and permeability.

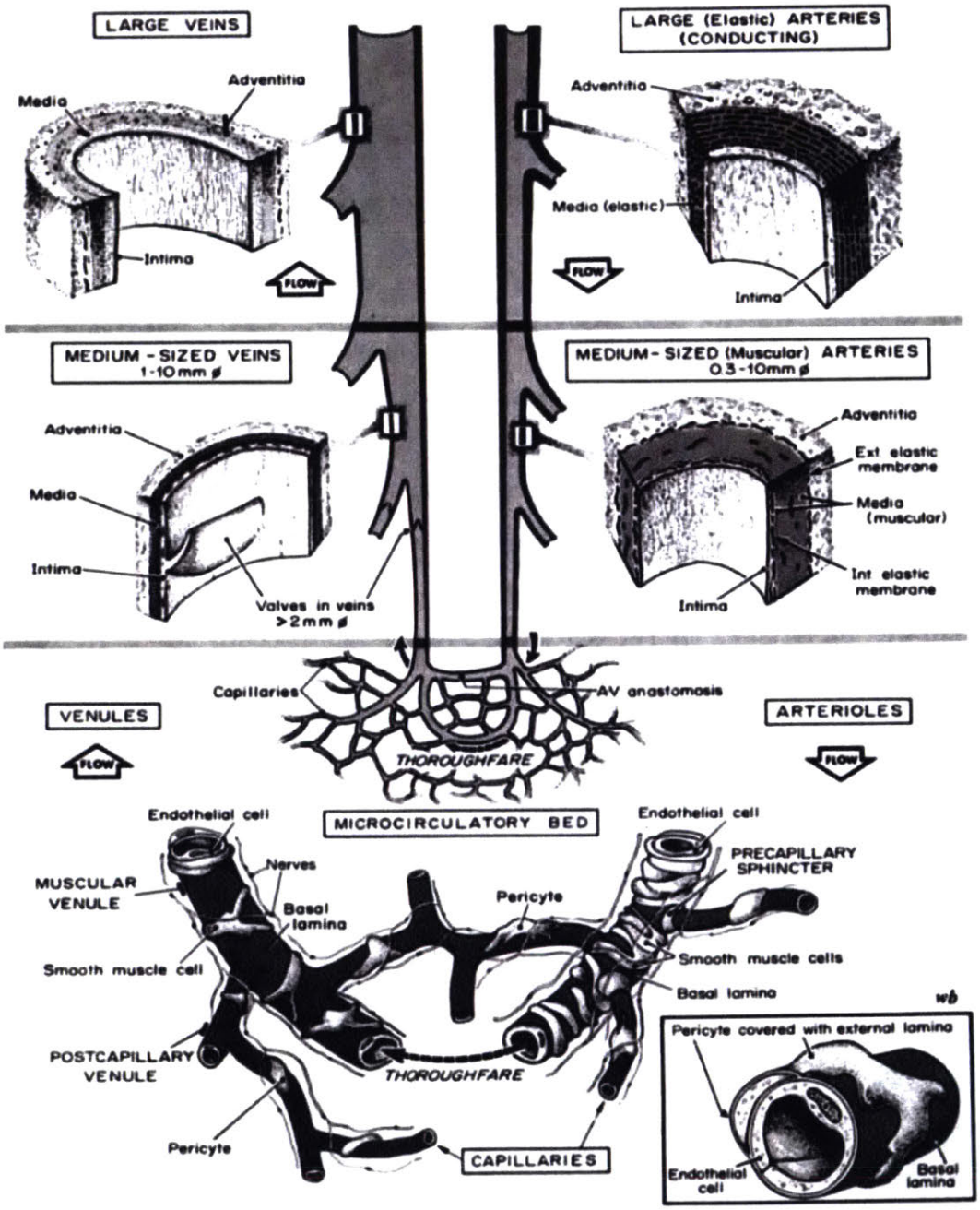

Figure 1-4 Schematic of blood vessel wall architecture and composition. Reprinted from[74].

1.2.3.1 Cells

Endothelial Cells

Endothelial cells (ECs) line the interior of all blood vessels. Their properties give rise to many of the vessel's functions - including permeability, hemostasis, trafficking of circulating cells, and tissue homeostatsis[75]. They are typically identified by expression of VEGF receptors flk-1 (VEGF-R2) and flt-1 (VEGF-R1), intercellular junction proteins VE-cadherin (CD144) and PECAM-1 (CD31), and the blood coagulation factor - vWF.

ECs originate from angioblasts in the mesoderm that differentiate into the specialized ECs of the arteries, veins, or capillaries. Capillary ECs then further differentiate to acquire organ specific phenotypes[76]. These phenotypic variations – manifested in distinct transcriptional and protein expression profiles[77,78] - lead to functional differences in the vessels they comprise, such as permeability, response to cytokine exposure, ability to attract homing immune cells, and tumor cell adhesion affinity[79,80].

Thus, it is important to consider the specific phenotype of ECs used for MMMs. Indeed, ECs obtained from various sources were found to differ *in vitro* in their ability to form vascular networks[81], and in their response to drugs[60] or specific cytokines[82]. Human umbilical vein ECs (HUVEC) were the first EC to be successfully cultured *in vitro* and thus are commonly used in MMMs due to their extensive characterization[83] and their relative ease of procurement. Several groups have used vessel and organ specific ECs to accurately model *in vivo* vascular phenotype and function – including artery[43,60], vein[60], brain[84], lung [43,63,71], and kidney[28].

MMMs have also been generated using ECs derived from adult endothelial progenitor cells (EPC) [66,69,82,85-90], or induced pluripotent stem cells (IPSC)[68,91]. The former can be isolated from bone marrow[92] or periphery blood[93] and the latter from urine samples[94] or skin biopsies[95]. They can be further differentiated into vessel and organ specific ECs[96]. Thus, stem-cell derived ECs could potentially be used to create organ and patient-specific MMMs without the need for invasive isolation procedures such as those required for primary cells.

It is important to note that the vessel and organ specificity of ECs results from both inherited epigenetic modifications and local environmental cues. When removed from their native environment and cultured *in vitro*, vessel specific ECs partially de-differentiate[77,97].

However, there is evidence that their phenotypes can be maintained in MMMs by properly recreating the biochemical, mechanical, and physical environment they experience *in vivo* [98,99].

Mural Cells

Pericytes

Pericytes (PC) are perivascular cells that directly contact and share a basement membrane with the endothelium of microvessels. They contribute to vessel stability by providing mechanical support, synthesizing ECM and basement membrane, and secreting growth factors – most notably Angiopoetin-1 (Ang-1)[100] – that regulate EC phenotype. They help regulate perfusion - by transmitting contractile forces to the vessels and secreting vasoactive chemicals - and also reduce vessel permeability[101]. PCs are often found covering inter-endothelial junctions, and can thus regulate the passage of transmigrating leukocytes or cancer cells[102,103].

The area fraction of pericyte coverage varies from 10-70% depending on the location of a capillary bed, with higher coverage correlating to lower permeability[100]. In the retina, there is one PC for every EC, while the PC:EC ratio in skeletal muscle is as low as 1:100[101]. Even at low ratios, PCs extend protrusions that can span multiple ECs and vessels, enabling them to coordinate signaling across the vasculature[104]. They physically integrate into the vessel endothelium through peg and socket junctions – in which PCs insert cytoplasmic extensions into EC invaginations, adherens junctions, and gap junctions – allowing direct contact between the cytoplasm of the two cell types[101].

During vasculogenesis, PCs differentiate from mesenchymal stem cells (MSCs) and are attracted to the newly formed vessels through paracrine PDGF-β signaling[105]. They express the markers: PDGFR-β, NG2 – a proteoglycan, and α-SMA. PCs also play a significant role in angiogenesis. The initiation of a sprout coincides with detachment of PCs and their basement membrane from the parent vessel, while recruitment of PCs to the newly forming vessel prevents its regression[106].

As with ECs, PCs exhibit tremendous phenotypic heterogeneity and organ specificity.

Several groups have incorporated PCs from various sources into MMMs, including brain[32,73], placenta[57,107-110], lung[71], skeletal muscle[81], retina[81], and embryonic stem cell derived PCs [111]. In a sprouting assay, Kim et. al.[57] formed a monolayer of HUVEC and placental PCs, and induced sprouting into a fibrin gel via paracrine signaling from either dermal or lung fibroblasts. They found that PCs from the monolayer wrapped around the newly formed vessels. Inclusion of PCs led to denser, more branched and interconnected networks of vessels. Significantly, PC investment reduced vessel diameter and permeability – both signatures of PC functionality *in vivo*. Bichsel et. al.[71] cultured lung microvascular ECs together with lung PCs in fibrin gel in a self-assembly assay, and similarly found that PC co-culture reduced both vessel diameter and permeability. PCs directly contacting the endothelium expressed higher levels of α-SMA, suggesting differentiation towards a contractile phenotype. Treatment with phenylephrine – a vasoconstrictor – further reduced the vessel diameters through a PC dependent mechanism.

Vascular Smooth Muscle Cells

Vascular smooth muscle cells (VSMC) are contractile mural cells typically associated with larger vessels. They share a common lineage with PCs but express high levels of proteins associated with the contractile phenotype, including α-SMA, SMMHC (smooth muscle myosin heavy chain), SM22, and smoothelin – a distinct marker of SMCs[112]. VSMCs regulate blood pressure through contraction and relaxation, and provide structural support to the vessel[113]. In the large arteries, where pressures are significant, up to 40 layers of VSMCs are necessary to carry out these mechanical functions, whereas 1-2 layers are sufficient in the smaller arterioles[114]. VSMCs can transition from a contractile to a synthetic phenotype – in which they proliferate, migrate, and secrete ECM – this usually occurs in response to injury [113]. Excess ECM production by VSMCs causes an increase in vessel wall stiffness that can lead to hypertension and related vascular diseases[115].

VSMCs of the tunica media have been incorporated into MMMs mainly through a variation of the coated channel technique. They are either (1) encapsulated in a hydrogel surrounding an endothelialized channel (2) or seeded as a monolayer on the channel surface[116]. In an example of the former, Hasan et. al.[34] formed perfusable multilayer vessels in a PDMS microfluidic device by sequentially seeding cell-laden GelMA hyrdrogels around

concentric needles. An outer adventitia with fibroblasts was first formed, followed by a media containing aortic SMCs, and finally a monolayer of ECs was seeded to coat the lumen. Inner diameters of 120-400 microns were achieved and the wall thickness and mechanical properties of each layer could be tuned. Yoshida et. al.[117] utilized the latter approach to form perfusable multilayer vessels within a synthetic γ-PGA hydrogel. Hollow channels of 720 microns were seeded with umbilical artery SMCs followed by a HUVEC monolayer. A fibronectin-gelatin (FN-G) nanofilm coating was deposited between the two cell monolayers to ensure efficient and uniform adhesion. The bilayer vessel wall was found to significantly decrease diffusion of BSA into the surrounding gel. Finally, the hydrogel was degraded to obtain free-standing, intact, perfusable vessels that could be useful for future tissue engineering applications. In a unique approach, Barreto-Ortiz et. al.[107] formed free-standing arterioles with diameters ranging from 100-500 microns by sequentially seeding ECs and then VSMCs around a fibrin tube. The fibrin tube was then degraded to expose the vessel lumen. VSMCs were found to deposit collagen and elastin – the two major ECM components of the tunica media.

Stromal Cells

Fibroblasts

Fibroblasts (FB) comprise a general class of mesenchymal stromal cells[118] that are characterized by the lack markers for other specifically differentiated cells[119]. They are present in the stroma of all tissues, and therefore interact with vessels of every type and size through secretion of paracrine signaling factors - notably IL-6, IL-8, HGF, and TGF-β[120]. Their main function is to synthesize, secrete, and regulate the stromal ECM - mostly collagen - which gives mechanical structure to a tissue or organ. In response to biochemical and mechanical stimulants resulting from a wound, FBs can acquire an activated myofibroblast phenotype in which they become proliferative and migratory, produce excessive amounts ECM, and actively contract the wound[121]. It has been suggested that the act of isolating FBs initiates their wound healing response and thus all FBs cultured *in vitro* are of the activated, rather than stable, phenotype[122].

FBs play a role in many diseases. They can promote inflammation, tumor growth, and angiogenesis through the secretion of cytokines, and also physically interact with cancer or immune cells that have extravasated and entered the tissue stroma[123]. Irregular matrix production can lead to fibrosis or heart disease[124].

Stromal cells - in particular FBs - have been shown to play an important role in the formation and maintenance of microvessels in MMMs. In the absence of FBs, ECs sprouting from a monolayer migrate independently and fail to form stable capillaries[125], while ECs dispersed in a hydrogel elongate to form nascent networks that subsequently regress [72]. In a sprouting assay, Newman et. al.[126] showed that the pro-angiogenic and stabilizing effects of FBs resulted from the secretion of growth factors - that interacted directly with ECs, and proteins - that incorporated into, and modified, the ECM.

FBs from different anatomical sources show phenotypic heterogeneity[127] and support vascularization in MMMs to varying degrees. In a sprouting assay, Kim et. al.[128] found that normal human lung fibroblasts (NHLF) induced HUVEC to form vascular networks that were more dense than those formed with dermal fibroblasts (DF), whereas DFs better facilitated pericyte coverage of the vessels. Shamis et. al.[129] differentiated FBs from ESCs and IPSCs and showed that they promoted more robust and uniform vascularization than did foreskin FBs, likely through elevated secretion of angiogenic growth factors, and adoption of a pericyte-like phenotype.

Mesenchymal Stem Cells

Mesenchymal stem cells (MSC) are stromal cells that can differentiate into bone, fat, cartilage, or muscle cells. They exhibit many of the same morphologic and phenotypic characteristics as activated fibroblasts, and some suggest that the two cell types are not distinct[130-132]. Indeed, the phenotypic boundaries between many of the mural and stromal cells important to the vasculature are fluidly defined and trans-differentiation between them has been observed. For example, pericytes differentiate from MSCs during embryogenesis, and are phenotypically similar to VSMCs. FBs are also capable of differentiating into VSMCs[121]. It is therefore plausible that a single pluripotent stromal cell type could be induced with the right environmental cues to differentiate into the various vascular support cells *in vitro*.

In a self-assembly assay, Jeon et. al.[67] found that bone-marrow derived MSCs (BM-MSC) promoted the formation of vascular networks, then co-localized with the microvessels and began expressing α-SMA. Several groups have observed a similar phenomenon in which FBs (NHLF) take on the role of both stromal and mural cells in MMMs[85,133].

1.2.3.2 Exctracellular Matrix

Blood vessels are embedded within the stromal extracellular matrix (ECM) - a porous meshwork of proteins and polysaccharides - that provides structural support and biochemical signaling cues to surrounding cells. The composition of ECM varies depending on the functional requirements - both mechanical and biological - of a given tissue. The most abundant ECM protein, collagen 1, forms a fibrous structural scaffold that imparts mechanical strength to the tissue, while elastin provides elasticity, and hyaluronan resists compressive loading[121,134]. Other, less abundant components, such as fibronectin, play a significant role in cell signaling - either through direct interactions with cells that in part influence cell migration, proliferation, survival and differentiation, or by sequestering soluble cytokines that locally guide cellular behavior[134].

Reconstituted hydrogels with varying concentrations of collagen[135], fibronectin[51,108,109,136], or hyaluronan[89] have been used to support vessels in MMMs. To more accurately model the native ECM composition, Nagao et. al.[28] used decellularized human ECM from kidney (kECM) as a 3D template to form perfusable vessels. They found that kidney peritubular microvascular ECs seeded on kECM assumed a more quiescent phenotype than when seeded on collagen 1.

The physical properties of ECM hydrogels also influence the vasculature in MMMs. Ghajar et. al.[133] found that increasing ECM density inhibited angiogenic sprouting indirectly by decreasing the scaffold porosity and limiting the diffusion of angiogenic growth factors. Alternatively, by varying the extent of crosslinking while keeping the protein concentration constant, gel stiffness can be controlled independently of ligand density. Using this and other similar methods, stiffness has been shown to affect the ability of ECs to self assemble into vascular networks[137], form angiogenic sprouts[62,138], and maintain a stable monolayer [139,140].

The ECM must be able to maintain structural stability while exposed to cell induced forces. Fibrin gels seeded with skeletal muscle myoblasts, ECs and FBs collapsed on themselves – inhibiting the formation of vasculature – unless the gels were incorporated into stiff PLLA/PLGA scaffolds[141]. Rao et. al.[142] found that incorporating hydroxyapatite particles in unconstrained hydrogels recovered the formation of vasculature despite gel contraction.

Synthetic hydrogels provide a means to engineer ECMs with tunable mechanical and biochemical properties with the ability to independently control the density of polymer, cross-linker, and bioactive peptides[47,143]. PEG gels are biologically inert, but the inclusion of MMP degradable cross-linkers allows ECs to form the voids necessary to elongate and form networks, while synthetic RGD peptides enable cell adhesion and provide the proper signaling for vacuole and lumen formation[89,91].

Specialized ECMs play a significant role with regard to the vasculature in the contexts of development, vessel quiescence, and wound healing. During embryogenesis, the ECM - predominantly composed of fibronectin and hyaluronan - is highly conducive to vasculogenesis[144].

After the formation of a nascent vasculature, ECs synthesize and secrete ECM components that self-organize into the basement membrane (BM). The BM is a 100 nm thick sheet of ECM that mechanically supports blood vessels, assists the maintenance of proper EC apical/basal polarity, functions as a barrier to extravasating cells, shields the endothelium from the underlying stromal matrix, and induces a quiescent phenotype[145-147]. It is composed of a thin layer of laminin that coats the surface of the endothelium and a dense, highly cross-linked collagen IV scaffold that supports other proteins and glycoproteins – namely, nidogens and heparin sulfate proteoglycans[148]. Roughly 50 proteins make up the BM, but collagen accounts for half of its weight[149]. Han et. al.[150] replicated the BM by coating a thin layer of matrigel on the surface of a collagen channel before seeding HMVEC. This induced a stable EC phenotype and reduced the vessel permeability. Even without an exogenous supply, ECs *in vitro* have been found to lay down their own BM[57,107] and this effect is enhanced by the presence of pericytes[151].

In response to injury, platelet aggregation at the site of a wound induces the formation of a fibrin clot – a provisional matrix of fibrin and fibronectin that induces robust vascularization. Fibroblasts recruited to the clot, later replace it with a more stable

collagenous matrix. This mechanism may also play a role in angiogenesis, where increased vessel permeability allows leakage of clot forming factors into the interstitial matrix prior to the induction of sprouting[152]. Thus, fibrin is commonly used in MMMs to induce sprouting[56,57,63] or the self-assembly of vascular networks[66,67,82].

1.2.3.3 Soluble Factors

The local composition – concentrations and gradients – of soluble biochemical factors plays an important role in controlling vascular phenotype. For example, the growth factors (GF) Ang-1 and TGF-β1 are known to promote EC quiescence and vessel maturity. VEGF and FGF are necessary for EC survival, but at elevated levels, they lead to increased permeability and the formation of angiogenic sprouts[7,153]. *In vivo*, these factors – and others – are delivered to the vessel by the systemic circulation and also secreted locally by stromal and parenchymal cells. In MMMs, they must be supplied by the growth medium (GM). EGM-2 (Lonza) – the GM most commonly used for MMMs - contains the GFs VEGF, FGF, EGF, IGF, and 2% serum, and is optimized to promote a proliferative EC phenotype. Additional GFs have been used to induce angiogenic sprouting (VEGF[16]), enhance the self-assembly of vascular networks (HGF[136]), and control blood vessel morphology (S1P[72]). It is important to note that serum contributes unknown quantities of many GFs to the medium and thus limits the ability to control its overall composition. To address this, the Davis lab[154] and others[155] developed defined, serum-free medium formulations for MMMs.

Identifying a GM formulation that indefinitely maintains stable vasculature *in vitro* remains an elusive goal. An alternative approach has been to rely on stromal cells to secrete GFs that promote vascular stability – a function they perform *in vivo*. These cells have been encapsulated in separate hydrogels[3,56] or alginate beads[61,109] to physically isolate them from the vasculature while still permiting paracrine communication through the diffusion of soluble factors. Interestingly, the stabilizing effects could not be reproduced with conditioned medium[129,156], suggesting that bilateral communication between the stroma and vasculature is required. Additional GFs regulate the interactions between vascular and stromal cells. Lim et. al.[157], used S1P to enhance the stabilizing effect of FBs on vascular sprouts, and Jeon et. al.[67], added Ang-1 to promote MSC induced vascular maturation.

Combining multiple cell types in an MMM necessitates finding a medium formulation that supports them all. This can be especially difficult for the case of organ specific models with specialized parenchymal cells or stem cells that are sensitive to specific GFs. It is generally accomplished by forming mixtures of the media of the most sensitive cells[65,70,158]. Knowledge of a defined, serum free medium for each of the cell types could enable the formulation of a combined medium with the minimum necessary components.

1.2.4 Organ Specific MMMs

Combinations of organ specific vascular cells, ECM, and parenchymal cells have been used in MMMs to model the specialized vasculature in bone[49,65,159], brain[36,88], heart [16,31,160,161], liver [16,47], kidney[28,29], lung[71], muscle[20,141,159,162,163], pancreas[164] and tumor[38,56,85,165] tissues. As expected, the incorporation of parenchymal cells affects vascular morphology and function. Signaling from tumor cells was found to increase angiogenic sprouting[165] and vessel permeability[38,56]. In another study[159], vessels were formed in the presence of bone or muscle cells and exhibited differences in barrier function - namely permeability and the ability of cancer cells to extravasate.

Just as the parenchyme influences vascular function, the vasculature promotes the optimal phenotype and functionality of its host organ. Therefore, the vasculature can be considered an integral component of any organ-on-a-chip. Incorporation of vascular networks enhanced the differentiation of osteoblasts and osteoclasts in a bone regeneration model [166], and improved the morphology and tissue level organization of cardiomyocytes in a cardiac tissue model[31]. At the functional level, engineered vasculature promoted enhanced insulin production of islets in a pancreas model[164], and urea production of hepatocytes in a liver model[16].

The spatial organization of blood vessels within an organ and their juxtaposition to parenchymal cells – such as in the kidney glomerulus, hepatic lobule, or lung alveolus – is also critical to their function. Thus, the inclusion of organ specific cell types and materials is necessary but likely not sufficient to model organ specific vasculature. Self-assembly of these components into complex patterns is not presently reliable, and in some instances the inclusion of parenchymal cells even inhibits the formation of vasculature[158].

Micromachining methods[29] and novel 3D patterning techniques[167,168] have been used to engineer geometrically complex and physiologically accurate vasculature in MMMs.

1.2.5 Applications

Microfluidic MMMs provide an ideal platform to study the mechanisms underlying vascular formation and function in a controlled and systematic manner. The ability to (1) culture vascular cells in well defined 3D environments, (2) control the mechanical and biochemical properties of ECM hydrogels, (3) introduce known concentrations of individual molecules, (4) and apply physiological forces and flows - combined with the ability to quantitatively measure morphological and functional vascular responses to these inputs - has enabled studies whose findings have contributed vastly to our scientific understanding of the vasculature.

By inducing pathological responses, MMMs have been used to study the mechanisms of vascular disease. Kohn et. al.[26], modeled the intimal stiffening of aging blood vessels by modulating the stiffness of the underlying matrix. They found that increased stiffness inhibited the endothelium's normal response to shear stress and enabled the development of atherosclerosis. Zheng et. al.[32,169] modeled thrombosis by chemically stimulating the endothelium of perfusable vascular networks and introducing whole blood. They found that clotting was highly dependent on vascular geometry and corresponding flow patterns. Lewis et. al.[22] modeled the hypoxic vascular wound site by controlling oxygen and shear stress levels and studied their effects on the homing of endothelial progenitor cells.

The vasculature plays a central role in cancer, and MMMs have been used to model tumor angiogenesis[165], as well as tumor cell intravasation[27,41,165], adhesion[23,41], and extravasation [3,41,159].

Because of their ability to accurately model healthy and diseased vasculature, MMMs have proven to be a valuable tool for drug testing and screening. They have been used to identify novel compounds and determine optimal dosages of drugs to treat hyper-permeable [24,56] or constricted vessels[25], inhibit angiogenesis[60], and disrupt the tumor vasculature[85]. In a microfluidic model of tumor dispersion, Bai et. al.[170] found that the presence of blood

vessels indirectly modulated the affects of anti-EMT drugs on tumor spheroids, thus demonstrating the importance of considering secondary effects of the vasculature on drug efficacy in organotypic models[16]. To better integrate these assays with standard pharmaceutical screening technology, Phan et. al.[171] arranged multiple independent vascularized micro-organs on a 96-well plate, potentially allowing for automated processing and analysis.

Findings from MMM studies have also led directly to the development of vascularized implantable tissue constructs and regenerative medicine therapies [46,70,89,90,109,142,172]. However, we have limited our discussion here to purely *in vitro* studies.

2 Fluidic Platform for 3D Vascular Morphogenesis

2.1 Introduction

To systematically study the emergent properties of vascular morphogenesis, we designed an *in vitro* 3D culture platform to satisfy the following criteria: **(i)** high resolution, real-time imaging of both cellular and matrix components, **(ii)** vascular perfusion for functional studies, **(iii)** physical access to intact tissue for mechanical testing, **(iv)** isolation of cells for gene regulation analysis, and **(v)** isolation of matrix for protein analysis. Combining these functionalities, for the first time, gave us the unique ability to holistically study the morphological, functional, mechanical, and biological properties of an individual tissue sample at various stages of vascular development.

2.2 Results

2.2.1 Vascular Morphogenesis

To fulfill the above criteria, we designed and fabricated a PDMS fluidic device comprising three adjacent and parallel channels (Figure 2-1); See methods for dimensions and fabrication details). ECs and FBs were encapsulated together in a fibrin hydrogel in the

middle channel – the "Tissue Vascularization Channel". The two side channels – "Perfusion Channels" – were filled with growth medium to support tissue growth and survival and were also used to convect flow through the tissue after the formation of vasculature. A coverglass bonded to the bottom of the device enabled direct observation of vascular morphogenesis in real time.

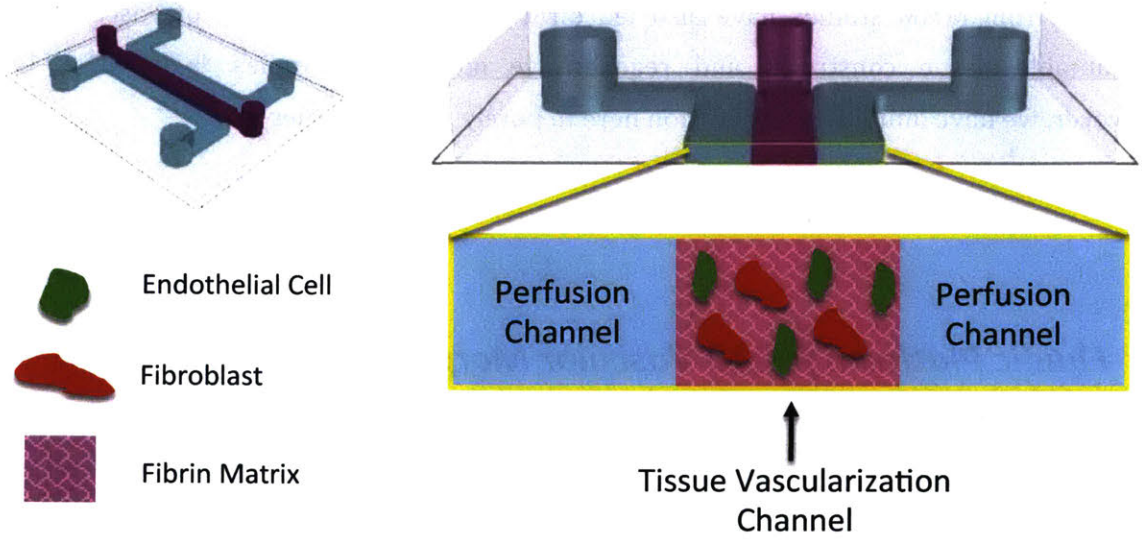

Figure 2-1 Fluidic device for 3D vascular morphogenesis. 3 channel PDMS-device bonded to a glass coverslip for visualization. Endothelial cells and fibroblasts encapsulated in fibrin matrix in central vascularization channel. Growth medium supplied in side perfusion channels.

Over the course of one week, we observed profound morphological changes at both the cellular and tissue levels (Figure 2-2). At the tissue level, ECs – initially rounded and mono-dispersed – spread out, extended protrusions that developed into intercellular connections, and formed an interconnected, perfusable network by day 4. Over the next 3 days, the overall network structure remained stable while individual vessel branches continued to mature, forming smooth vessel boundaries with well-defined lumens.

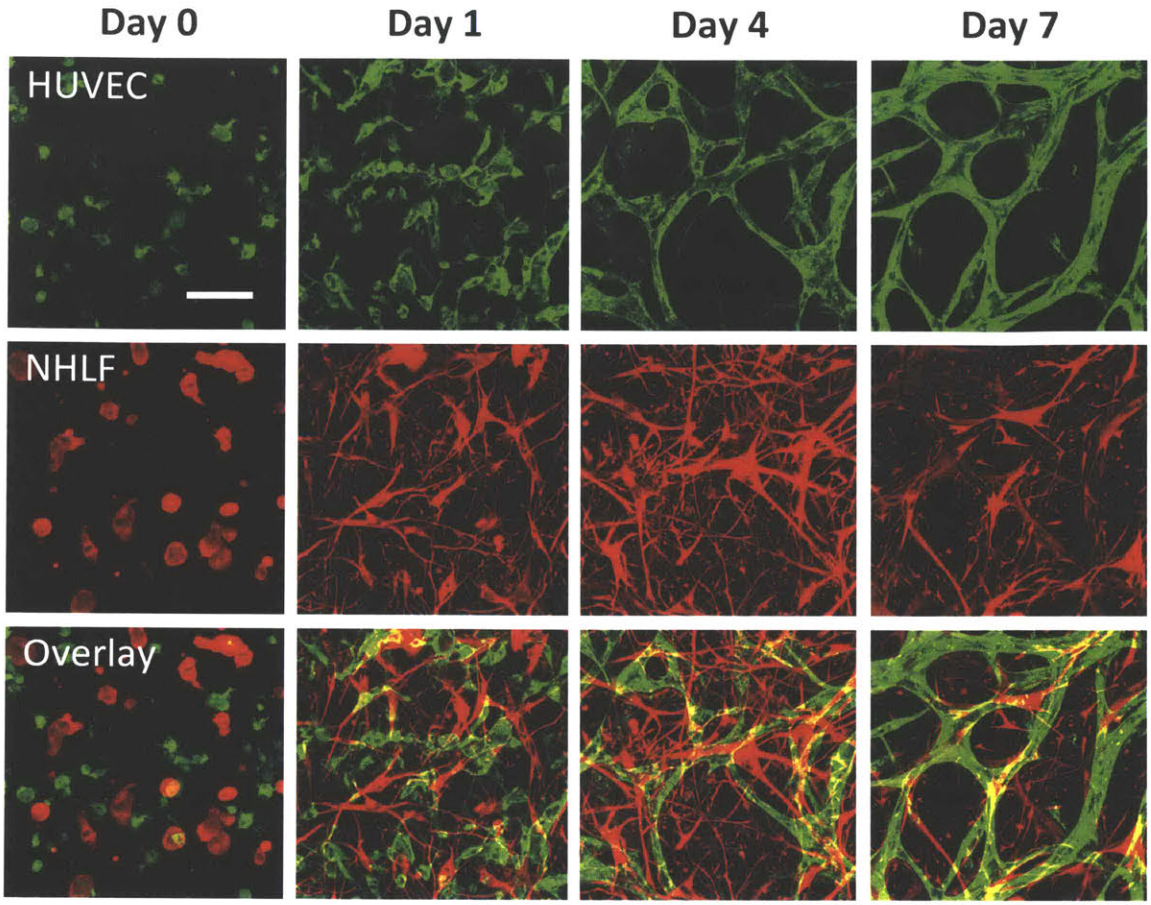

Figure 2-2 Confocal images of vascular morphogenesis. Progression of morphological changes in EC and FB during 1 week of vascular morphogenesis. Scale = 100 μm.

High resolution, 3D confocal imaging revealed the mechanism of vascular lumen formation at the cellular level (Figure 2-3). As early as day 1, the formation of intracellular vacuoles was observed in ECs. Multiple vacuoles within an individual cell were found to coalesce until all the cytoplasm was arranged as a thin shell surrounding the large intracellular vacuole. By day 4, we observed the formation of intercellular connections among ECs through which the intracellular vacuoles of multiple cells were joined together and enclosed by the growing surface. Finally, by day 7, a well-defined multi-cellular vessel structure was observed consisting of a thin EC wall surrounding a patent, fully connected lumen interior.

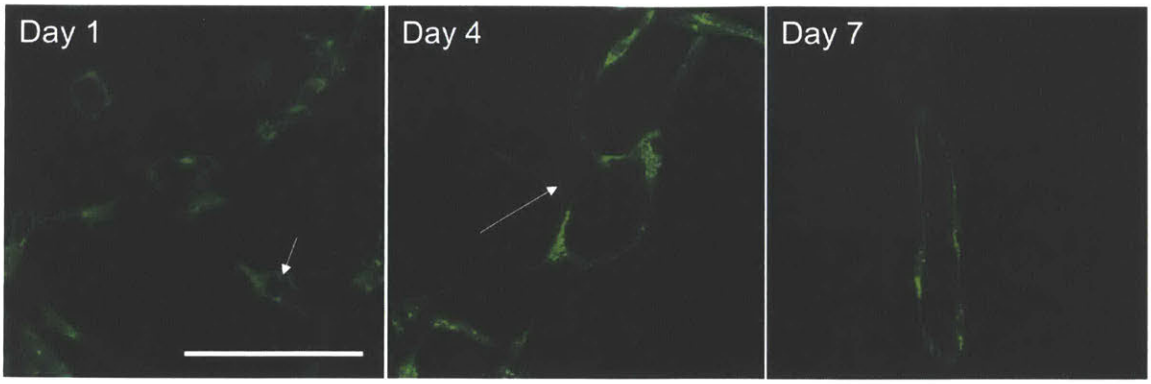

Figure 2-3 EC lumen formation. Day 1: arrow points to single cell with multiple intracellular vacuoles. Day 4: arrow points to joining of intracellular vacuoles between two cells. Day 7: single, multicellular vessel with well-defined lumen. Scale = 100 μm.

FBs also underwent significant shape change in a short amount of time (Figure 2-2). Already by day 1, they extended protrusions and became elongated, with some individual cells spanning a distance of several hundred microns. By day 7, FBs appeared to be preferentially concentrated around the vasculature.

2.2.2 3D Morphology Characterization

We developed methods to accurately quantify the 3-dimensional morphological characteristics of our engineered vasculature at both the vessel and tissue level scales after 1 week of vascular morphogenesis. At the tissue level, we measured a vascular density of 45.6 $\pm$ 4.87 lumens per mm^2 (Figure 2-4a) and a vascular volume fraction of 13.6 $\pm$ 3.32 percent (Figure 2-4b). In the body, these values can span a large range depending on age, health, and specific organ. Our engineered vasculature closely resembled that of the human skin, with regard to capillary density - 34.4 $\pm$ 1.7 per mm^2 measured by Lamah et. al.[173], and that of human lung with regard to vascular volume fraction - 14 $\pm$ 8 % measured by Kampschulte et. al.[174]. These values – especially capillary density – can be much higher, *in vivo*, for more metabolically active organs[175].

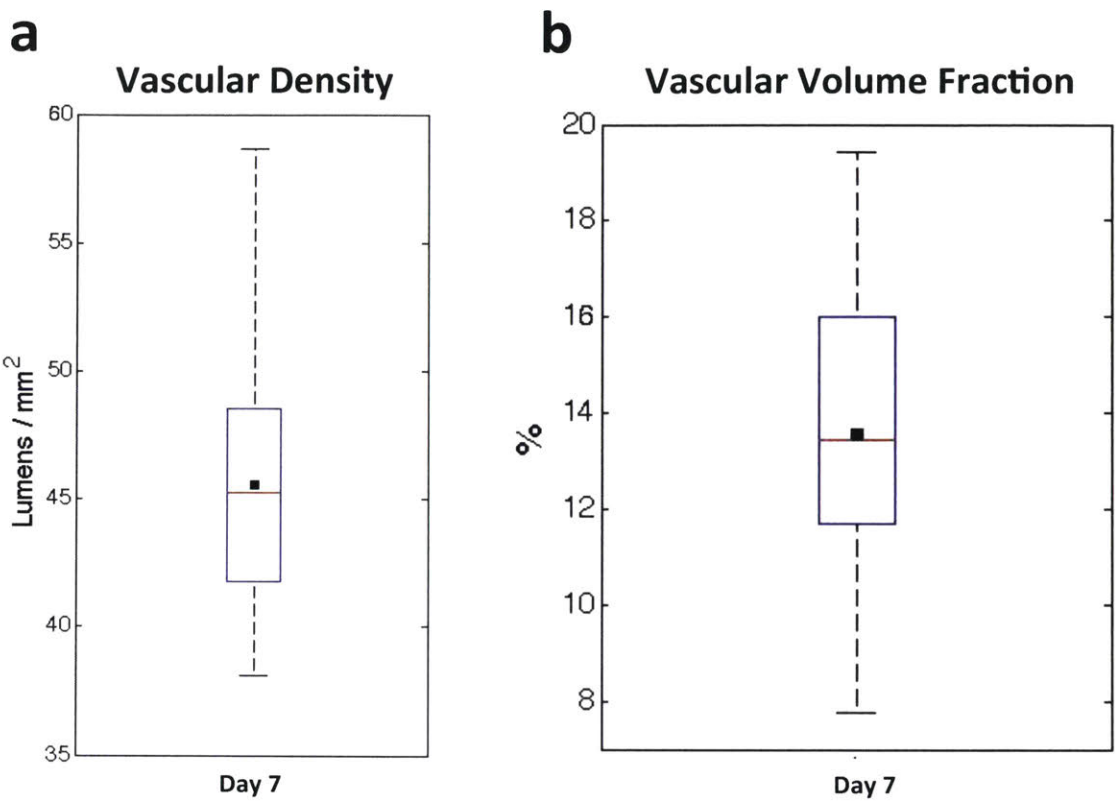

Figure 2-4 Tissue scale vascular morphology measurements. (a) vascular density, (b) vascular volume fraction. Black square represents mean value.

The vasculature that formed in our fluidic device comprised vessels with a heterogeneous range of diameters and lengths consistent with those of the physiological microvasculature, which is made up of capillaries (5 – 10 microns in diameter), venules and arterioles (10 – 100 microns in diameter). We measured an average vessel diameter of 33 microns, with individual vessel diameters spanning a range of 6 – 89 microns (Figure 2-5a-b). We measured an average vessel length of 173 microns with individual vessel lengths spanning a range of 90 – 900 microns (Figure 2-5c-d).

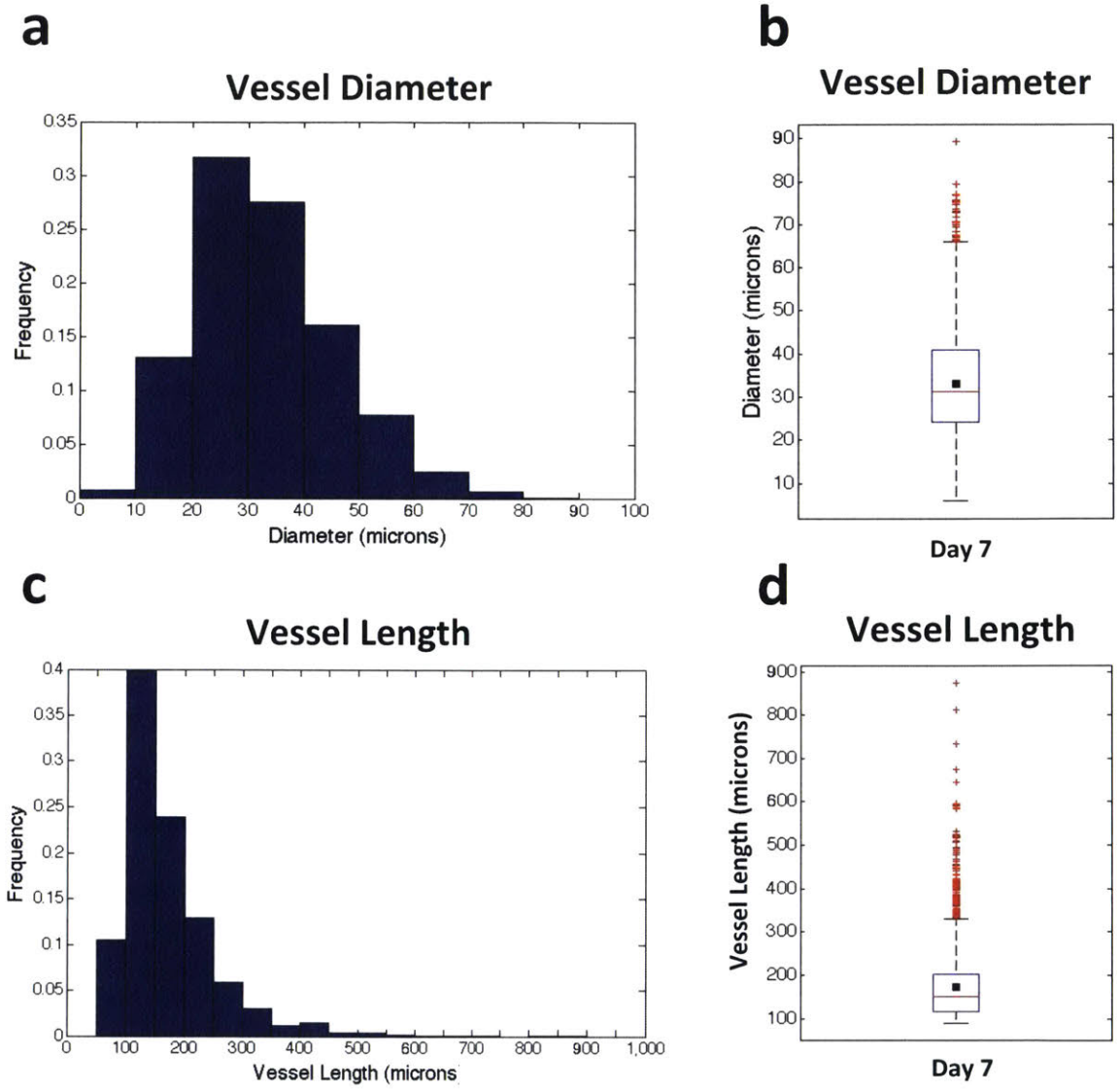

Figure 2-5 Individual vessel morphology measurements. (a-b) vessel diameter, (c-d) vessel length. Black square represents mean value.

The vessel length distribution was skewed towards larger values, and we suspect that this is a function of vascular pruning. The vasculature likely forms initially with a relatively uniform vessel length, determined by the seeding density of ECs and the corresponding inter-cellular spacing. Over time, individual vessel segments are then pruned for reasons such as optimization of nutrient delivery or non-stable regression, leading to an increase in effective length of the neighboring vessels. This could be confirmed experimentally in future studies by tracking the length distribution as a function of time.

2.2.3 Functional Characterization

We next set out to characterize the primary functional properties of our engineered vasculature – namely, bulk convection and trans-endothelial transport. We introduced a fluorescently labeled tracer into the upstream perfusion channel of the fluidic device and induced a pressure gradient across the tissue. The vasculature quickly and uniformly filled with the tracer dye, and 3D confocal imaging revealed that the dye was contained within the vascular lumen space – confirming the presence of a tight endothelial barrier (Figure 2-6).

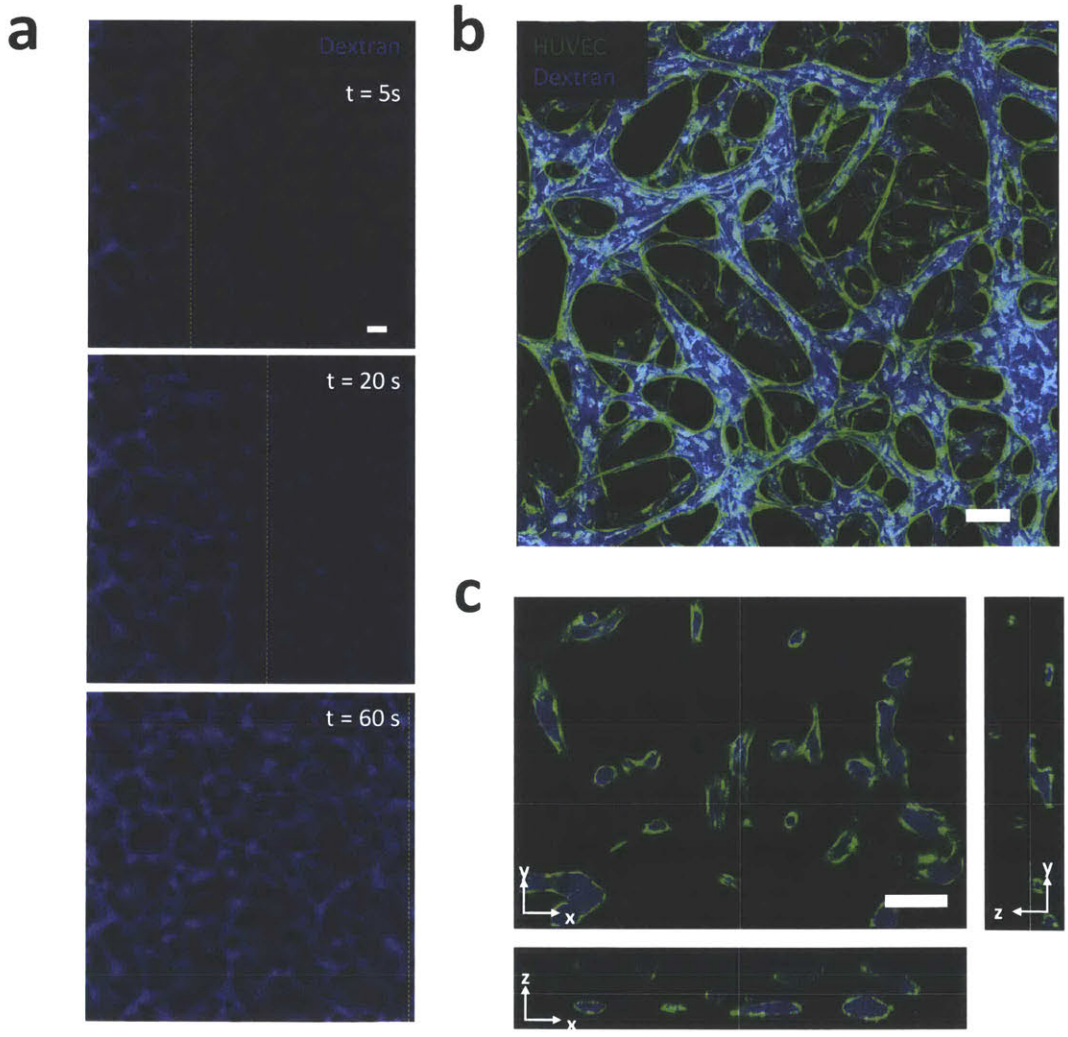

Figure 2-6 Visualization of vasculature with fluorescent tracer dye. (a) dashed line shows penetration of tracer dye into the tissue after introduction into left perfusion channel at time t=0. (b) confocal projection of GFP HUVEC and blue fluorescent dextran (tracer dye). (c) orthogonal view of individual slice showing tissue cross-section with tracer contained to vascular lumens. Scale = 100 μm.

We further developed methods to quantify these properties in 3D. We measured the perfusability of the engineered vasculature to be 96.3 $\pm$ 1.47 percent – demonstrating that nearly all of the formed vasculature was capable of conveying flow (Figure 2-7a; See methods for perfusability calculation details). We measured the bulk volumetric flow rate through the engineered vasculature to be 0.27 $\pm$ 0.086 $\frac{ml}{hr*cmH2O}$ (Figure 2-7b).

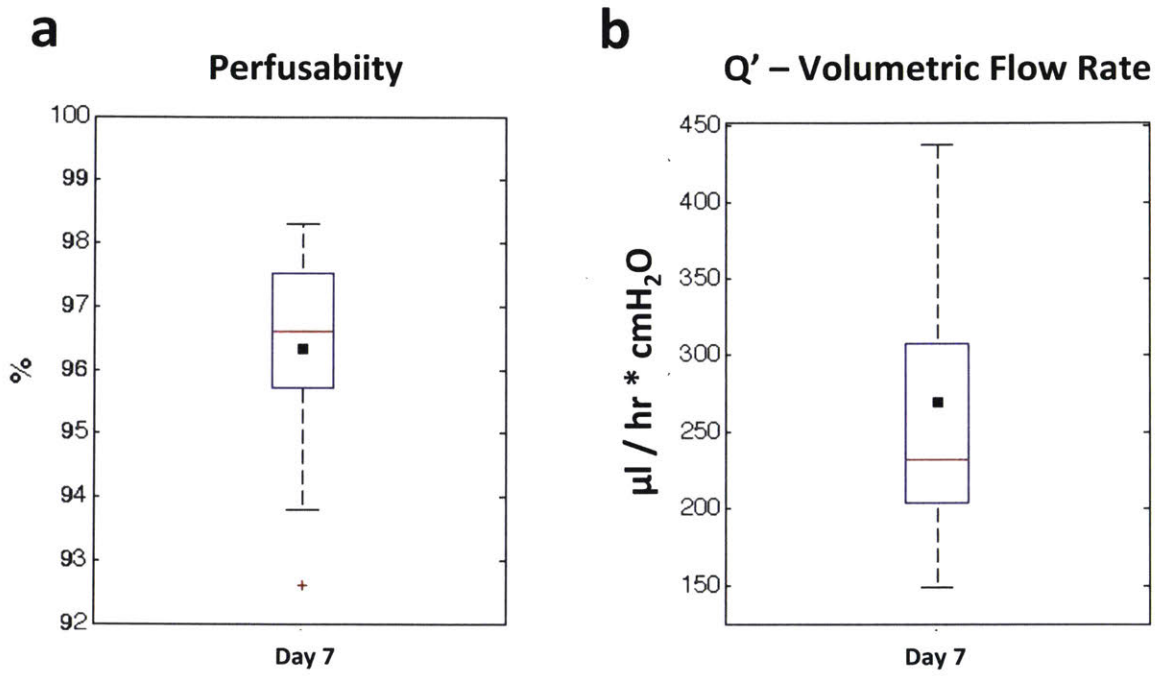

Figure 2-7 Vascular function measurements. (a) perfusability - percentage of vascular lumens containing tracer dye after perfusion, (b) volumetric flow rate through entire tissue construct.

To obtain a local description of the flow profile through the engineered vasculature, we converted 3D images into finite element models and performed CFD analysis to obtain pressure, velocity, and wall shear stress distributions (Figure 2-8). The results predicted a maximum velocity of 1 mm/s and a maximum shear stress of 1 Pa for an applied pressure head of 1 cmH_2O. We further corroborated the velocity predictions by performing particle-tracking experiments on selected regions of the vasculature and observed individual particle velocities of 50 – 400 microns per second. These values are similar to those measured for human microvessels *in vivo*: 0.70 $\pm$ 0.23 mm/s and 0.86 $\pm$ 0.05 Pa measured by Khansari et. al.[176]

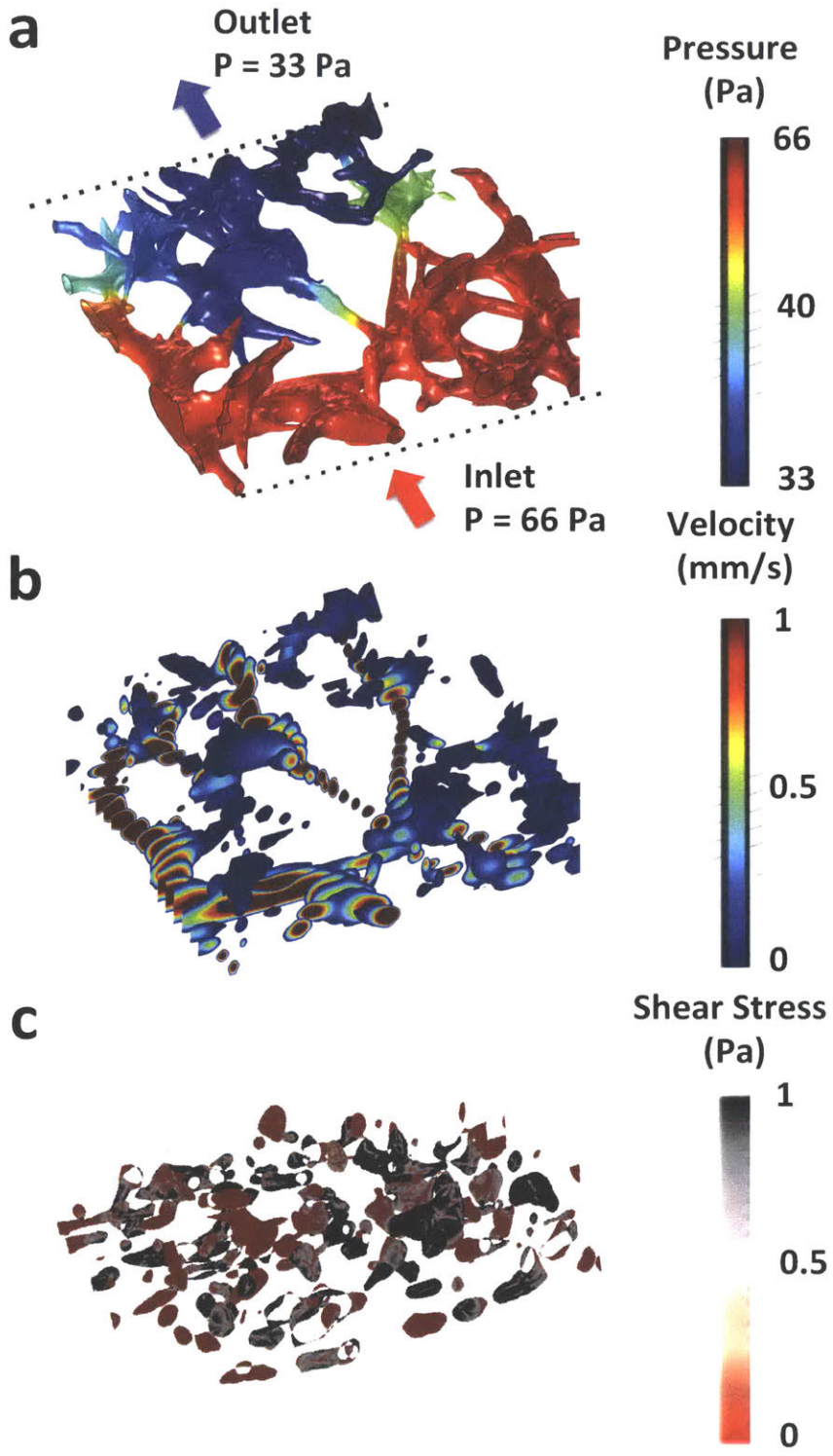

Figure 2-8 CFD results of flow through engineered vasculature. Flow simulation performed on 3D reconstruction of vasculature for 1mm x 1mm x 0.25mm ROI. (a) pressure distribution, (b) velocity profile, (c) shear stress distribution.

In future studies, it will be interesting to correlate the velocities and shear stresses in our system to local vessel morphological properties and vascular function. This information could be useful for biological studies of vascular disease such as atherosclerosis - in which disruptions in the flow profile are thought to promote the disease phenotype[177], or cancer cell extravasation – in which specific regions of the vasculature display higher rates of extravasation events than others[178].

Finally, we developed a method to quantify the permeability of the engineered vasculature in 3D. We measured the permeability to 70 kDa dextran to be 3.13e-7 $\pm$ 1.95e-7 cm/s (Figure 2-9). This value is similar to those measured previously for individual microvessels *in vitro* (3.3e-7 cm/s measured by Price and Tien[179]) and *in vivo* (1.4e-7 cm/s measured by Yuan et. al.[180]). It is significantly lower than those measured previously for large-scale engineered vascular networks *in vitro* (1.7e-6 cm/s measured by Kim et. al.[58] Our value is closer to those measured *in vivo*, likely due to improvements in biological stabilization and the 3D quantification techniques developed in this thesis.

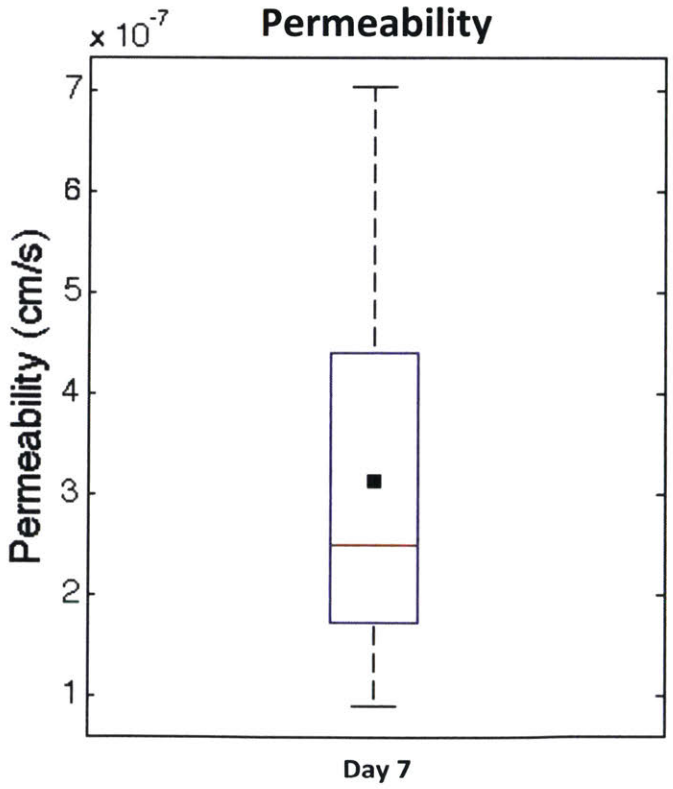

Figure 2-9 Permeability measurements. Bulk permeability of vascular tissue construct after 7 days of culture. Black square represents mean value.

To investigate the nature of vascular perfusion and barrier function in our system at the tissue level, we examined the interface between the perfusion channel and the tissue vascularization channel – the location of bulk fluid transfer into the tissue (Figure 2-10). We found that ECs from the tissue had formed a confluent monolayer covering the interface, thus forming a barrier to bulk transport into the interstitial space. The lumens of individual vessels were found to interface with the perfusion channel through isolated openings in the monolayer that enabled bulk transport into the vasculature.

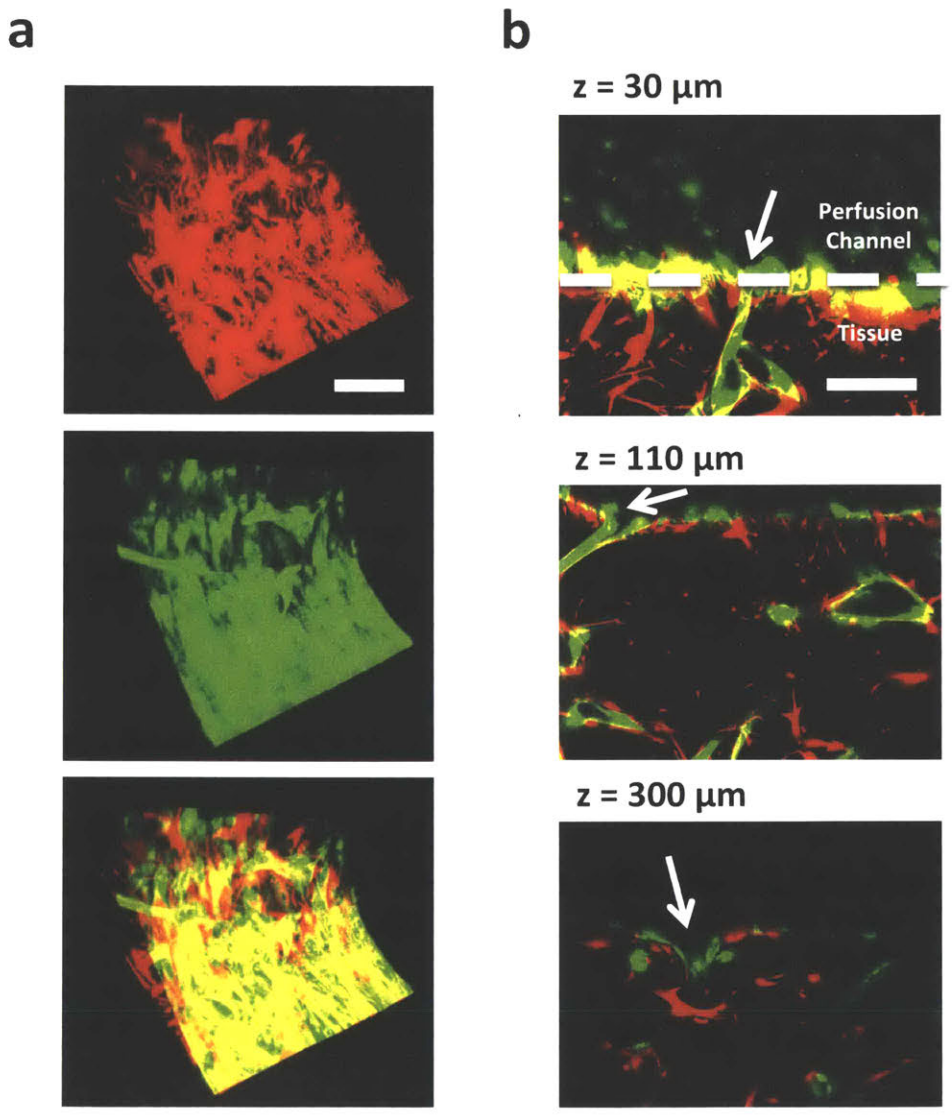

Figure 2-10 Visualization of tissue interface with perfusion channel. (a) confocal images of FB (mCherry) and EC (GF) showing the tissue surface covered with cells at the interface with perfusion channel. (b) openings in the interface connected to vascular lumens in the tissue provide entry for fluorescent tracer into vasculature. White dashed line indicates interface. Images taken at multiple heights within same ROI, show multiple openings. Scale = 100 µm.

2.3 Methods

2.3.1 Device Design

The PDMS fluidic device comprises three adjacent, parallel channels - each with rectangular cross-sectional dimensions of 3 x 1 mm, and 23 mm length (figure 2-11a). Vascularization occurs in the central channel, in which vascular cells are encapsulated in a 3D hydrogel. The adjacent perfusion channels are filled with growth medium to support tissue survival (figure 2-11b). A glass coverslip bonded to the bottom of the device enables real-time imaging with standard microscopy techniques. A key feature of the design is the 0.3 mm PDMS lip extending from the top surface of the fluidic channels along the lines separating the individual channels (figure 2-11c). While filling pre-polymerized hydrogel into the vascularization channel, the lips provide surface tension to prevent the solution from spilling into adjacent channels. This enables the individual channels to be filled independently. The remaining 0.7 mm height of the channel interfaces allow for direct, unobstructed interaction between the adjacent channels.

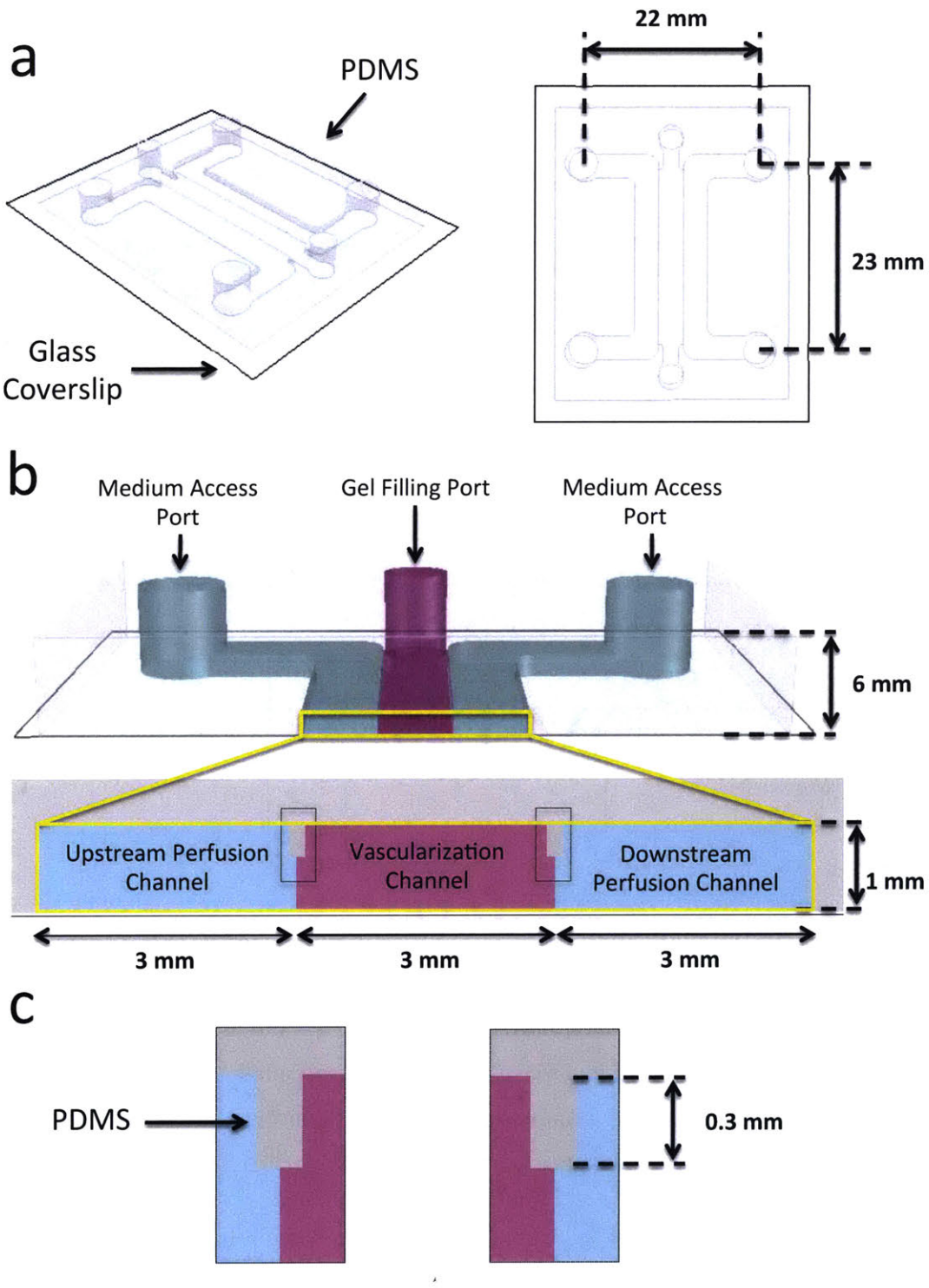

Figure 2-11 Device diagram and dimension. (a) PDMS bonded to glass coverslip for visualization. (c) PDMS lip extending from surface of fluidic channel prevents leakage of pre-polymer hydrogel solution from vascularization channel into perfusion channel through surface tension.

The device was designed with dimensions sufficiently large to yield enough cells, matrix, and culture medium required for standard biological assays. Table 2-1 compares the culture properties of our fluidic device with those of a standard 48-well plate.

Table 2-1 Comparison of cell culture properties between fluidic device and standard 48-well plate. Culture area for fluidic device calculated as 2D projected area of hydrogel channel. Cell yield for fluidic device measured by counting cells after gel removal and gel digestion. Working volume for fluidic device is volume of medium in perfusion channels.

Property	Fluidic Device	48 - well plate
Culture Area	0.66 cm^2	0.95 cm^2
Cell Yield	67,000	95,000
Working Volume (Medium)	198 µl	190 µl

2.3.2 Acrylic Mold Fabrication

PDMS fluidic devices were formed using a custom acrylic mold. To fabricate the mold, a 2D CAD drawing of the fluidic device outline was first generated and used to laser-cut (Epilog) a 1 mm thick piece of acrylic (Ridout Plastics). Next, 300 micron deep grooves were etched into the top of the mold along the lines separating individual fluidic channels. Finally, the bottom of the mold was bonded to an acrylic base by applying 30 psi at 85° C for 30 min.

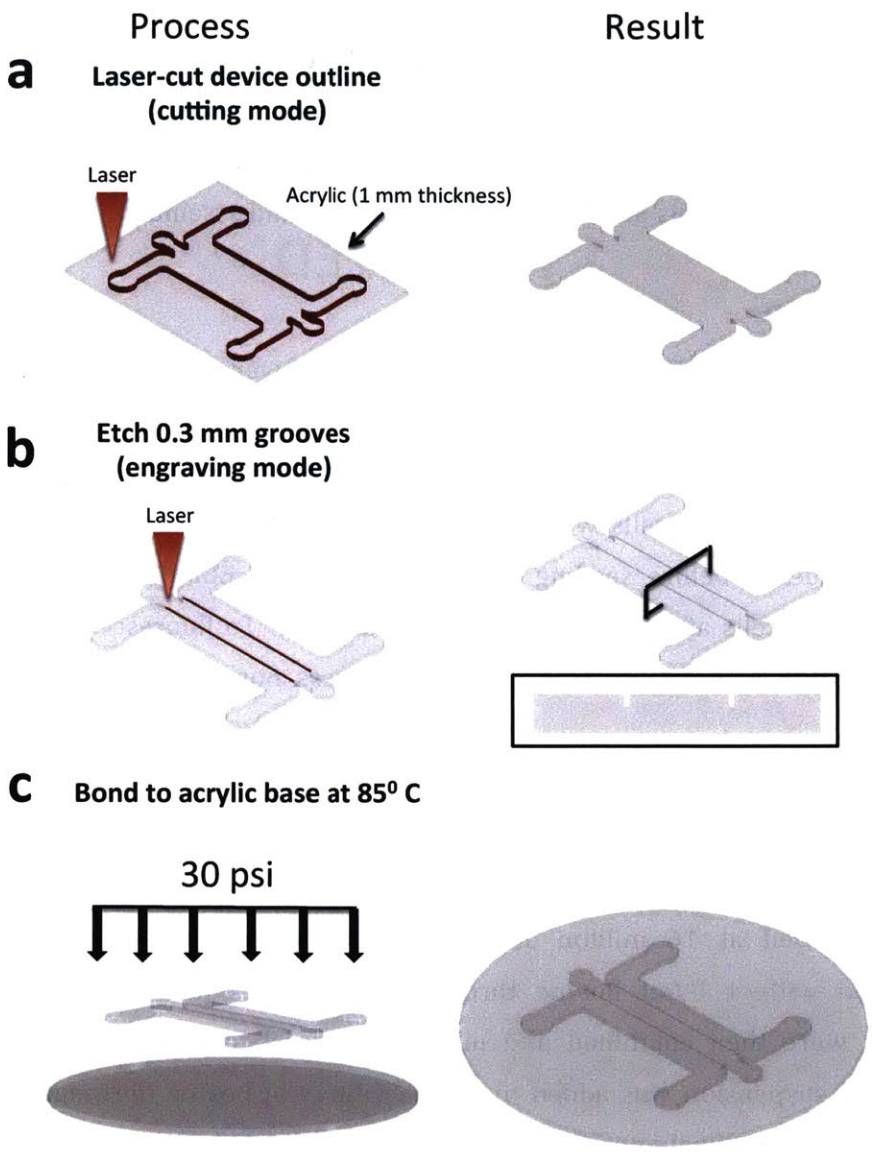

Figure 2-12 Acrylic mold fabrication. 3-step process: (a) cut outline of mold out of 1-mm thick acrylic; (b) etch 0.3 mm grooves at boundaries between adjacent channels; (c) bond acrylic to acrylic using force at high temperature to initiate melting and fuse together.

2.3.3 PDMS Device Fabrication

The acrylic mold was taped to the bottom of a 60 mm petri dish. PDMS and crosslinker (10:1; Sylgard-184; Dow Corning) were mixed, degassed and poured over the mold to a height of 6 mm. After curing for 4 hours at 60° C, the PDMS was cut and peeled from the mold. Gel filling ports and medium access ports were created by punching out 1 mm and 4 mm holes, respectively, completely through the PDMS at the appropriate locations using a

biopsy punch (Miltex). The device was cleaned with tape to remove debris and then sterilized in an autoclave. Finally, the bottom of the device and a glass coverslip (No. 1; Electron Microscopy Sciences) were treated in a plasma etcher (Harrick) for 60 s and pressed firmly together to form an irreversible bond. See Shin et. al.[15], and Chen et. al.[4], for further diagrams and details on PDMS device fabrication and assembly.

2.3.4 Cell Culture

HUVEC were cultured in EGM-2MV medium, and NHLF were cultured in FGM-2 medium during passaging. All cells and media were purchased from Lonza. Cells were initially expanded and cryopreserved to establish a consistent stock used for all experiments. For an individual experiment, cells were plated onto collagen coated (50 μg/ml) flasks and grown to confluency before seeding into fluidic devices. EGM-2MV medium was used exclusively for all cells after seeding into fluidic devices. To fluorescently label the cells, HUVEC and NHLF were stably transduced to express non-localized GFP and mCherry, respectively.

2.3.5 Cell Encapsulation

Endothelial cells and fibroblasts were trypsinized (Gibco), counted, and pelleted. The cells were re-suspended at 16 million and 8 million cells/ml, respectively, in EGM-2MV supplemented with 4 U/ml bovine thrombin (Sigma). Equal parts of the two cell suspensions were then combined and mixed. For each device, 50 microliters of the combined cell suspension was added to 50 microliters of bovine fibrinogen (6 mg/ml in PBS; Sigma) to form a final encapsulation suspension of: 4 M/ml ECs and 2 M/ml FBs in 3 mg/ml fibrinogen with 2 U/ml thrombin. The suspension was mixed several times, slowly, over ice – to avoid premature polymerization – and then pipetted into the vascularization channel - half the volume through each of the two gel filling ports (Figure 2-13). The device was immediately placed in a humidified chamber and incubated at room temperature for 30 min during fibrin polymerization. Finally, the perfusion channels were filled with warm EGM-2MV through the medium access ports. The devices were incubated at 37° C and 5% CO_2 for the remainder of the culture and growth medium in the perfusion channels was replaced every day.

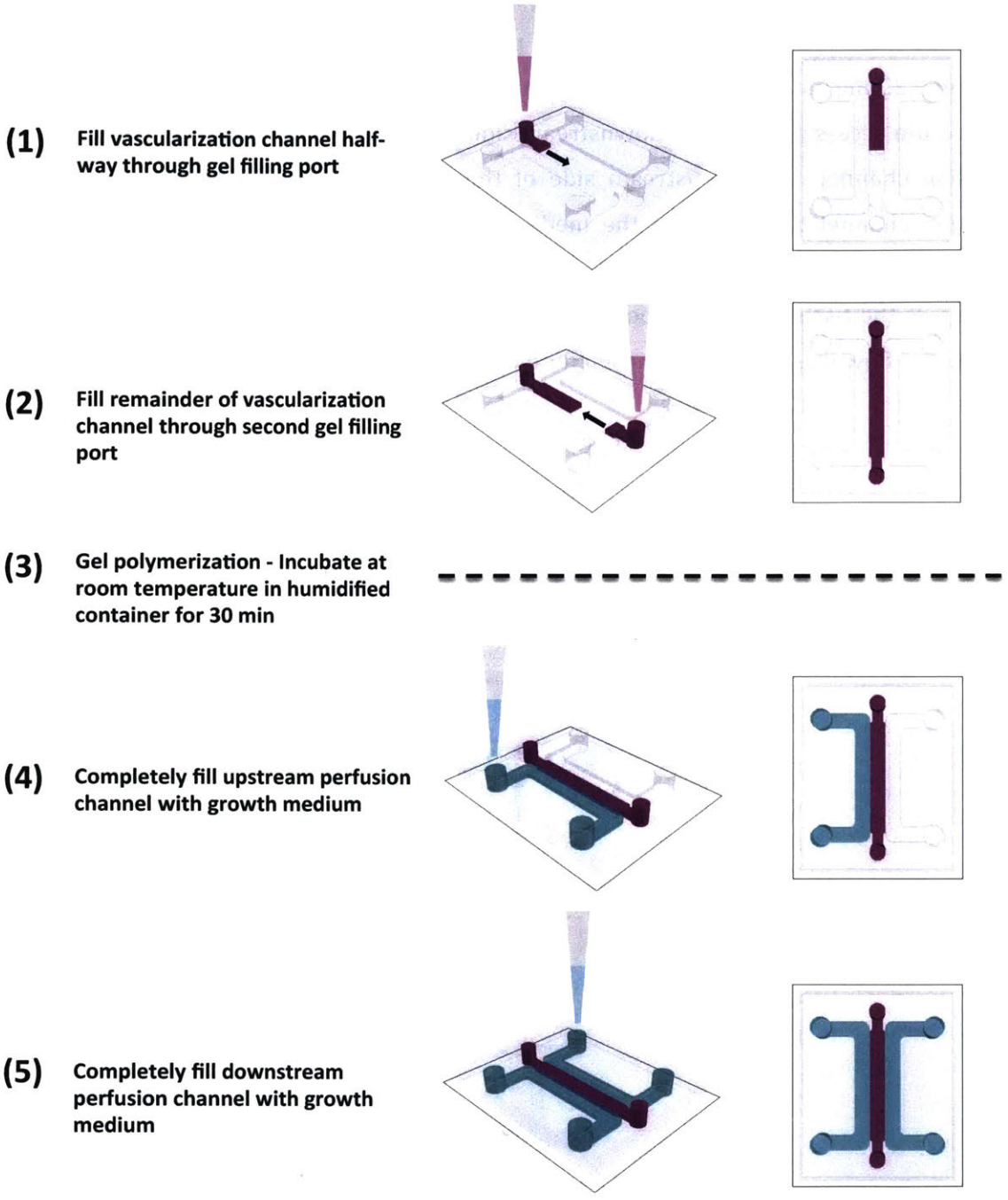

Figure 2-13 Gel filling procedure.

2.3.6 Tracer Visualization

All 3D morphology and functional quantification was performed on confocal image stacks in which the vasculature was visualized by perfusion with a fluorescent tracer (70 kDa dextran; 0.25 mg/ml in EGM-2MV; Life Technologies). This was achieved by: (1) emptying the medium access ports on the downstream side of the tissue, (2) completely emptying the perfusion channel on the upstream side of the tissue, and (3) re-filling the up-stream perfusion channel to the top of the medium access ports with medium containing the fluorescent tracer (Figure 2-14a). This resulted in a hydrostatic pressure head of 0.5 cm H_2O across the tissue and corresponding flow though the vasculature (Figure 2-14b). The direction of flow was arbitrarily chosen for each device (i.e. upstream/downstream).

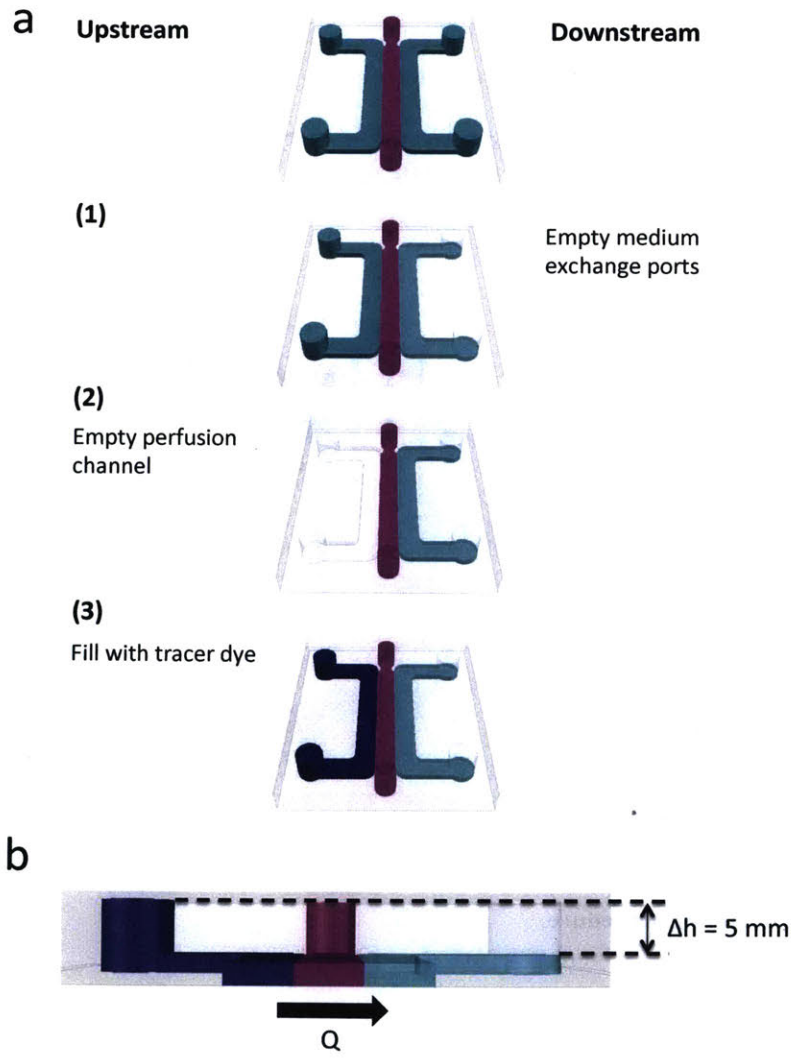

Figure 2-14 Tracer visualization. Initiation of pressure head across tissue to fill vasculature with tracer dye.

Images of the vasculature (GFP) and tracer (blue) were simultaneously acquired with a confocal microscope (Olympus) to a tissue depth of 225 microns with a 10X objective and 4.51 micron spacing between slices (figure 2-15).

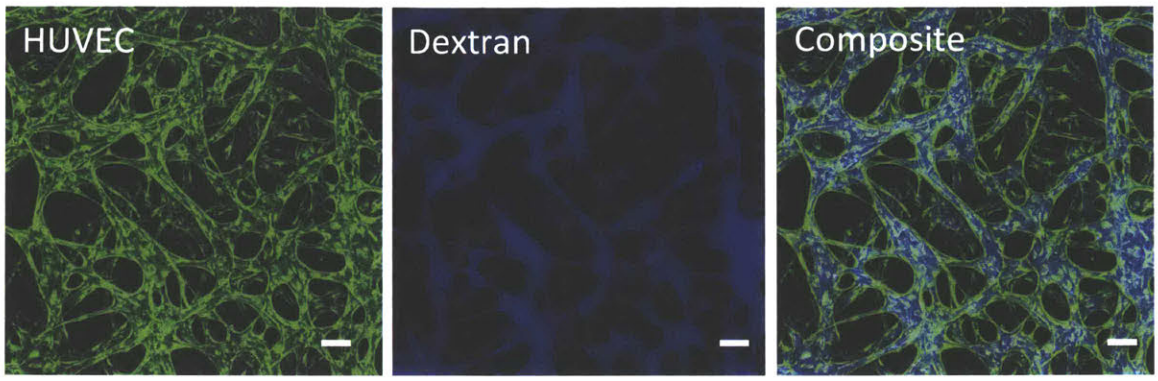

Figure 2-15 Confocal projection of tracer filled vasculature. Scale = 100 μm.

2.3.7 3D Morphology Characterization

To objectively quantify vascular morphological and functional properties using universal metrics, calculations were performed on full 3-dimensional images, without collapsing the confocal stacks. The individual slices were processed and binarized using imagej (See Appendix 3 for full macro script). The tracer filled regions were defined as the vasculature and the remaining volume defined as the interstitial space (figure 2-16). Because the tracer was used to define the vascular region, these calculations are only meaningful for well-developed vasculature with sufficient barrier function such that the tracer is contained to the vascular region during the time required to image (~30 min).

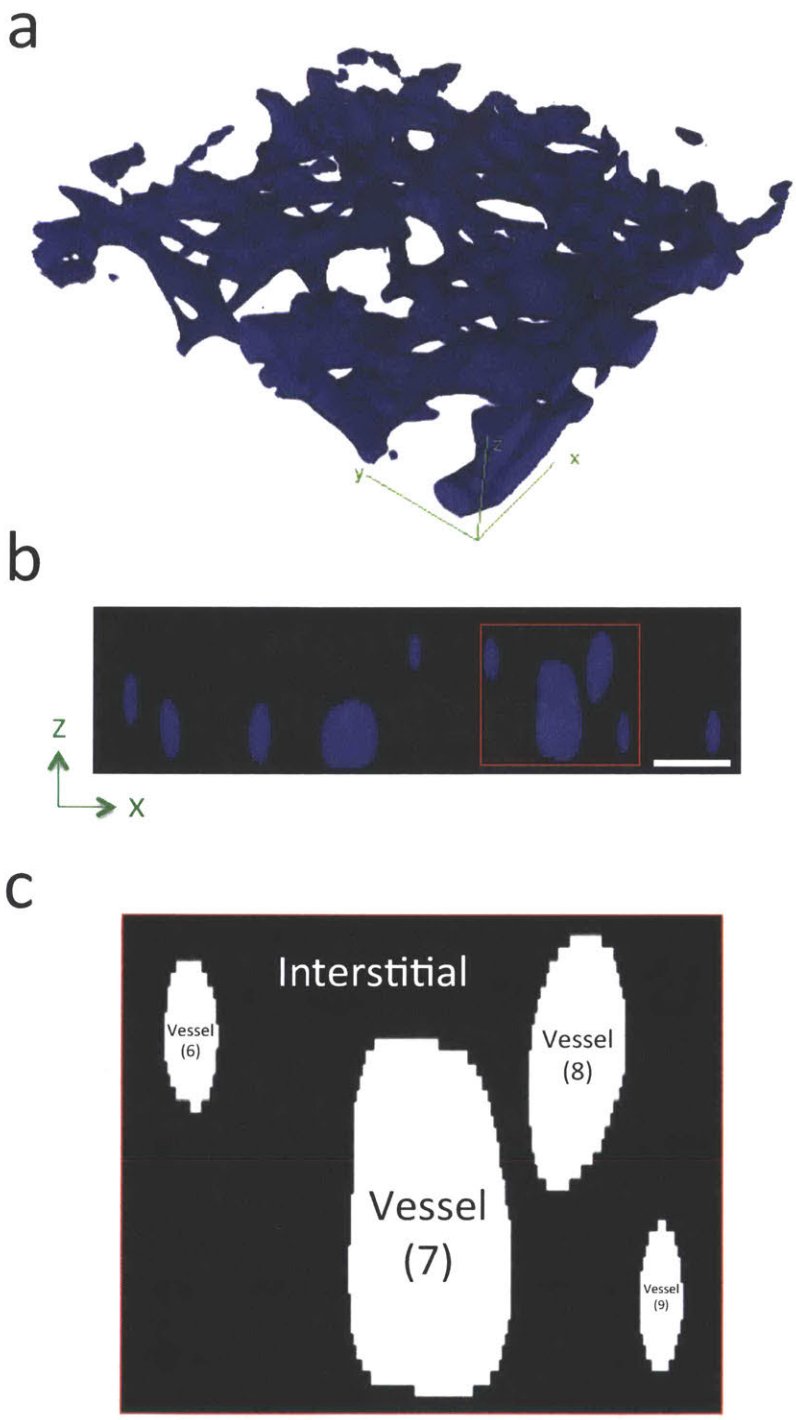

Figure 2-16 3D reconstruction of tracer filled vasculature. (a) confocal 3D image. (b) resliced in x-z plane, perpendicular to direction of flow. (c) automated lumen identification.

2.3.7.1 Vascular Density

Re-slicing the binarized volumes perpendicular to the flow direction, we quantified the number of lumens per cross-section (figure 2-16c) with an automated script (Appendix 3). Vascular density was calculated by dividing this number by the cross-sectional area.

2.3.7.2 Vascular Volume Fraction

The total luminal cross-sectional area divided by the total cross-sectional area was used to calculate the vascular volume fraction:

$$Vascular\ Volume\ Fraction = \frac{\sum_{i=1}^{N} A_i^V}{\sum_{i=1}^{N} A_i^V + A^I}$$

where,

A_i^V is the cross-sectional area of the i_{th} vessel and A^I is the interstitial cross-sectional area.

3D morphology metrics for a 1272 x 1272 x 225 micron ROI (X x Y x Z) were calculated by averaging the values for 800 XZ-cross-sections evenly spaced throughout the tissue volume.

2.3.7.3 Vessel Diameter and Length

To calculate 3D vessel diameters and lengths, we utilized the Filament Tracer extension for Imaris (Bitplane) - a commercially available 3D image analysis software – to analyze our binarized, 3D reconstructed images. Briefly, the software performed a thinning algorithm, resulting in a 3D skeleton (Figure 2-17). The skeleton segment lengths were directly used to determine vessel lengths. To remove terminal and unconnected branches, we imposed a minimum branch length of 50 microns. The vessel diameter at any point was determined by the cross-section of the binarized vessel perpendicular to the skeleton axis at that point. An average diameter was automatically calculated for each vessel. We used an automated routine to batch process the images with the parameters given in table 2-2.

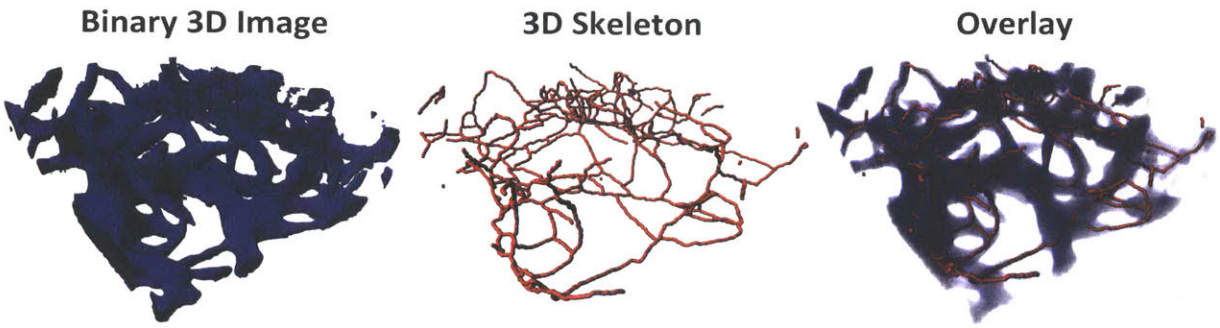

Figure 2-17 3D skeletonization. Automated skeletonization of vasculature performed using Imaris software - filament function.

Table 2-2 Skeletonization parameters. Parameters used for Imaris – filament function to batch process skeletonization of 3D confocal images of vasculature.

Algorithm	
Name	Threshold (loops)
Track (over time)	false
Preprocessing	
Channel Index	1
Enable Preprocessing	true
Approximate Diameter	3.67 um
Preserve Edges	false
Segmentation	
Fill Cavities	false
Connected BaseLine	true
Threshold Low	0.000
Threshold High	255.000
Graph Compilation	
Branch Length Ratio	5.000
Find Dendrite Beginning Point	false
Finish	
Build all Time Points	true
Delete Working Channel	true

2.3.8 3D Functional Characterization

2.3.8.1 3D Perfusability

To calculate 3D perfusability, confocal stacks were re-sliced in the x-z plane and both GFP (HUVEC) and blue (Dextran) channels were binarized. The HUVEC channel was used to identify vessel outlines. The outlines were then overlaid with the dextran channel to identify those vessels that were perfused. If a vessel cross-section contained dextran within it, its area was added to the total perfused area. This calculation was performed for all x-z cross-sections throughout the volume. 3D perfusability was calculated by dividing the total perfused volume by the total vascular volume.

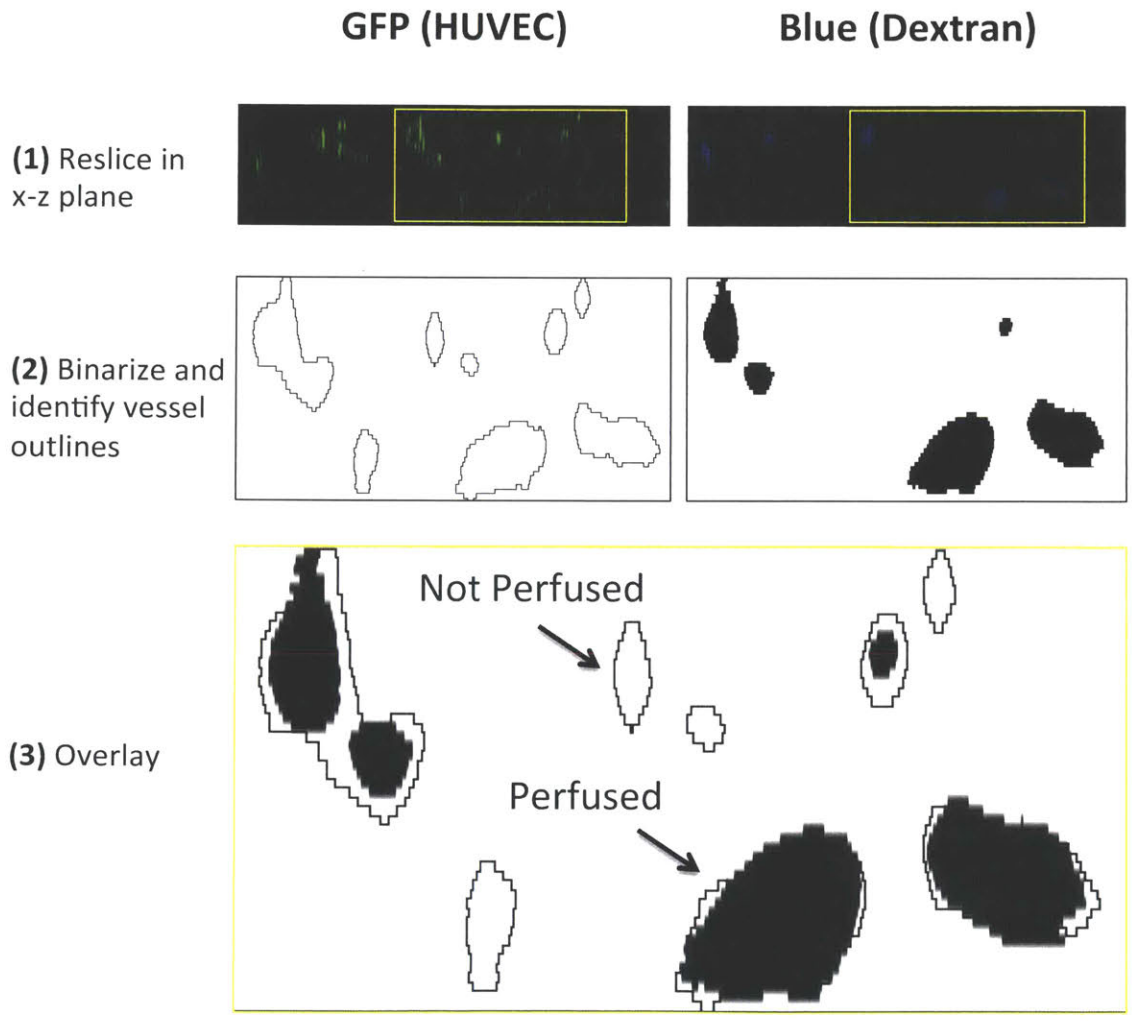

Figure 2-18 3D perfusability image analysis. (1-2) outline of GFP HUVEC used to define vessel perimeter. (3) lumens containing dextran defined as perfusable.

2.3.8.2 Volumetric Flow Rate

To experimentally measure the bulk flow properties of the vasculature, leuer-lock fittings with barbed tube ends (McMaster-Carr) were attached to plastic syringes (BD) and inserted into the medium access ports of the fluidic device. The plungers were removed from the syringes such that the syringes acted as open-air reservoirs with their contents exposed to atmospheric pressure (See Sudo et. al., FASEB J 2009[181], and Chan et. al., PLOS One 2012[61] for diagrams of experimental setup). A pressure head of 3 cm H_2O was established between the reservoirs on the upstream and downstream sides of the vasculature. Using the volume gradation lines printed on the syringes, the height difference between upstream and downstream reservoirs was recorded as a function of time. From these measurements, the pressure difference (ΔP) and volumetric flow rate (Q) was calculated for each time interval and plotted as ΔP vs Q (Figure 2-19a). The slope of this plot was used to determine the volumetric flow rate per cmH_2O, Q^* (Figure 2-19c). The same experimental setup was used to determine the hydraulic permeability of a non-vascularized fibrin gel in the fluidic device, K, where $K = \frac{1}{Q^*}$.

a

t (s)	dt (sec)	dh	dv	dP	Q (ul/hr)
0	0			14	3562.848
25	25	1	24.742	12	3711.3
49	24	1	24.742	10	2783.475
81	32	1	24.742	8	2172.468293
122	41	1	24.742	6	1746.494118
173	51	1	24.742	4	1171.989474
249	76	1	24.742	2	

b

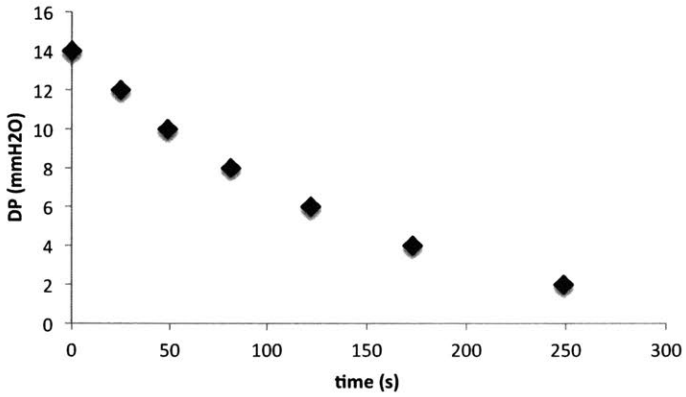

c

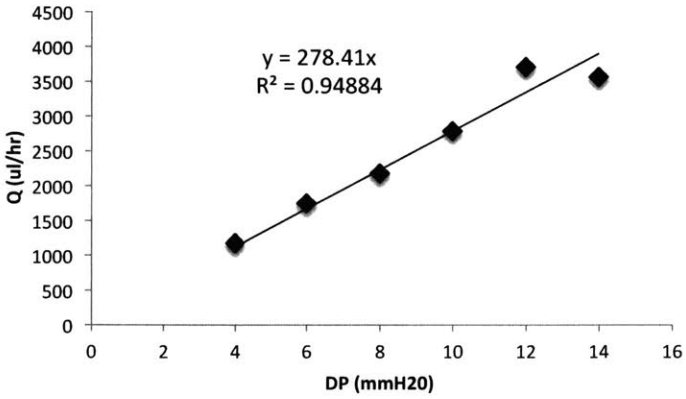

Figure 2-19 Volumetric flow rate sample calculation. (a) grey columns indicate measured inputs, all other values calculated. (b) exponential decay of pressure during flow through vasculature. (c) linear fit to determine flow rate.

2.3.8.3 *Permeability*

For permeability measurements, we calculated the average tracer intensity in both the vascular and interstitial spaces immediately after introducing the tracer, and again at a later time point (t =12 - 24 min). The difference in interstitial intensity along with morphological properties of the vasculature were used to calculate the permeability coefficient, *P* (See Appendix 3 for full macro script).

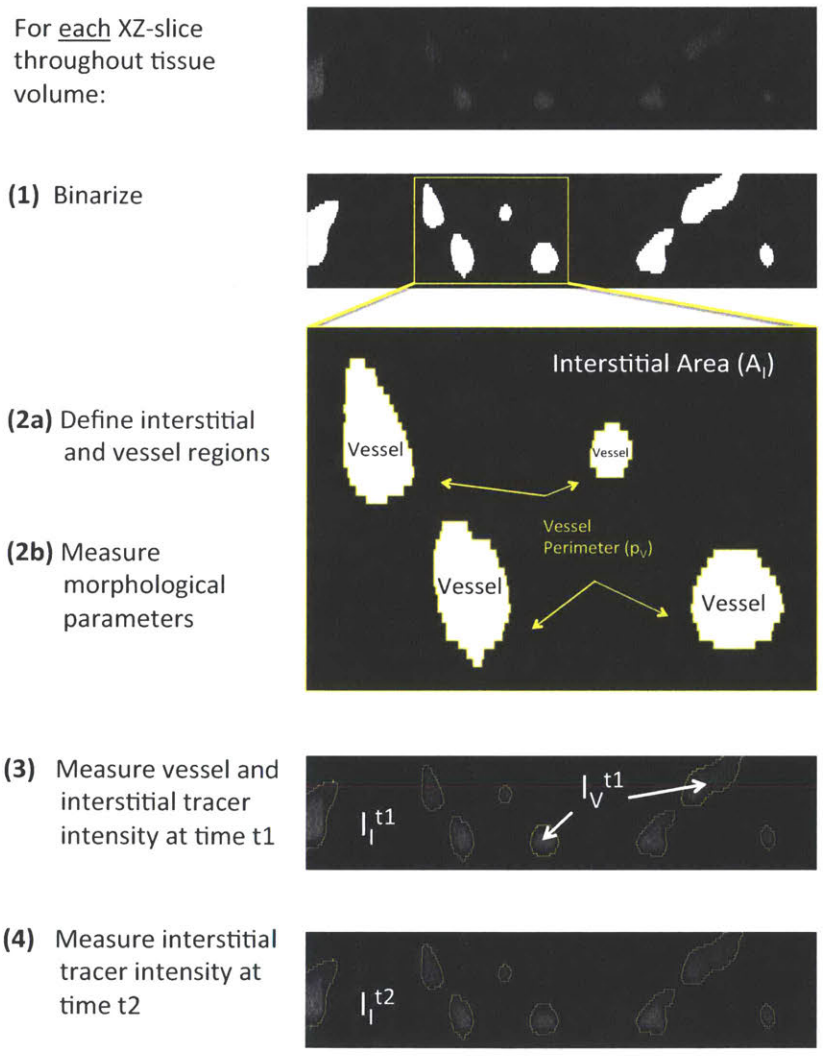

Figure 2-20 Permeability image analysis.

Performing a mass balance for the fluorescent tracer crossing the vascular endothelium into the interstitial tissue over a given time interval, Δt, we obtain:

Tracer Accumulation in Interstitium		***Tracer Crossing through Endothelium***
$(I_I^{t2} - I_I^{t1}) * V_I$	=	$P * (I_V^{t1} - I_I^{t1}) * S_V * \Delta t$

where,

I_I^{t1} , and I_I^{t2} are the tracer intensities in the interstitial volume at the initial and final time points, respectively.

V_I is the total interstitial volume.

I_V^{t1} is the tracer intensity in the vasculature at the initial time point.

S_V is the total vascular surface area.

Solving for the Permeability coefficient, we obtain:

$$P = \frac{(I_I^{t2} - I_I^{t1})}{\Delta t} * \frac{1}{(I_V^{t1} - I_I^{t1})} * \frac{V_I}{S_V}$$

Taking into consideration the fact that the tracer intensities, I_I *and* I_V, are not completely uniform throughout the volume, we replaced them with their volume-averaged values, $\overline{I_I}$ and $\overline{I_V}$ to obtain a bulk Permeability coefficient for the entire volume, $\bar{P}$:

$$\bar{P} = \frac{\left(\overline{I_I^{t2}} - \overline{I_I^{t1}}\right)}{\Delta t} * \frac{1}{\left(\overline{I_V^{t1}} - \overline{I_I^{t1}}\right)} * \frac{V_I}{S_V}$$

$\bar{I}_I$, and $\bar{I}_V$ are calculated by first averaging over the respective regions for each cross-section, and then averaging over all cross-sections throughout the volume.

V_I is calculated by summing the interstitial area, A_I, of all cross-sections throughout the volume and multiplying by the slice depth.

S_V is calculated by summing the vessel perimeters, p_v, for each cross-section, then summing over all cross-sections throughout the volume, and multiplying by the slice depth.

The above formulation relies on the following assumptions:

1. Fluorescence intensity is linearly related to tracer concentration.
2. Acquisition ROI is large enough to capture all tracer leaving the vasculature.
3. Zero net flux boundary conditions.

Assumption 1 is satisfied for fluorescently conjugated dextran (data not shown).

Assumption 2 is satisfied as long as the entire vascular volume is imaged. If not, a large enough ROI should be imaged, such that the tracer diffusion length during the interval, Δt, is comparatively small. Using a value of 4.5E-11 m^2/s for the diffusion constant of dextran[27], and a 10 minute interval, we calculated the diffusion length to be on the order of 100 microns as compared to our imaging ROI of 1272 x 1272 x 225 microns.

Assumption 3 is satisfied as long as the system is sufficiently uniform at the scale of the ROI, and there is no bulk transport from the tissue boundaries. By imaging several, large ROIs per device, we limited the effects of spatial variability. In our system, there is a tracer concentration gradient at the boundary between the perfusion channel and the vascularization channel. The effects of bulk diffusion were limited by imaging a ROI at a

distance of 1 mm from this interface, well above the tracer diffusion distance. Additionally, by seeding endothelial cells on this interface, we were able to enhance the barrier to diffusion there and further limit these effects.

It should be noted that the algorithm used to identify vascular lumens consistently over-estimated the vessel diameter. This can be seen in figure 2-20, panel 3. The dark portion immediately inside the yellow vessel outline presumably belongs to the interstitial space, but is counted as part of the vessel region. This error affects two parameters in the permeability calculation: (1) intensity difference between vessel and interstitium (underestimation), and (2) vessel surface area (overestimation). The effect of the former leads to an overestimation of the permeability, while the latter has the opposite effect. Because the intensity underestimation scales with lumen area, while the surface area overestimation scales with lumen diameter, the overall effect is an overestimation of the permeability that scales with the error in the measurement of the lumen diameter. As seen in the images, this error varies with vessel size and is largest for smaller vessels. Assuming an average error of 50% in measuring the diameter, this would lead to an overestimation of the permeability by 50%. This is within the standard deviation of our measurements and comparable to other sources of quantification error. Since the error appears largest in the z-direction, we could improve the calculations by imaging at higher magnification to increase the z-resolution. However, doing this would significantly reduce the measurement ROI and require increased image acquisition time to collect data that is representative of the bulk tissue.

2.3.9 CFD Modeling

Meshes were generated from 3D reconstructed, binarized images of the vasculature (see Appendix 3), using the commercially available software - Simpleware. Briefly, after the images were imported into Simpleware, they were (1) resampled (cubic); (2) thresholded - to generate a mask; (3) a recursive gaussian was applied; and (4) island removal was performed for objects < 100,000. Finally, a mesh was created with the following options: (a) binarize, (b) smart mesh, (c) Comsol (all versions). The mesh was then imported into the commercially available, finite element software - COMSOL - to perform simulations. Constant pressure boundary conditions of 66 Pa and 33 Pa were applied at the upstream and downstream interfaces of the vasculature, respectively. The images used to generate the meshes were acquired from the middle 1 mm of the 3 mm wide tissue - so the pressure

values were chosen to model a 100 Pa pressure drop across the entire tissue. The no-slip boundary condition was applied at the internal surfaces of the vasculature and at the bottom interface of the tissue, representing the glass slide in our experimental setup. Symmetric boundary conditions were applied at all other interfaces of the tissue section.

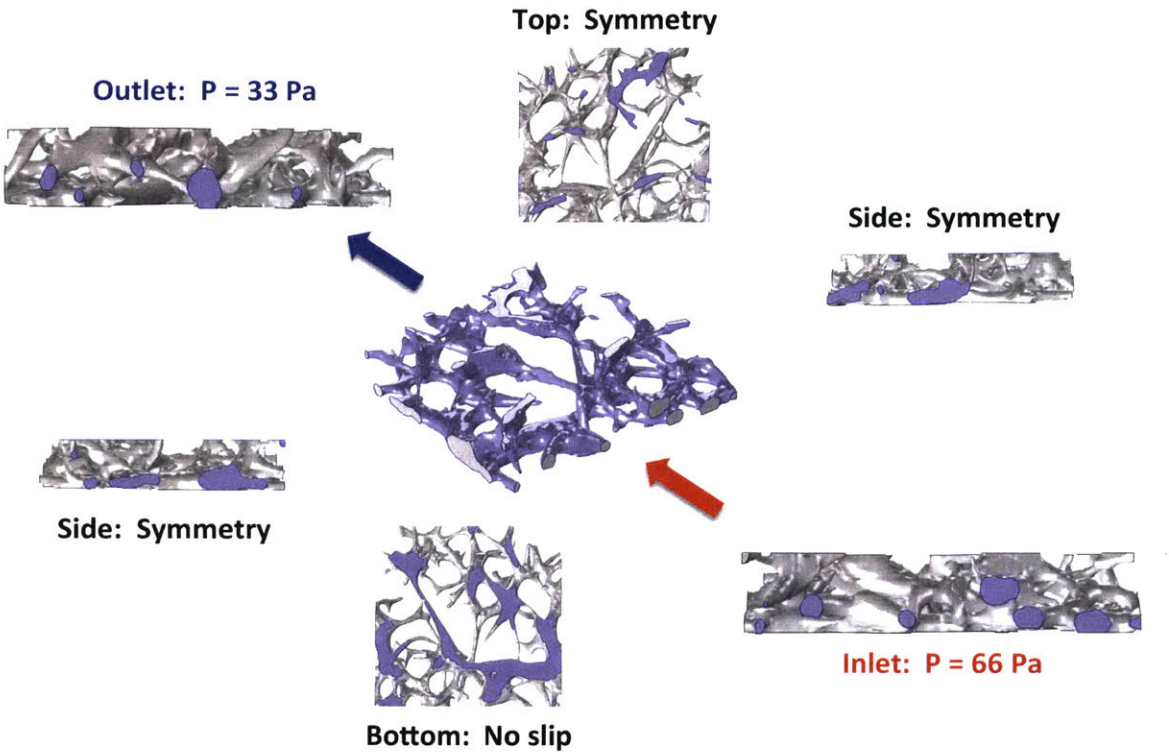

Figure 2-21 CFD boundary conditions.

3 *Effects of Fibroblast Co-culture*

3.1 Introduction

It is well known - based on our own previous findings and those of others[63,72,157,182] - that fibroblasts aid ECs in the formation and stabilization of vascular networks. However, the nature of this beneficial heterotypic interaction remains unclear, and there is discrepancy in the literature as to whether physical contact between the two cell types is necessary or whether paracrine signaling alone is sufficient.

To answer this question, we modified our fluidic device by incorporating two additional cell encapsulation channels – one on either side of the vascularization channel and separated by a medium filled perfusion channel – to enable the physical separation of fibroblasts from ECs and ensure that heterotypic cell-cell communication was limited to the diffusion of secreted factors (Figure 3-1). We studied three conditions: Monoculture (**MC**) – ECs encapsulated in the vascularization channel and cell-free fibrin gels in the cell encapsulation channels; Paracrine Co-culture (**PCC**) – ECs seeded in the vascularization channel, and FB seeded in the cell encapsulation channels; Juxtracrine Co-culture (**JCC**) – ECs and FB seeded in the vascularization channel, and cell-free fibrin gels in the cell encapsulation channels.

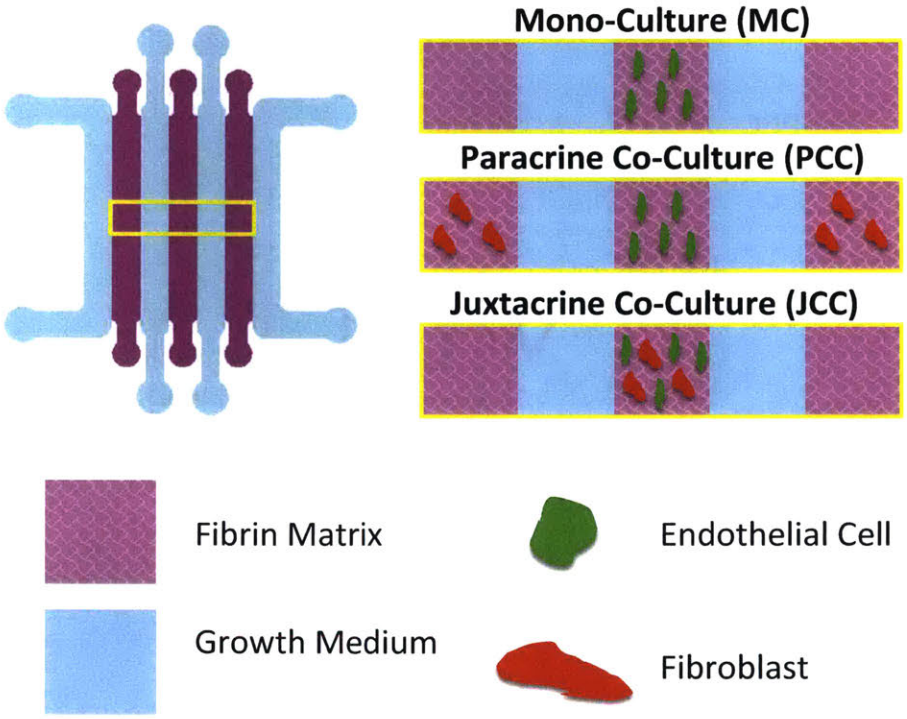

Figure 3-1 Co-culture Fluidic Device. Modified version of fluidic device with 3 parallel hydrogel channels, separated by growth-medium filled perfusion channels to compare co-culture conditions. MC – Monoculture – ECs encapsulated alone in vascularization channel; PCC – Paracrine co-culture – ECs encapsulated alone in vascularization channel and FB encapsulated alone in side hydrogel channels; JCC – Juxtacrine co-culture – ECs and FBs encapsulated together in vascularization channel.

3.2 Results

3.2.1 Vascular Morphology

We observed dramatic differences in vascular morphology between the different co-culture conditions (Figure 3-2a). Monoculture ECs elongated and self-assembled into multicellular networks, but intercellular connections were subsequently lost, and the structures fully regressed after 96 h. Paracrine co-culture with fibroblasts resulted in vascular networks that persisted through 1 w of culture. The vessels had large diameters comprised of

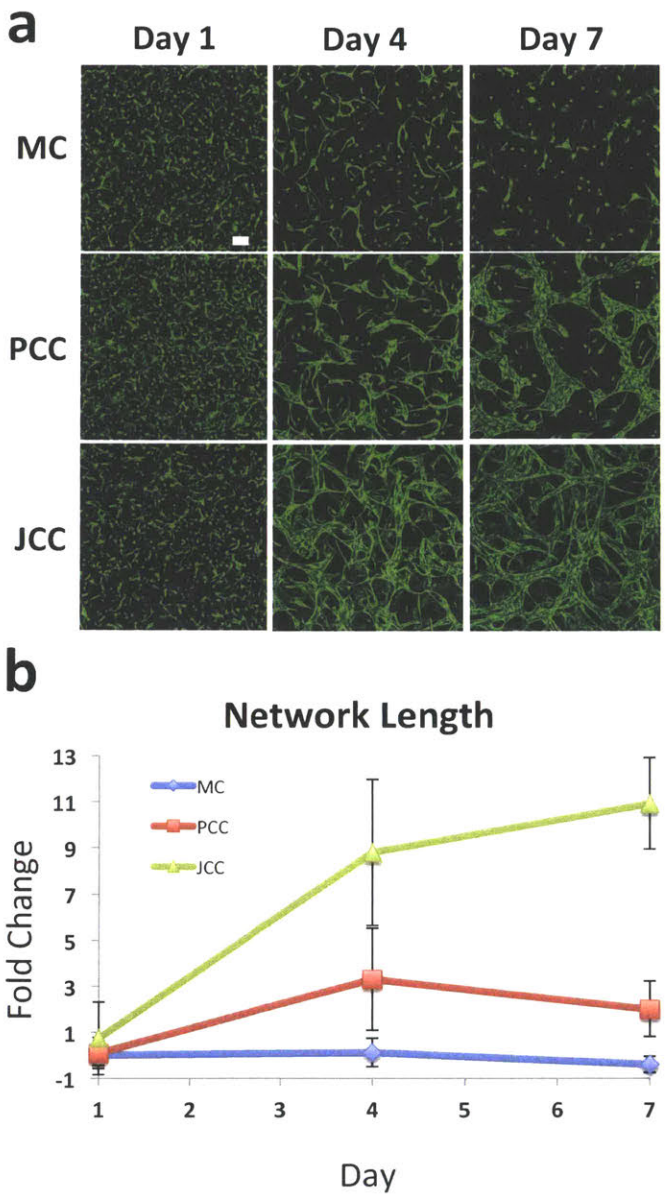

multicellular, "sheet-like" clusters. Juxtacrine co-culture with FB resulted in highly connected networks, with thin, well-defined vessels. Quantifying the length of the longest connected network, we found that the JCC condition resulted in vascular networks that were significantly more connected than the others (Figure 3-2b).

Figure 3-2 Co-culture morphology comparison. (a) Confocal projections of GFP HUVEC for different co-culture conditions. Scale = 100 μm. (b) Length of longest connected network normalized to MC day 1 value.

3.2.2 Vascular Function

We further quantified the differences in vascular function between the different co-culture conditions by perfusing the tissues with a fluorescent tracer (Figure 3-3a). We found that both the perfusability and barrier function was significantly enhanced through juxtacrine co-culture (Figure 3-3b-c).

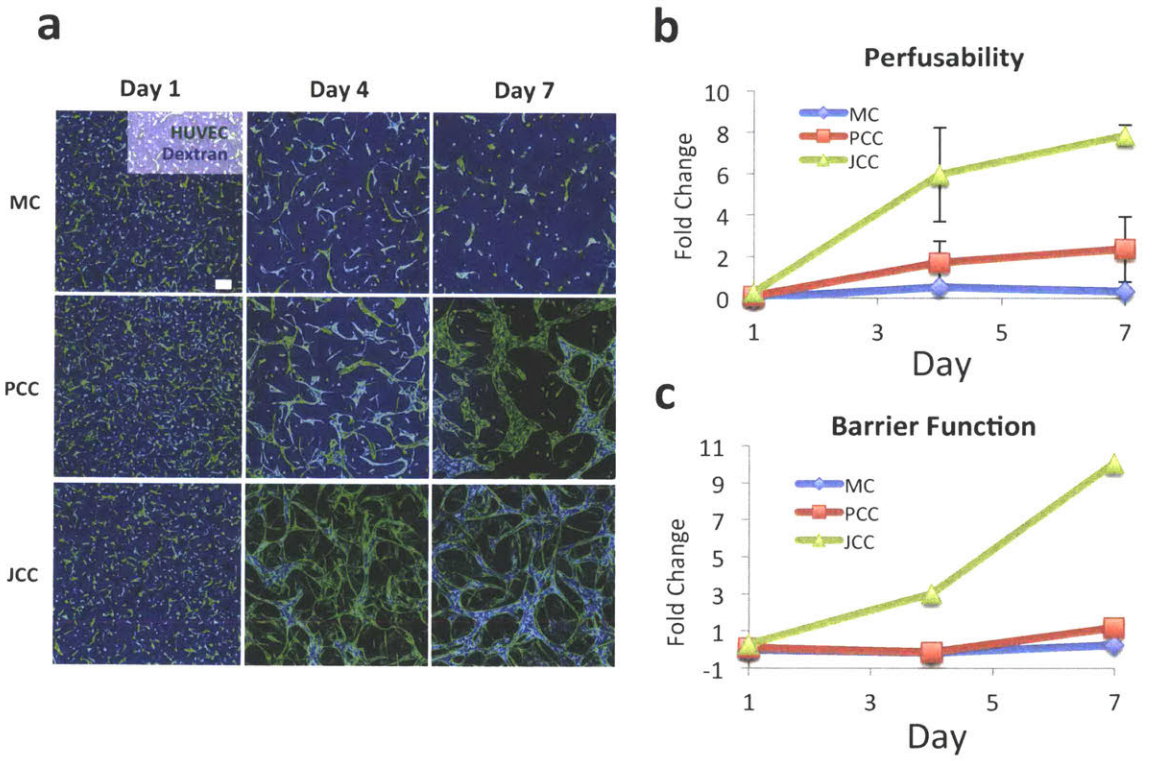

Figure 3-3 Co-culture functional comparison. (a) blue fluorescent tracer dye (70 kDa dextran) introduced from left side of vascularization channel (see Figures 2-6 and 2-14); For fully formed vasculature, dextran flows into vessels and remains contained (i.e. JCC Day 4, 7). For unformed vasculature, dextran flows into interstitial fibrin gel (i.e. MC Day 1, 4 ,7). Scale = 100 μm. (b) perfusability calculated as percentage overlay of GFP (HUVEC) and Blue (dextran) channels, normalized to MC day 1 value. (c) barrier function, calculated as inverse of increase in average dextran concentration of interstitial gel, normalized to MC day 1 value.

Notably, paracrine co-culture did result in increased network length, perfusability, and barrier function when compared to ECs cultured alone, but to a significantly lesser degree

than with juxtacrine co-culture. This implies that soluble factors secreted from FBs are beneficial to vascular morphogenesis but not sufficient to achieve the optimal state.

We then performed additional experiments to support this conclusion. To rule out the possibility that higher concentrations of FB secreted growth factors were needed to improve vascular morphogenesis to the level of JCC, we increased the amount of FBs in the system up to a factor of four. We found no significant increase in vascular network length by increasing the number of FBs (Figure 3-4).

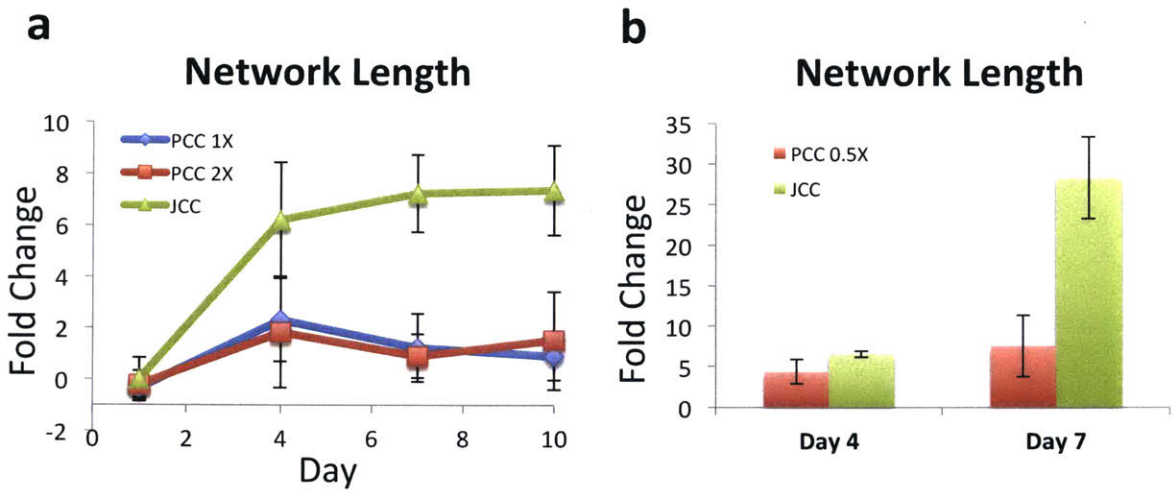

Figure 3-4 Effect of PCC FB seeding density. (a) PCC 1X – equal number of FB and EC; PCC 2X – twice as many FB as EC. Longest connected network length, normalized to MC day 1 value. (b) PCC 0.5X – twice as many EC as FB. Longest connected network length, normalized to MC value at each day (i.e. Day 4 and Day 7).

3.2.3 Conditioned Medium

Finally, we sought to rule out the possibility that soluble factors were indeed responsible for the JCC enhancement of vascular morphogenesis, but that these factors were only secreted through juxtacrine interactions between the two cell types. To do this, we collected conditioned medium from JCC devices, and applied it to MC devices. We found that conditioned medium from JCC devices was not able to replicate the beneficial effects of actual juxtacrine co-culture (Figure 3-5).

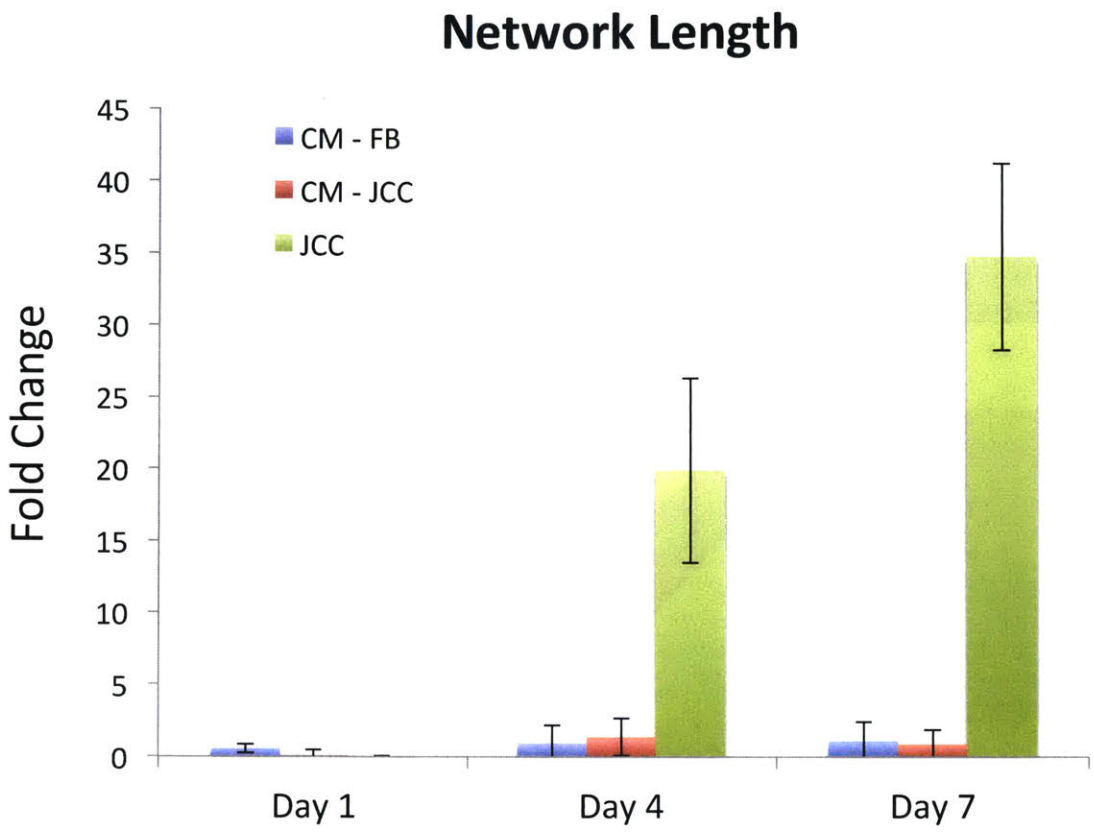

Figure 3-5 Conditioned medium experiments. Conditioned medium applied to MC devices. CM – FB: conditioned medium collected from FB encapsulated alone in fibrin gel; CM – JCC: conditioned medium collected from JCC devices. Longest connected network length, normalized to MC value at each day (i.e. Day 1, Day 4 and Day 7).

3.2.4 Physical Interaction

To better understand the nature of the heterotypic, juxtacrine interactions between ECs and FBs, we performed high-resolution confocal imaging of individual vascular segments (Figure 3-6b). We found evidence of direct, physical interaction, characterized by the longitudinal elongation of FBs along the external vessel walls **(**Figure 3-6c**)**, similar to the interactions observed between ECs and pericytes or smooth muscle cells *in vivo*. Additionally, we observed individual FBs extending and contacting multiple vessels at once (Figure 3-6d). These interactions provide a mechanical and signaling linkage that could allow for coordination of the vasculature at the network level and may aid in vascular morphogenesis and stabilization.

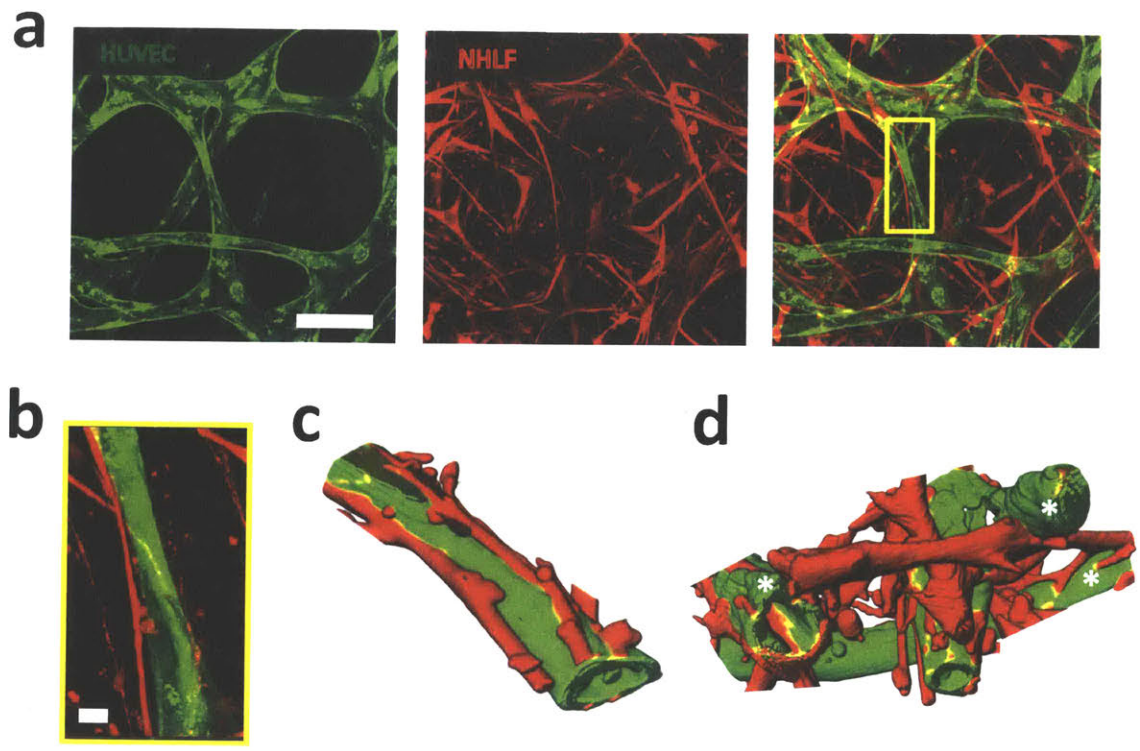

Figure 3-6 Visualization of EC-FB interactions. (a) Confocal image projection of JCC condition. Scale = 100 μm. (b) Close-up image of FB extended along EC vessel. Scale = 10 μm. (c) 3D reconstruction of (b). (d) 3D reconstruction showing single FB contacting multiple vessels. * connotes region of contact.

3.3 Methods

3.3.1 Cell Encapsulation

For co-culture comparison experiments, the fibrin gel density (3 mg/ml) in all three encapsulation channels, the EC seeding density (4 M/ml) in the central vascularization channel, and the FB seeding density (2 M/ml) were held constant for all three conditions (Table 3-1).

Table 3-1 Seeding densities for co-culture comparison experiments.

Condition	Cell Encapsulation Channel (Left)	Vascularization Channel	Cell Encapsulation Channel (Right)
MC		EC – 4 M/ml	
PCC	FB – 2 M/ml	EC – 4 M/ml	FB – 2M/ml
JCC		EC – 4 M/ml FB – 2 M/ml	

3.3.2 Conditioned Medium Experiments

For conditioned medium experiments, JCC devices were seeded with 8 million EC/ml and 4 million FB/ml and MC devices were seeded as usual. Every 24 h after seeding, the supernatant was retrieved from the JCC device perfusion channels and diluted 1:1 with fresh growth medium – to replenish nutrients depleted over that interval. The supernatant from the MC perfusion channels was removed and replaced immediately with the JCC conditioned medium. Conditioned medium from FB only devices was also applied to separate MC devices for comparison.

3.3.3 2D Network Length

To quantify network length, fluorescent images of GFP HUVEC were acquired at 3 separate locations throughout a device with a 4X objective – corresponding to a region of interest of 2.2 x 1.7 mm – on an epifluorescent microscope. Images were processed, binarized, and skeletonized using ImageJ, and the 'Analyze Skeleton' plugin was used to calculate the length of all connected networks (Figure 3-7; See Appendix 3 for full macro script). The longest connected network was used to determine network length.

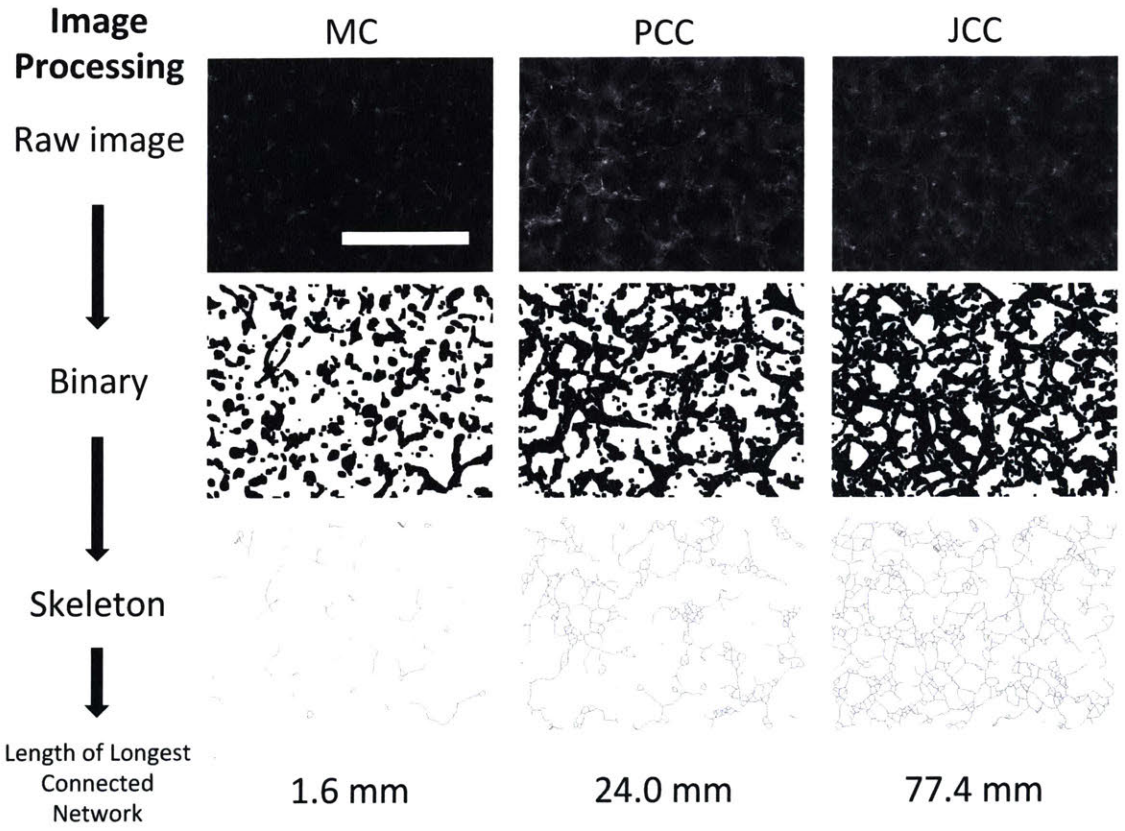

Figure 3-7 2D network length image analysis. Epi-fluorescent images taken of EC (GFP) channel. Length of longest connected network calculated using automated analysis. Scale = 1 mm.

In some cases, a similar procedure was performed for 3D image stacks acquired with a 10X objective on a confocal microscope, by first collapsing the stacks to a 2D projection. See Appendix 3 for full imageJ macro script.

3.3.4 2D Perfusability

To calculate perfusability, confocal stacks of tracer-filled vasculature (Figure 3-8) were collapsed by z-projection onto the x-y plane. The GFP channel (HUVEC) was binarized and used as a mask to define the vascular space. The blue (tracer) channel was binarized - using the overall image average tracer intensity as a threshold - and used to determine the

perfused regions. The two binary masks were then overlayed to calculate the percentage of vasculature that was perfused (Figure 3-8; See Appendix 3 for full macro script):

$$Perfusability = \frac{GFP \cap Blue}{GFP} = \frac{Vasculature \cap Tracer}{Vasculature}$$

All values were normalized to the day 1 monoculture condition.

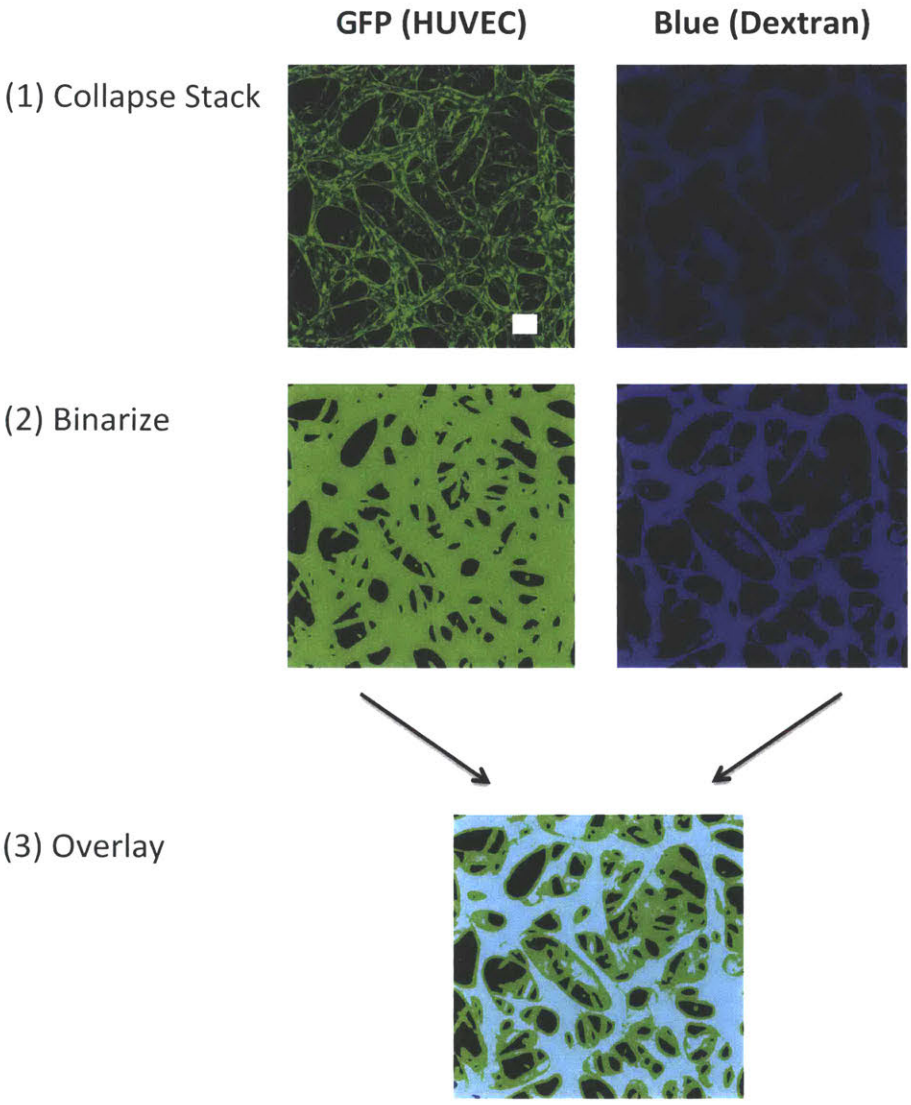

Figure 3-8 2D perfusability image analysis. Perfusability calculated as percentage overlay of tracer (blue) with HUVEC (GFP). Scale = 100 μm.

3.3.5 Barrier Function

To calculate barrier function, confocal stacks of tracer filled vasculature (Figure 3-9) were collapsed by z-projection onto the x-y plane. The GFP channel (HUVEC) was binarized and used as a mask to define the vascular space, and the inverse region(s) was used to define the interstitial space. The average intensity of fluorescent dextran in the interstitial region was calculated for an image taken one hour after introduction of the tracer dye (See Appendix 3 for full macro script). The inverse of this value was used to quantify barrier function:

$$Barrier\ Function = \left[\bar{I}_{blue,int}^{t=1\ hr}\right]^{-1}$$

where,

$\bar{I}_{blue,int}^{t=1\ hr}$ is the average blue (tracer) fluorescence intensity in the interstitial space after one hour.

All values were normalized to the day 1 monoculture condition.

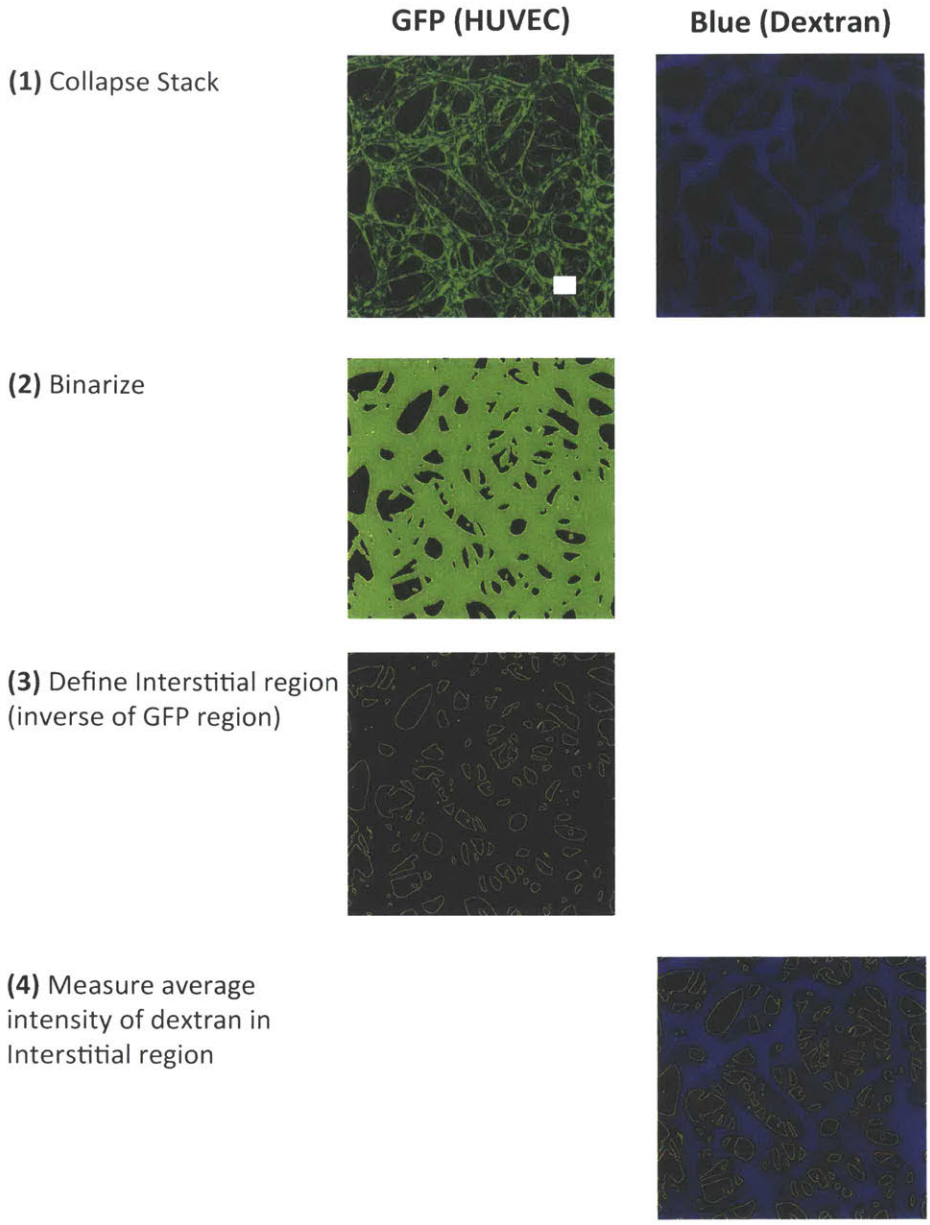

Figure 3-9 2D barrier function image analysis. Barrier function calculated as inverse of the increase in fluorescent tracer intensity in interstitial region. Scale = 100 μm.

4 Mechanical Properties

4.1 Introduction

Mechanical properties of the larger vessels are well characterized due to their need to withstand large pressures and flow rates. At the level of the microvasculature, however, the emphasis of characterization is typically on morphological and transport properties related to the local delivery of nutrients and oxygen. During the course of our experiments, we observed significant physical changes to the vascularized tissue at the macroscopic scale. At the very early stages of vascular assembly, the tissue consistency was that of a soft hydrogel that would easily break apart if external force was applied. However, as vascular morphogenesis progressed, the tissue became stiff and cohesive and maintained its structural integrity when deformed. An elastic response was observed for applied strains up to 50%. Since the biological function of cells is known to be modulated by substrate stiffness[183,184], we sought to characterize the intrinsic stiffness changes that occur during vascular morphogenesis in an effort to better understand their effects on both the vasculature and the surrounding tissue.

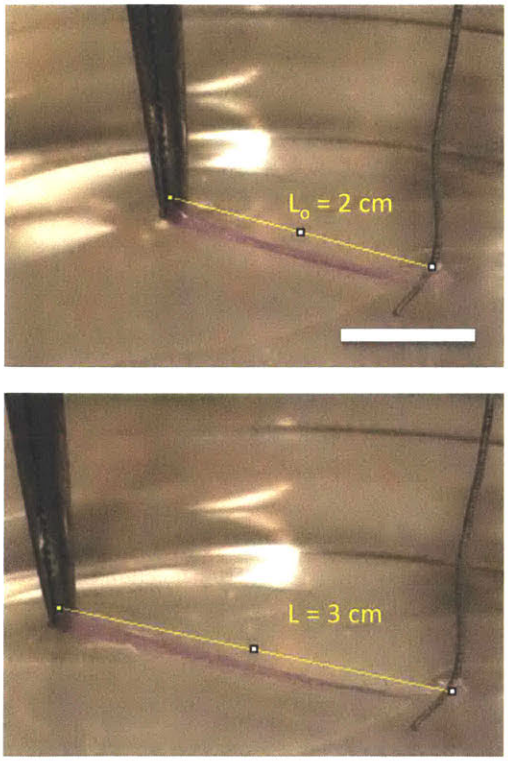

Figure 4-1 Manual tissue stretching. Tissue removed from fluidic device after 2 weeks of culture and submerged in buffer. Anchored at one end with wire; clamped and pulled at other end. 50% strain achieved without permanent deformation.

4.2 Results

4.2.1 Juxtacrine Induced Stiffening

We used atomic force microscopy (AFM) to measure the stiffness changes over time and found a significant increase occurring over the course of 1 week, from 100 Pa at day 1 to 800 Pa at day 7 (Figure 4-2). To check whether this stiffening could be accounted for by the natural tendency of individual cells to contract the ECM, we also measured the stiffness of ECs or FBs seeded independently in a fibrin gel. ECs alone did not induce any significant increase in the tissue stiffness, while FBs induced a modest 2-fold increase, significantly less than for the case of juxtracrine co-culture. Thus, the intrinsic stiffening that occurs during vascular morphogenesis results from the collective assembly of a functional vasculature and synergistic interactions between ECs and FBs. To further validate this, we measured the stiffness of the vasculature formed through paracrine co-culture and found that it increased by only 50% from day 1 to day 7. This implies that the stiffening is indeed correlated to enhanced vascular morphology and function.

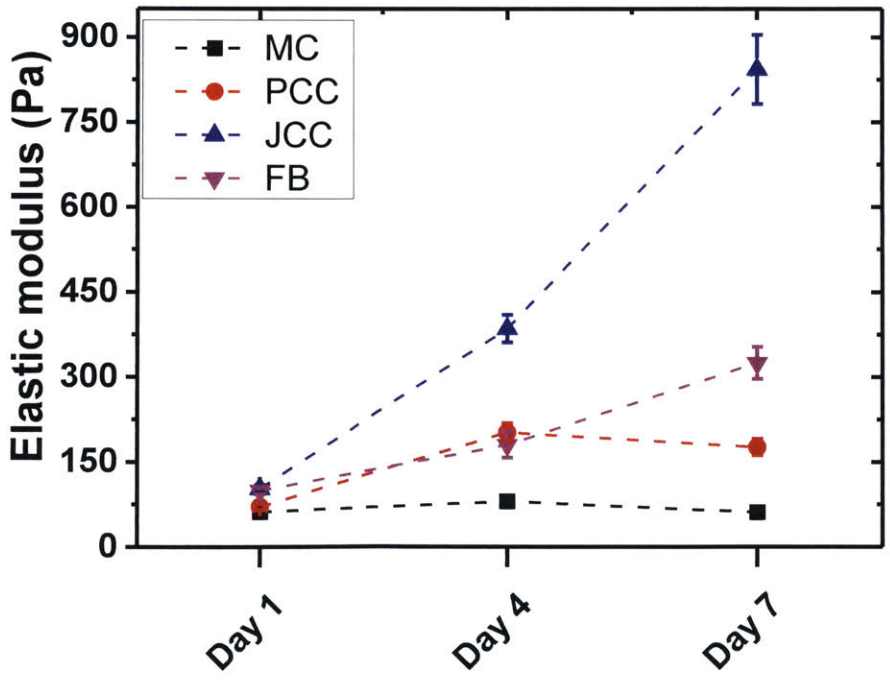

Figure 4-2 Tissue stiffening as a function of co-culture condition. Stiffness measured with AFM.

We then carried out stiffness measurements for the optimal condition of juxtacrine co-culture over a period of 2 weeks of vascular development (Figure 4-3). The stiffness effectively plateaued after 1 week, reaching a maximum value just over 1 kPa at day 10. This corresponded to a 20-fold increase in stiffness compared to non-vascularized fibrin gel.

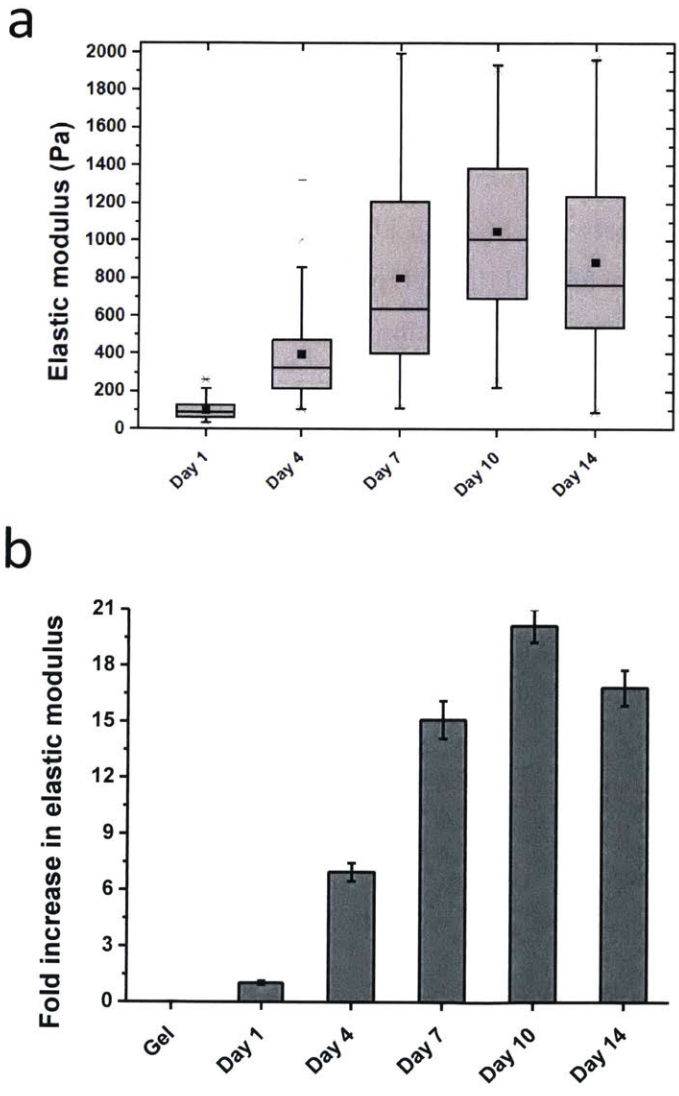

Figure 4-3 Tissue stiffening for JCC condition (AFM). (a) absolute stiffness measurements. (b) fold increase of stiffness compared to cell-free fibrin gel.

We compared the stiffness profile with respect to time to the corresponding morphological and functional profiles for JCC (Figure 3-2 and Figure 3-3). Whereas the morphological (vascular network length) properties plateaued after 4 days, the functional (permeability) and mechanical properties showed significant increases between day 4 and day 7, before reaching a plateau – suggesting that further functional development and stabilization occur after the initial vascular patterning, and they are correlated to the stiffening of the tissue.

4.2.2 Active Stiffening

We hypothesized that the increased stiffness resulted from active force generation by the vasculature generating a contractile pre-stress in the tissue. To test this, we inhibited cellular force generation by treating the tissue with cytochalasin-D (cyto-D; Sigma), a known inhibitor of actin polymerization. Indeed, for tissues treated with cyto-D, the average stiffness at each time point was reduced by roughly 50 percent (Figure 4-4b).

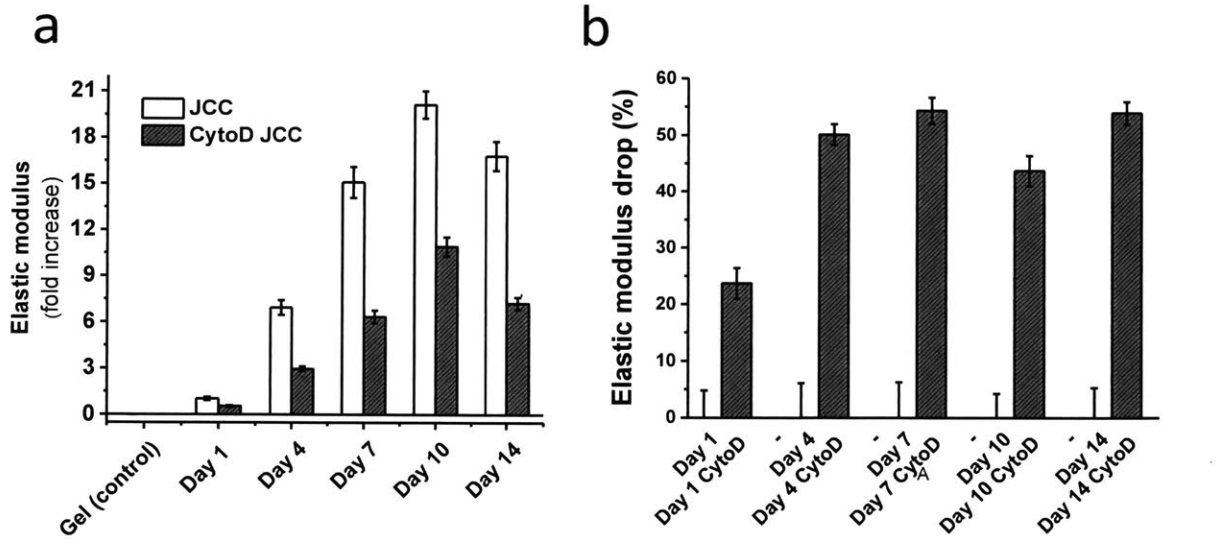

Figure 4-4 Active stiffening (AFM). (a) fold increase of tissue stiffness compared to cell-free fibrin gel for JCC (control) and JCC treated with cytochalasin-D to disrupt cytoskeleton and associated force generation. (b) quantification of % decrease cyto-D treatment relative to control in (a).

To directly confirm the presence of active force generation, we performed 3D traction force microscopy to visualize and quantify the local, reversible deformations imposed by the

vasculature on the surrounding matrix. The magnitude of this deformation increased throughout the course of vascular morphogenesis, following the same trend as stiffness, and further corroborating our hypothesis (Figure 4-5).

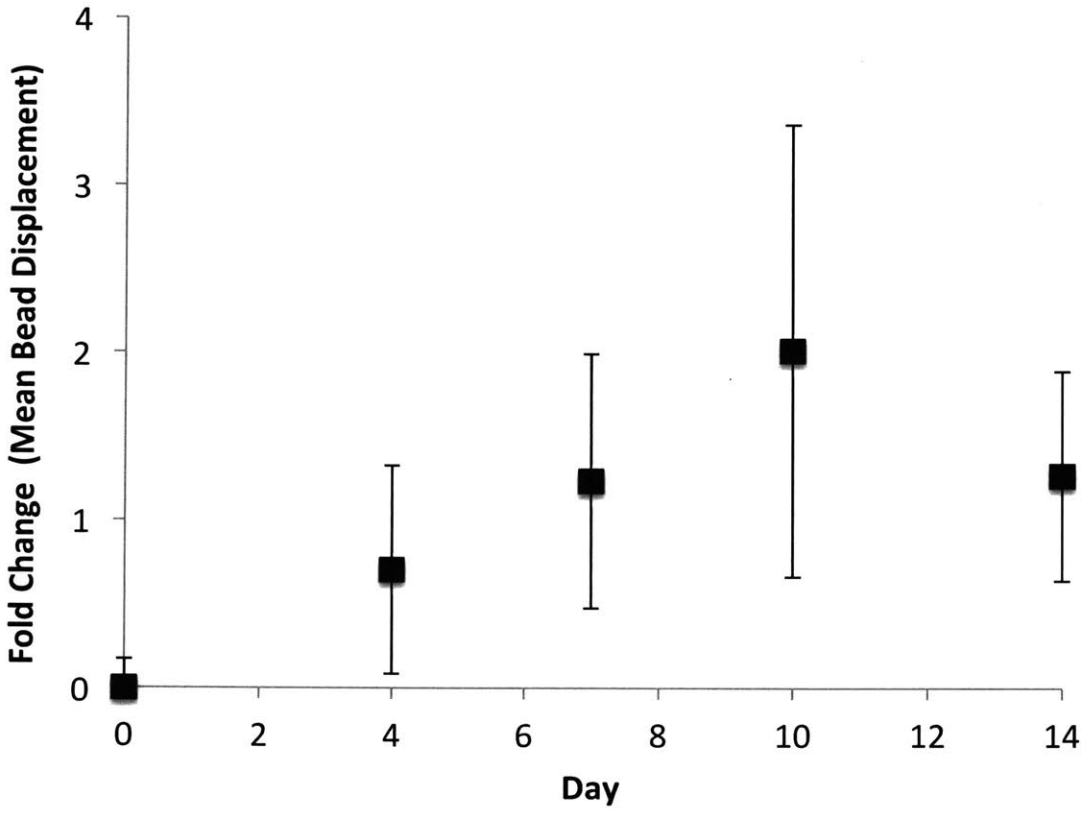

Figure 4-5 3D traction force measurements. Mean displacement of fluorescent beads attached to the hydrogel after relaxation of cells. Fold change with respect to value at Day 0 – immediately after seeding. Displacement is proportional to active tissue pretension.

4.2.3 Passive Stiffening

We speculated that the residual stiffness increase remaining after cytoskeletal disruption could be accounted for by the passive contribution of cellular material. To test this, we decellularized the tissue and again performed AFM measurements. We found that the average stiffness at each time point was further reduced by an additional 20%, for a total of 70% (Figure 4-6b).

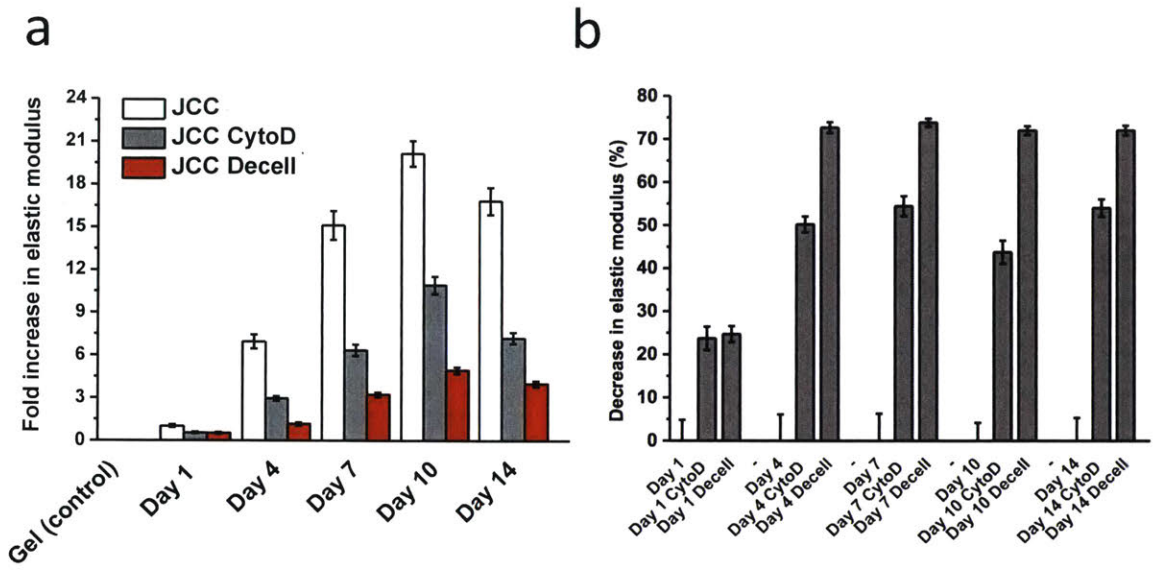

Figure 4-6 Passive stiffening (AFM). (a) fold increase of tissue stiffness compared to cell-free fibrin gel for decellularized tissue (JCC Decell); (b) quantification of % decrease Decell treatment relative to control in (a).

To summarize, AFM measurements revealed that tissue stiffness increased 10-fold over the course of vascular morphogenesis. 50% of the increase was due to active force generation by the vasculature, and an additional 20% was due to the passive contribution of cellular material. We concluded that the remaining 30% of the stiffening was caused by irreversible changes to the matrix. In chapter 5, we explore, in detail, those structural and compositional changes to the matrix that contribute to this stiffening. Interestingly, we confirmed that the extent of irreversible matrix stiffening we observed could not be accounted for by ECs or FBs alone, again demonstrating the synergistic effects of juxtacrine interactions that emerge during vascular morphogenesis (Figure 4-7).

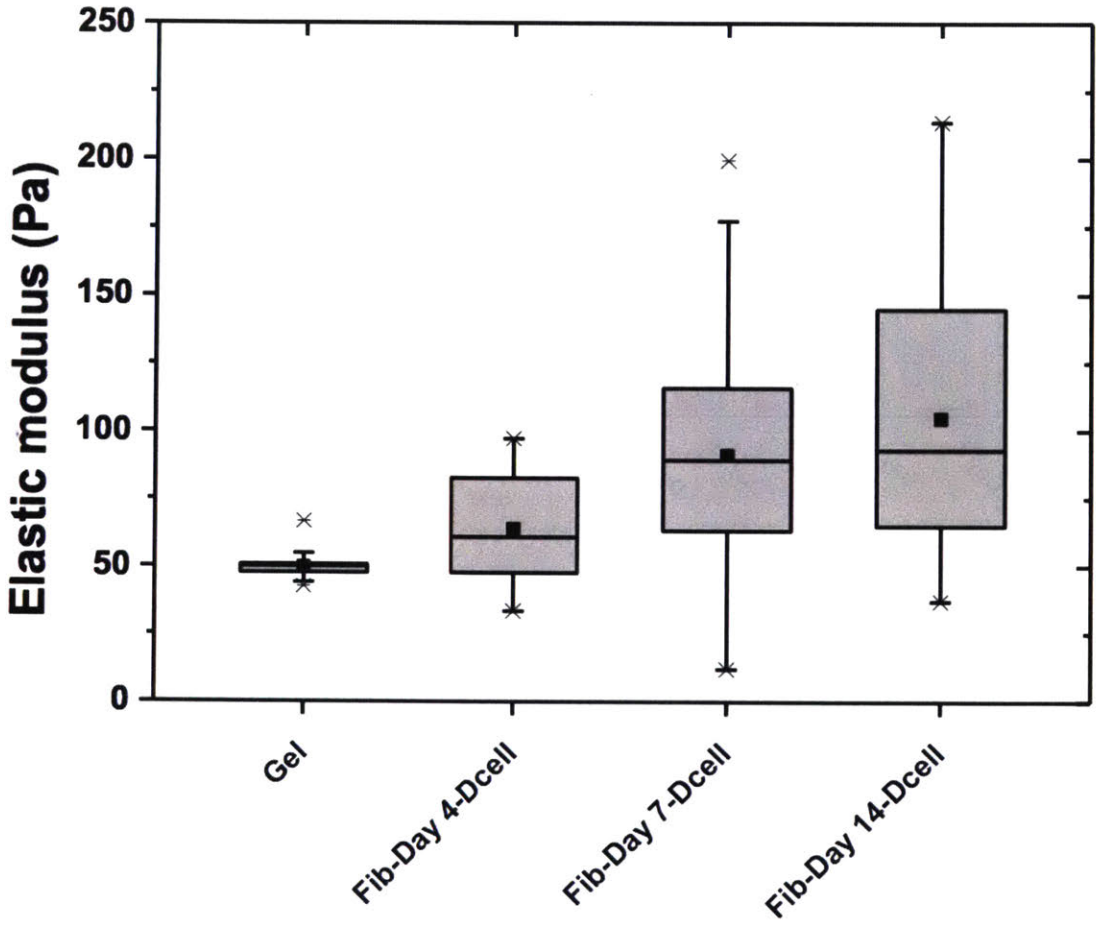

Figure 4-7 Matrix stiffening FB mono-culture (AFM). Absolute stiffness measurements for fibroblast-only tissue constructs after decellularization.

4.3 Methods

4.3.1 Tissue Removal From Device

The tissue was removed from the fluidic device by cutting through the PDMS with a scalpel (Bard-Parker) along the perimeter of the vascularization channel, and slowly peeling it from the glass coverslip (Figure 4-8a-b). The tissue remained intact and adherent to the PDMS upon removal (Figure 4-8c-d).

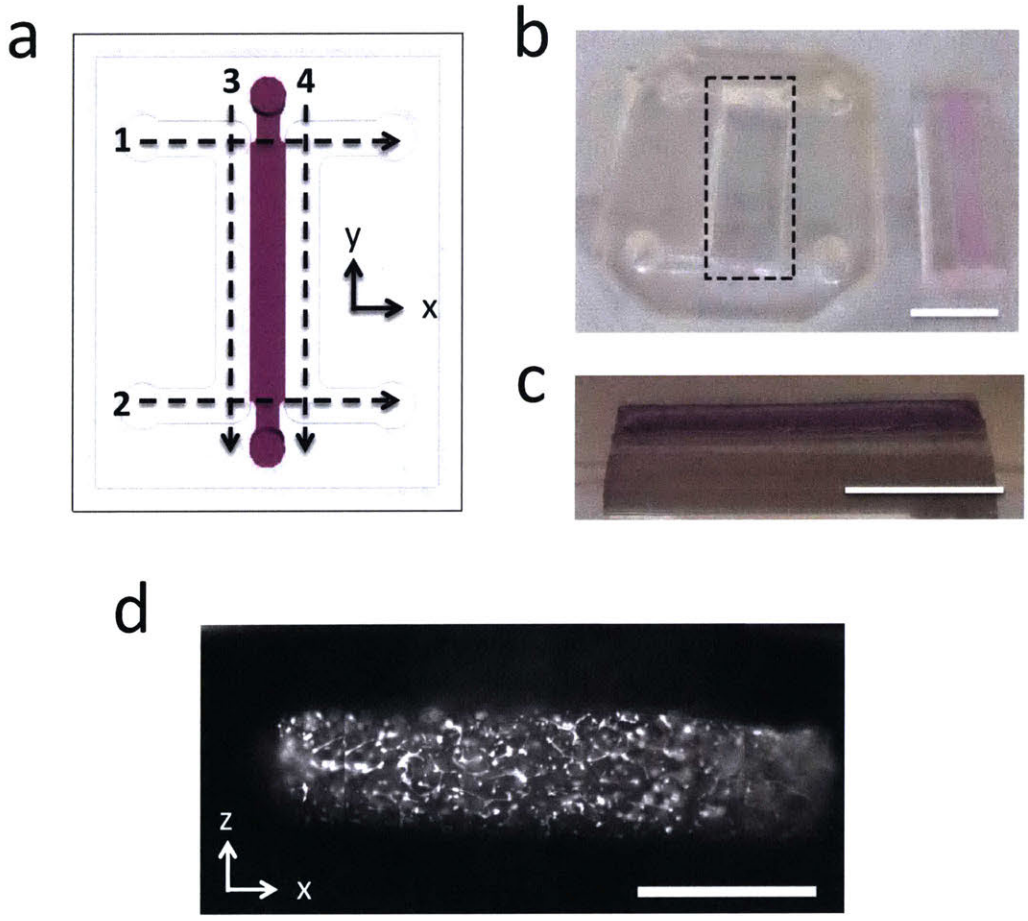

Figure 4-8 Tissue removal from device. (a) 4 cuts with scalpel through PDMS around the tissue vascularization channel. Cuts are made along fluidic channels where PDMS is not bonded to glass coverslip. (b-c) photo of tissue after cutting and peeling from glass coverslip. Tissue remains attached to PDMS. Scale = 1 cm. (d) Cross-section of tissue after removal from device, still attached to PDMS base. AFM measurements made at the top surface. Scale = 1 mm.

4.3.2 AFM Measurements

For AFM measurements, the tissue was left attached to the PDMS which provided a supportive base and helped maintain the original tissue geometry. The entire sample was submerged in a CO_2 – independent medium, consisting of Leibovitz's L-15 Medium without phenol red (Gibco Life Technologies), and supplemented with 10% FBS (Invitrogen).

AFM force-distance measurements were acquired using a JPK Nanowizard Cellhesion 200 (JPK Instruments AG, Berlin, Germany) placed on an inverted optical microscope (Zeiss Axiovert 200) with manual xy-positioning stage. Tipples cantilevers (MLCT-O10, Bruker; nominal spring constant of 0.07 N/m) were modified by gluing 50 μm diameter glass microspheres (Cospheric, USA) to the tip of the cantilever via UV curing glue (ultraviolet curing, Loctite). Prior to gluing the beads, spring constants of the cantilevers were determined using the thermal noise method of the AFM software (JPK SPM, JPK instruments). The stage was carefully moved to position the cantilever tip above the middle of the sample prior to approaching the tissue surface. No less than 50 force-distance curves were taken per sample by moving the stage manually (in ~0.5 mm steps) across the length of the tissue, with an approach speed of 10 μm/s and a set force of 30 nN.

4.3.3 Data Analysis

Using a custom-written MATLAB (Mathworks) routine, the contact point and subsequently the force-indentation curve were extracted from the force-distance curve [185]. The apparent elastic modulus $E/(1-\nu^2)$ was extracted by fitting the force-indentation curve to a Hertz contact model between a sphere and an infinite half space [186]. Considering the size of the glass bead, the applied maximum force was chosen to apply sufficiently large indentations and probe the stiffness of the gels and vascular tissue constructs on a length-scale that is larger than the size of individual cells while also adhering to small strain conditions [187], thus providing the macroscopic level average elastic modulus of the constructs. Setting the maximum force to 30 nN resulted in average indentation depths δ ~7μm and maximum of δ ~25μm (for the softest samples such as cell-free fibrin gels). The average contact size was ~30 μm and the analysis of force-indentation curves was limited to a maximum indentation depth of 10 μm.

4.3.4 Cytoskeleton Disruption

After performing initial stiffness measurements on the tissue, Cytochalasin D (Sigma) was added to the medium at a concentration of 4μM, to inhibit active force generation through the inhibition of actin polymerization. New measurements were performed after 15 m of incubation.

4.3.5 Decellurization

The tissue was washed several times with PBS, and then incubated in decellurization buffer – consisting of 0.5% Triton X100 and 11 mM ammonium hydroxide – for 1 hr. The tissue was then washed several more times and again submerged in Leibovitz's L-15 Medium for additional stiffness measurements.

4.3.6 3D Traction Force Microscopy

3D TFM was performed by embedding 1 μm fluorescent beads in to the fibrin gel during cell encapsulation in the fluidic device. The beads became immobilized in the gel pores and did not interfere with vascularization (Figure 4-9). To perform a measurement at any given time point, the fluidic device was placed on a confocal microscope stage, and a 400 x 400 x 100 micron ROI was imaged to identify the initial bead positions. Without moving the device, cytochalasin D or decellularization solution was added to the device and left to incubate for 1 hr. After 1 hr, the same ROI was imaged again. 3D bead tracking analysis was performed with Imaris software to automatically identify the initial and final positions of individual beads, and to subsequently calculate the bead displacements. The displacements of all beads within a ROI were averaged together and the mean displacement was reported as a fold change with respect to day 0.

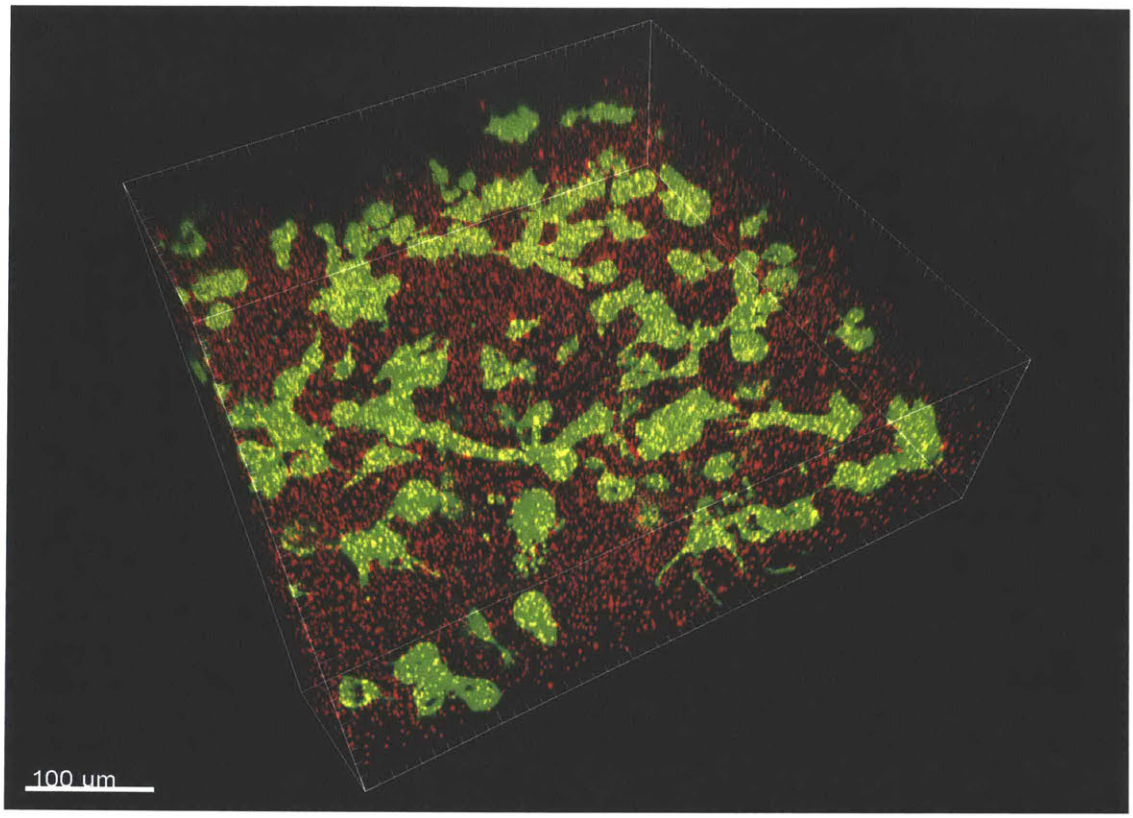

Figure 4-9 Traction Force Microscopy. 1 μm red fluorescent spheres embedded into fibrin gel during cell encapsulation (GFP HUVEC) to quantify gel displacements after force relaxation. Scale = 100 μm.

5 Extracellular Matrix

5.1 Introduction

As discussed in the previous chapter, irreversible modifications by cells to the ECM during vascular morphogenesis resulted in a nearly 4-fold, permanent increase in matrix stiffness after decellularization. Furthermore, as discussed in Chapter 1, both FBs and ECs are capable of generating and depositing new matrix proteins to facilitate vascular morphogenesis and stabilization. In this chapter, we experimentally investigate the physical and chemical modifications to the matrix that arise through intrinsic interactions with vascular cells and their correlation with enhanced vascular morphogenesis.

5.2 Results

5.2.1 Structural Remodeling

Using confocal reflectance microscopy, we visualized the ECM structure throughout the course of vascular morphogenesis and observed several significant changes over time (Figure 5-1a). Cells degraded or physically moved the matrix to form voids in which they subsequently spread and formed lumens. At the perimeter of the lumens, between the vessel wall and the bulk matrix, a thin boundary of dense matrix fibers was formed. We also observed local alignment of individual fibers within the bulk matrix between vessels. Quantification of these phenomena with image analysis confirmed that both the average thickness and alignment of the matrix fibers increased during vascular morphogenesis – most significantly at the perivascular interface (Fig 5-1b-c). The increased matrix density surrounding the vascular voids likely increased the local stiffness there and contributed to the increase in matrix stiffness we observed with AFM (Figure 4-6).

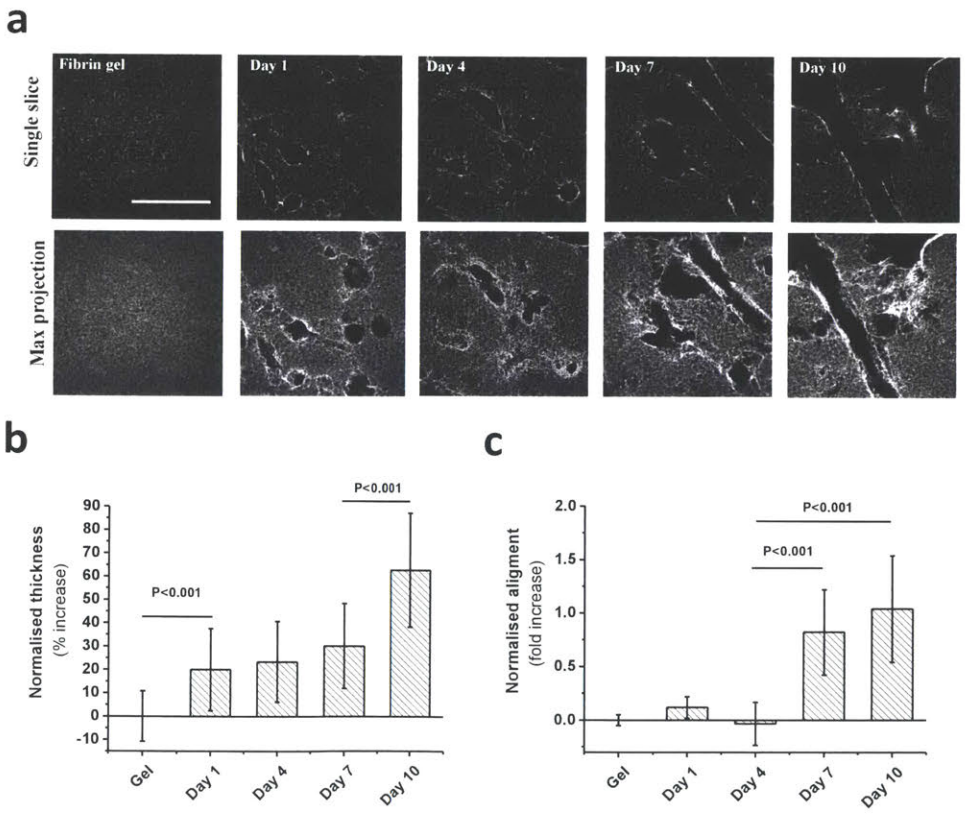

Figure 5-1 ECM structural modifications. (a) confocal reflectance microscopy images of fibrin gel fiber structure over time. Images acquired after decellularization. Thick bundles of fibers can be seen at the edges of voids previously occupied by cells. Scale = 100 μm. (b) quantification of average fiber thickness over time, normalized to cell-free fibrin gel. (c) quantification of fiber alignment over time, normalized to cell-free fibrin gel.

5.2.2 Compositional Remodeling

5.2.2.1 Protein Content

We performed mass spectrometry proteomics analysis to uncover the compositional changes to the matrix that occur during vascular morphogenesis. We identified over 50 ECM-related proteins that were deposited by the cells. Most of these proteins are associated with one or more of the following vascularization related functions: (a) vasculature development, (b) basement membrane, (c) cell-substrate adhesion, (d) collagen fibril organization, (e) ECM structural constituent, and (f) ECM organization (figure 5-2).

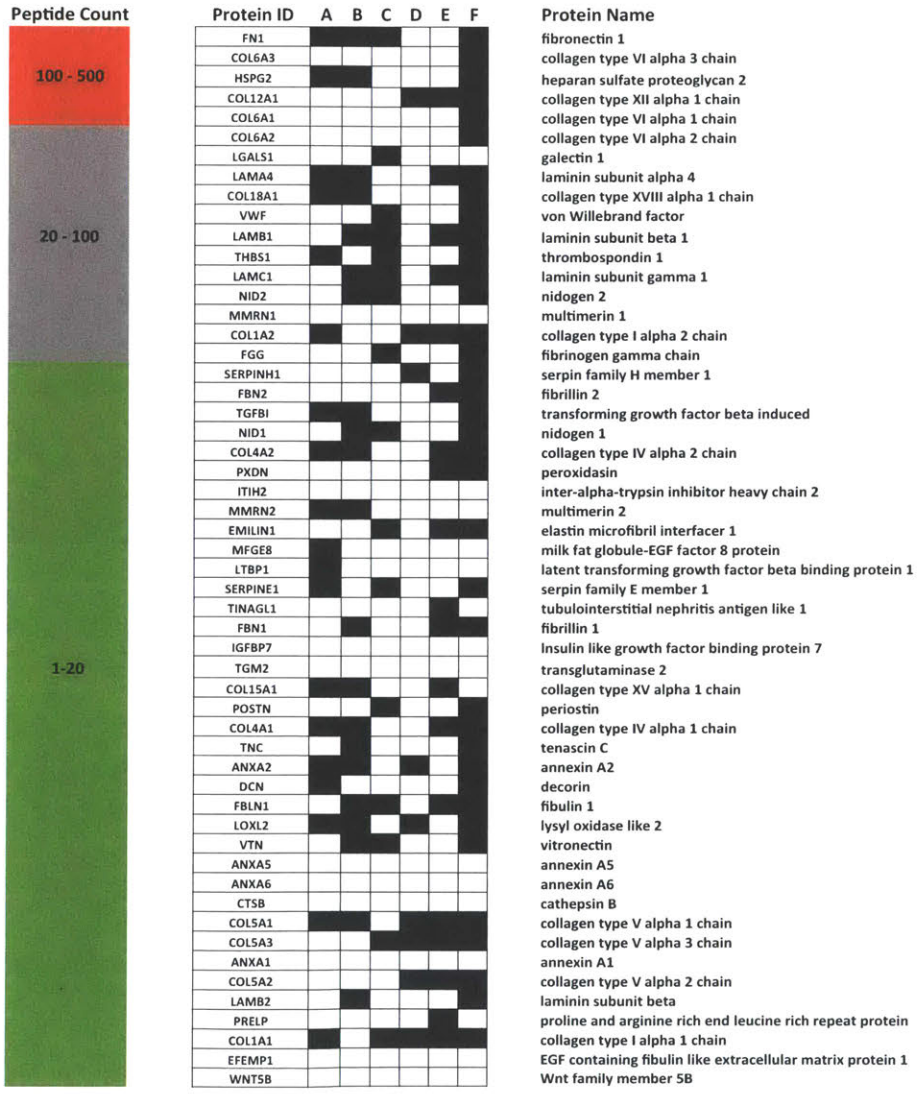

Figure 5-2 Composition of ECM deposited by cells - Mass spectrometry (MS). ECM protein deposition ranked in decreasing order of abundance by total peptide count after 2 weeks of culture. Proteins are categorized according to 6 ontology terms chosen for their relevance to vascularization.

Interestingly, significant deposition of these proteins was not observed when either ECs or FBs were cultured alone (figure 5-3).

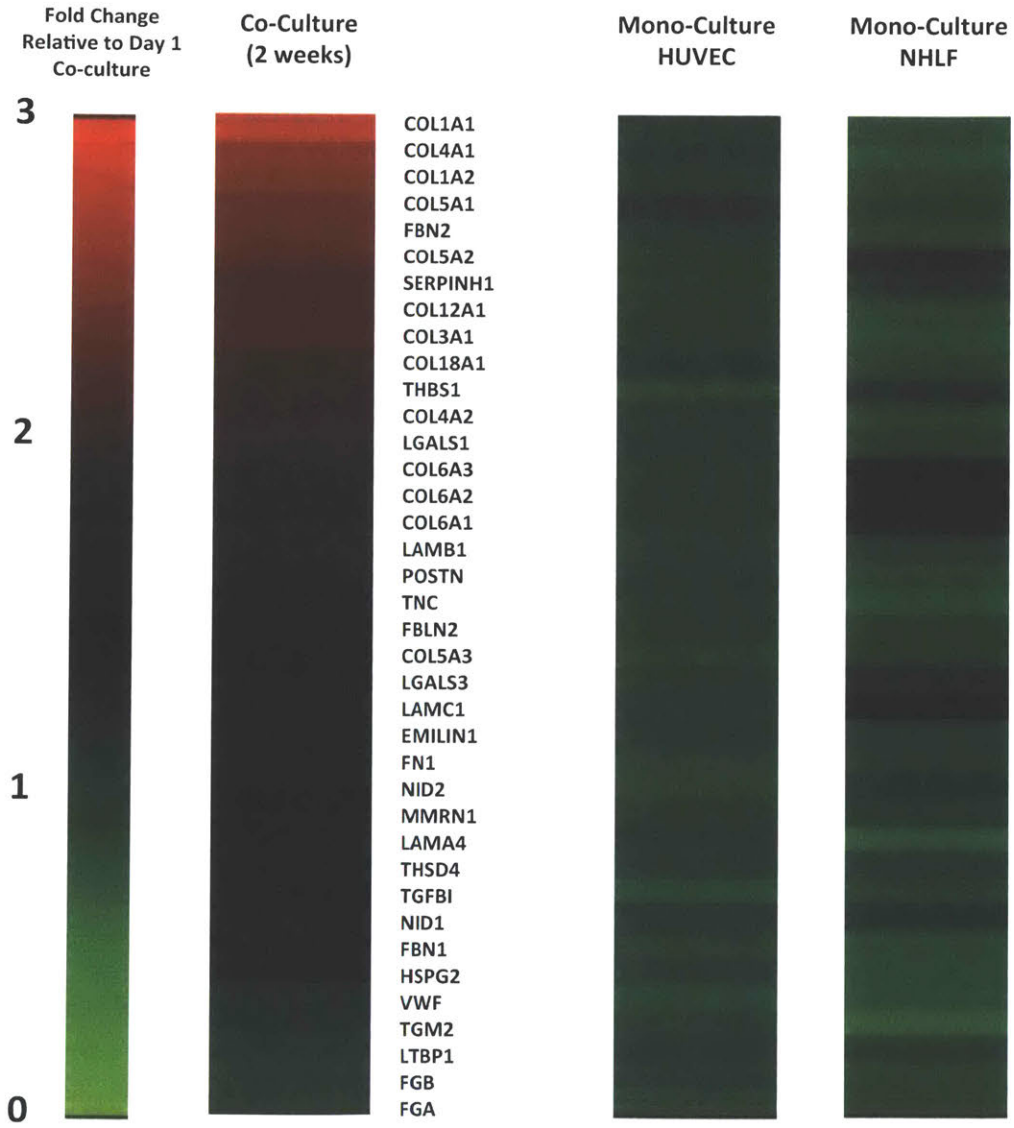

Figure 5-3 Co-culture synergistic ECM deposition - MS. ECM protein deposition ranked in decreasing order of fold change at 2 weeks relative to values at day 1 for JCC condition. Comparison to deposition of those proteins by EC or FB encapsulated alone in fibrin gel. Mono-culture HUVEC data was analyzed for 1 week samples due to limited cell survival beyond that point.

5.2.2.2 Temporal Evolution

We tracked the total peptide content of the matrix over 2 weeks of vascularization and observed a significant and steady increase resulting from new matrix deposition (Figure 5-4). Thus, matrix deposition and reconstitution appears to play an important role throughout the entire process of vascular morphogenesis.

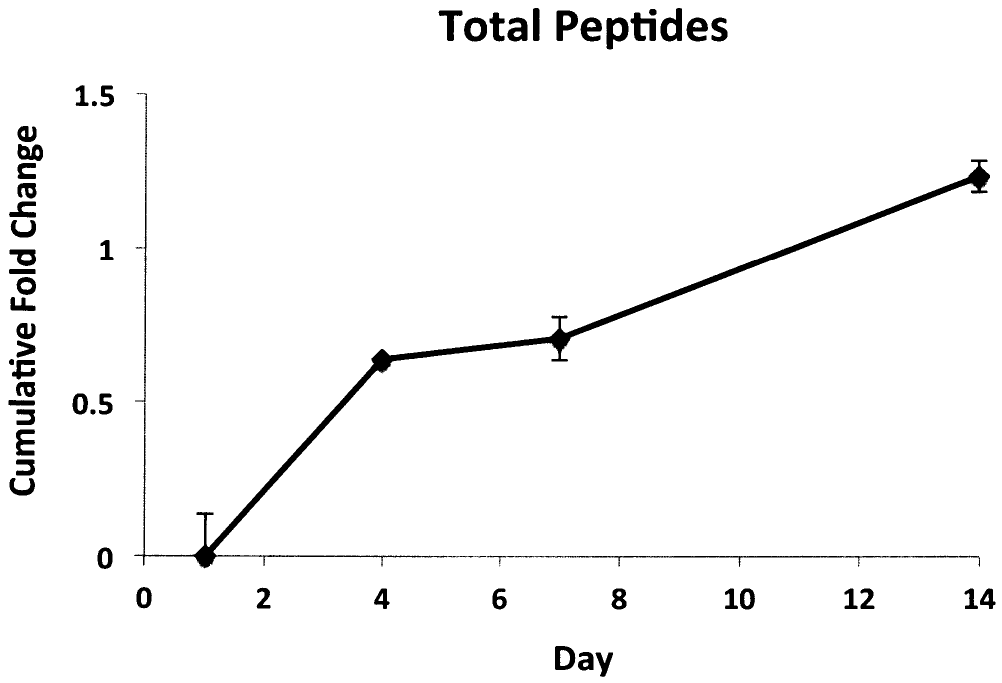

Figure 5-4 Temporal cumulative ECM deposition - MS. Cumulative fold change of total amount of peptides in tissue sample – as identified by MS – relative to value at day 1.

The increase in protein content that we measured likely contributed to the increased matrix stiffness that we observed. Duong et. al.[188] showed - for fibrin matrices - that increasing the fibrinogen concentration from 2 to 5 mg/ml caused a 4-fold increase in matrix stiffness.

Analyzing the temporal deposition profiles of individual proteins, we identified 6 unique patterns and grouped the proteins accordingly (Figure 5-5a). Qualitative temporal trends for cumulative protein deposition are plotted in figure 5-5a for the different groups. Differences between the groups are highlighted when comparing their relative rates of deposition during the 3 intervals of analysis (days 2-4, days 5-7, and days 8-14; Figure 5-5b). The proteins in group A – laminin (β1), fibrillin (2), and 10 different collagen-family

proteins – consistently exhibited high rates of deposition as calculated by fold-change increase with respect to their values at day 1. The proteins in group F, on the other-hand, consistently demonstrated relatively low rates of deposition. Of significant interest, are those groups for which the relative deposition rates were high for specific intervals but not others.

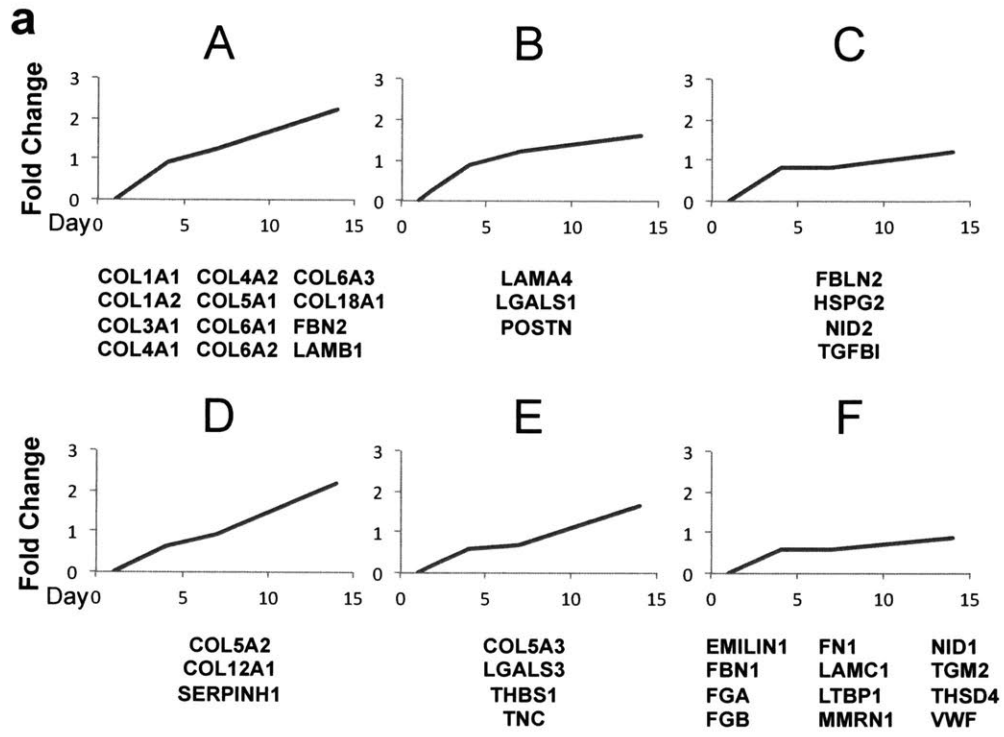

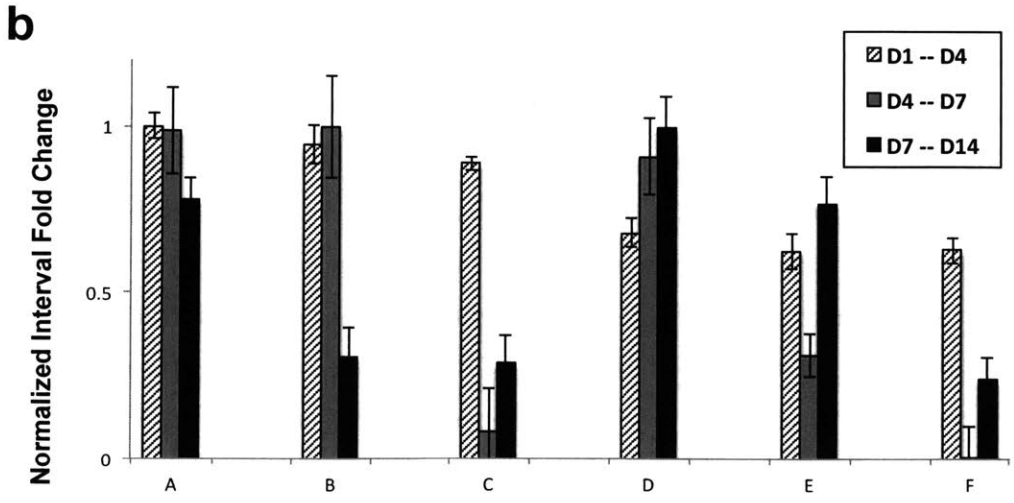

Figure 5-5 Specialized temporal patterns of ECM deposition – MS. (a) groupings of cell deposited ECM proteins based on similar temporal patterns of cumulative deposition. Group average fold change values calculated with respect to day 1. (b) group fold change values during each of three sample collection intervals (Day 1 – Day 4; Day 4 – Day 7; Day 7 – Day 14), normalized to maximum group fold change for each interval. Error bars represent standard error.

The occurrence of these patterns suggests that the cells temporally regulate the composition of their surrounding matrix to optimally achieve vascular morphogenesis and stabilization. For instance, relative deposition rates for proteins in groups B and C were initially high, but decreased significantly by the final interval. Examining the functional roles of the proteins in these groups, we found that they are all components of the basement membrane (LAMA4, HSPG2, TGFBI), important for cell-substrate adhesion (LGALS1, POSTN, FBLN2), or both (NID2). These proteins are critical in the early stages of vascular morphogenesis, enabling the cells to spread and adhere to the 3D matrix and providing the necessary signaling required to maintain their new morphology. Group D, which underwent the highest relative increase of all groups during the final interval, contains collagen-5 (α2) and collagen-12 (α1) – two important structural constituents of the ECM. At the later stages of vascular morphogenesis, in which the active tension increases to its maximum levels, the cells likely deposit these structural proteins to strengthen the matrix to withstand the internally generated forces.

5.2.2.3 Compositional Breakdown

Mass spectrometry is not an inherently quantitative method. Using isobaric labeling – as we did above – it is possible to accurately determine the relative amounts of any specific protein among different samples of an experiment. However, due to differential ionization and MS detectability among peptides, it is difficult to accurately compare the abundance of different proteins within an individual sample. In the last decade, several label-free methods have been developed to estimate these relative abundances based on post-processing of the MS data[189]. Implementing one of these methods – "Top-3"[190] – we found that by 2 weeks of vascular morphogenesis, roughly one-third of the matrix was composed of entirely new proteins deposited by the cells (Figure 5-6a). Of these proteins, the largest single contributors were collagen 1 (27%), fibronectin (17%), and fibrinogen (17%). Other proteins with significant abundance included collagen 6 (9%), collagen 5 (5%), collagen 4 (5%), and perlecan (2%) (Figure 5-6b). More than 20 other proteins were identified with

abundances of less than 1% (Figure 5-6c). It should be noted that a protein's abundance does not necessarily correlate to its functional significance. Many of the proteins deposited with low abundance (< 1%) – i.e. laminin , nidogen, multimerin 2 - locally provide biological signaling that is critical to vascular morphogenesis and stabilization. They are often found in specific anatomical locations – such as the basement membrane – where they constitute a majority of the local matrix composition.

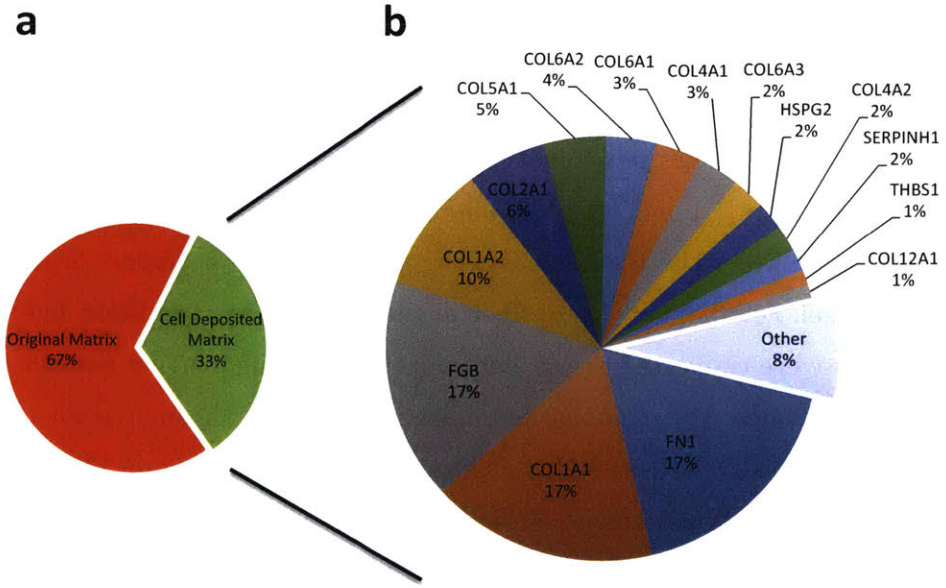

c

Protein	% Abundance
COL3A1	0.97647858
LGALS1	0.704170645
TGM2	0.642129515
COL5A2	0.631111289
FBLN2	0.545986739
FBN1	0.536034975
VWF	0.375244662
TNC	0.326644883
FGA	0.318732821
LAMC1	0.306301189
TGFBI	0.285301301
LGALS3	0.254096645
FBN2	0.23670795
LAMB1	0.217260235
MMRN1	0.205805549
EMILIN1	0.18470855
NID2	0.134200161
LAMA4	0.127471425
COL18A1	0.120043153
NID1	0.102465416
HTRA1	0.101084088
BGN	0.070104514
COL5A3	0.066944428
POSTN	0.062279705
LTBP1	0.055293449
SERPINE1	0.039093088
THSD4	0.03689281

Figure 5-6 Top-3 method: label free quantification of relative composition. Mathematical technique to estimate relative composition of all identified proteins. (a) relative contribution of cell deposited matrix compared to original fibrin matrix. (b) relative composition breakdown of cell-deposited matrix. (c) all cell deposited ECM proteins less than 1% of total cell-deposited matrix (from "other"in (b)).

5.3 Methods

5.3.1 Gel Quantification

Decellularized networks were imaged with a scanning laser confocal microscope (Olympus, FV-1000) using a 63X oil immersion objective lens (Olympus, NA 1.3 oil) and in reflectance mode. Ten single slice images per condition were thresholded and run through the BoneJ plugin for ImageJ (http://bonej.org/) to obtain the average fiber thickness within the decellularized network[191]. The final values were normalized with respect to the values of the intact fibrin gel. For the analysis of fiber alignment, for each condition five maximum projected images were converted to 2D spectrum images using the Fast Fourier transform (FFT) plugin in ImageJ. The transformed images were run through a custom Matlab program to sum the pixel intensities along a straight line from the center to the edge of the transformed images at different angles (from 0^{o} to 180^{o}). The sum of the pixel intensities as the function of angle represent the degree of alignment - with a perfectly random image giving constant intensity and an image with alignment giving intensity peaks at specific angles[192]. The degree of alignment was quantified as the total area under the intensity plots and normalized with respect to the intact fibrin gel.

5.3.2 Mass Spectrometry

We followed previously published methods to digest tissue samples into peptides for mass spectrometry[193] and to perform proteomics analysis on the data for identification of ECM related proteins[194].

Decellularization

To prepare the matrix for mass spectrometry, the tissue was first decellularized to remove the cellular protein contribution. Briefly, the extracted tissue was incubated at 4^{o} C on a shaker for 1 hr in a decellularization buffer consisting of 0.5% Triton X100 and 11 mM ammonium hydroxide. The sample was homogenized using a magnetic bead based,

mechanical homogenizer, and washed thoroughly, several times to remove the decellurization buffer. Samples were then flash frozen and stored at -80^0 C so that further processing of all experimental conditions and replicates could be performed simultaneously. See Appendix 2 for a detailed protocol.

In-Solution Digestion

Sample (1) reduction with DTT, (2) deglycosylation with PNGaseF, (3) digestion with Lys-C and trypsin, (4) and acidification with trifluoro-acetic acid were performed according to the published protocol (REF). Peptides were (5) desalted using the Protea C18 spin tips per manufacturer's instructions and lyophilized.

TMT labeling

Peptide labeling with TMT 10plex (Thermo) was performed per manufacturer's instructions. Lyophilized samples were dissolved in 70 µL ethanol and 30 µL of 500 mM triethylammonium bicarbonate, pH 8.5, and the TMT reagent was dissolved in 30 µL of anhydrous acetonitrile. The solution containing peptides and TMT reagent was vortexed and incubated at room temperature for 1 h. Samples labeled with the ten different isotopic TMT reagents were combined and concentrated to completion in a vacuum centrifuge.

LC-MS/MS

Peptides were separated by reverse phase HPLC (Thermo Easy nLC1000) using a precolumn (made in house, 6 cm of 10 µm C18) and a self-pack 5 µm tip analytical column (12 cm of 5 µm C18, New Objective) over a 140 minute gradient before nanoelectrospray using a QExactive Plus mass spectrometer (Thermo). Solvent A was 0.1% formic acid and solvent B was 80% MeCN/0.1% formic acid. The gradient conditions were 0-10% B (0-5 min), 10-30% B (5-105 min), 30-40% B (105-119 min), 40-60% B (119-124 min), 60-100% B (124-126 min), 100% B (126-136 min), 100-0% B (136-138 min), 0% B (138-140 min), and the mass spectrometer was operated in a data-dependent mode. The parameters for the full scan MS were: resolution of 70,000 across 350-2000 *m/z*, AGC 3e^6, and maximum IT 50 ms. The full MS scan was followed by MS/MS for the top 10 precursor ions in each cycle with a NCE of 34 and dynamic exclusion of 30 s.

5.3.3 MS Data Analysis

Raw mass spectral data files (.raw) were searched using Proteome Discoverer (Thermo) and Mascot version 2.4.1 (Matrix Science). Mascot search parameters were: 10 ppm mass tolerance for precursor ions; 15 mmu for fragment ion mass tolerance; 2 missed cleavages of trypsin; fixed modification were carbamidomethylation of cysteine and TMT 10plex modification of lysines and peptide N-termini; variable modifications were oxidized methionine, deamidation of asparagine, pyro-glutamic acid modification at N-terminal glutamine, and hydroxylation of proline. TMT quantification was obtained using Proteome Discoverer and isotopically corrected per manufacturer's instructions. Only peptides with a Mascot score greater than or equal to 25 and an isolation interference less than or equal to 30 were included in the data analysis. Matrix proteins were determined as previously defined[194].

Temporal Deposition Groupings

To identify unique groupings of temporal protein deposition, fold change increase was calculated for each protein during each of the 3 intervals (D2-D4, D5-D7, D8-D14). The average fold change of all the proteins during each interval was calculated. First, the proteins were divided into 2 groups based on fold change above or below the average for interval 1. Those groups were then subdivided based on fold change above or below the average for interval 2. Finally, those groups were subdivided based on fold change above or below the average for interval 3. Fold-change values for all proteins within a group were averaged together and plotted (Figure 5-5).

To generate the bar graphs in Figure 5-5b, the average fold change for each group during an interval was normalized to the maximum group fold change for that interval.

Top3 Abundance Calculations

Relative protein abundance was calculated using the Top-3 method. Briefly, of all identified peptides mapping to a given protein, those with the largest 3 precursor areas were averaged together and used as the abundance parameter for that protein. The abundance parameter for each protein was divided by the sum of abundance parameters for all proteins to determine its relative abundance.

6 Transcriptional Regulation

6.1 Introduction

In the previous chapters, we observed and characterized the morphological, functional, mechanical, and compositional changes that emerge during vascular morphogenesis. Non-transient changes in these individual properties are manifestations of a global phenotypic transition by the cells that is governed at the level of transcriptional regulation. To decipher the underlying biological program responsible for the observed emergence of microvascular form and function, we isolated and sequenced the RNA from ECs and FBs at various stages of vascular morphogenesis.

In previous studies, RNA expression levels were measured for ECs cultured alone during the initial 48 hours of vascular network assembly[13] and for ECs co-cultured with FB up to 5 days [195]. From our experiments, we identified that significant changes to the microvasculature continue through the second week of development. In a more recent study, the authors analyzed RNA expression for ECs cultured with FB at later stages of development (8 d), but because the cells were not separated prior to the analysis, it is difficult to independently determine the expression changes in each cell type[164]. Our analysis accounts for the long-term phenotypic changes occurring over the course of 2 weeks, and independently tracks those changes in ECs and FBs.

6.2 Results

6.2.1 Endothelial Cell RNA Expression

The distribution of differentially expressed (DE) genes in ECs is plotted in Figure 6-1 (a and c). Over time, both the magnitude of maximum differential expression increased as well as the number of genes differentially expressed at a given level. The total number of DE genes steadily increased before reaching a plateau at day 10 for both up and down regulation – 1294 and 1512 genes, respectively (inset of Figure 6-1 a and c). 80% of the DE genes on day 14 were already differentially expressed on day 10 – suggesting that a stable transition in gene expression occurred by that point.

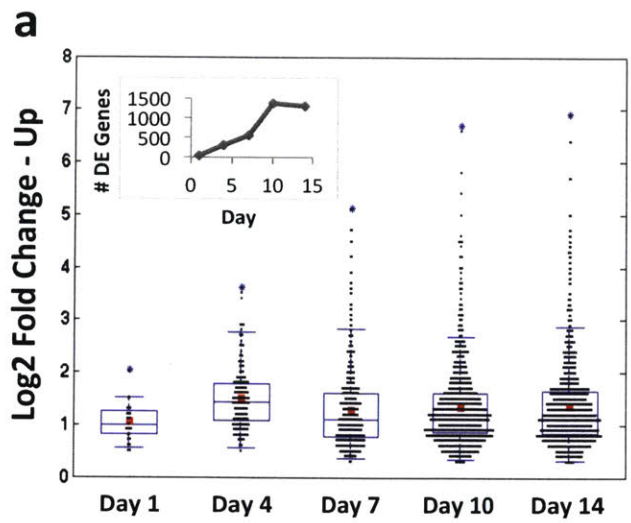

b

Vasculature Development

Gene	Log2FC	Day
APOD	4.3493	14
ENPP2	3.428	14
NOV	3.3292	14
EGFL7	3.1236	10
EPHB1	2.9201	10

Extracellular Matrix Component

Gene	Log2FC	Day
NTN4	2.5376	10
COL12A1	2.3137	14
MATN2	2.0271	14
LAMA5	1.936	14
CST3	1.7981	10

Cell Matrix Adhesion

Gene	Log2FC	Day
APOD	4.3493	14
ITGA1	2.5479	14
CD34	2.291	10
CDKN2A	2.2165	14
LAMA5	1.936	14

Cell-Cell Adhesion

Gene	Log2FC	Day
SELP	4.8073	14
CLDN5	3.9212	14
GAS6	3.7083	10
ARVCF	3.3395	10
NOV	3.3292	14

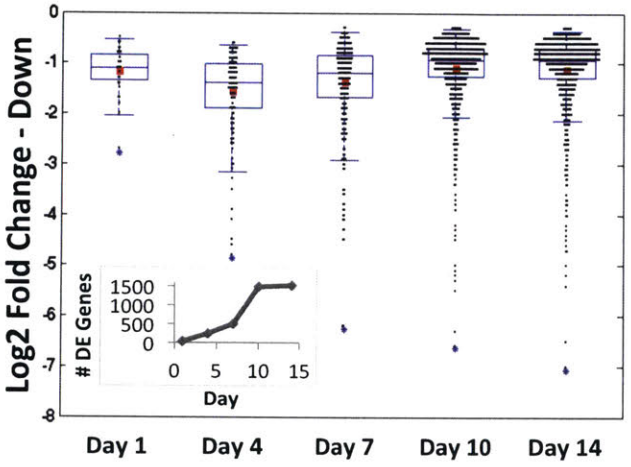

d

Vasculature Development

Gene	Log2FC	Day
HPSE	-2.8229	10
ACKR3	-2.7158	10
SLIT2	-2.6196	10
TGFBI	-2.5873	14
F3	-2.5742	10

Extracellular Matrix Component

Gene	Log2FC	Day
LAMC2	-4.1514	7
LAMB3	-2.6009	14
TGFBI	-2.5873	14
ANXA2P2	-2.5865	14
DCN	-2.561	10

Cell Matrix Adhesion

Gene	Log2FC	Day
VCAM1	-3.6317	10
CD44	-3.3057	14
HPSE	-2.8229	10
NID2	-2.5278	10
TESK2	-2.0598	14

Cell-Cell Adhesion

Gene	Log2FC	Day
VCAM1	-3.6317	10
CD44	-3.3057	14
CD74	-3.1717	14
IL7R	-2.7425	10
IL18R1	-2.6798	14

Figure 6-1 EC RNA expression. (a,c) distribution of differentially expressed genes with adjusted p-value < 0.05. Boxplots are overlayed with vertical histograms of the distributions for each day. Log_2FC values calculated with respect to mono-culture EC at day 1 for normalization. Red box in box-plot represents mean. Blue asterisk denotes maximum Log_2FC value for a given day. Inset – total number of differentially expressed genes at each day. (b,d) top 5 (Log_2FC) differentially expressed genes related to specific categories as labeled. Full gene names can be found in Appendix 3.

The top 5 DE genes related to (1) vasculature development, (2) extracellular matrix, (3) cell-matrix adhesion, and (4) cell-cell adhesion are listed in Figure 6-1 (b and d) for both up and down regulation. While these lists are not exhaustive, they represent the leading drivers of many of the morphological and functional observations presented in earlier chapters, and serve as a basis for hypothesis generation and future mechanistic studies.

To validate this analysis, we look at the most highly differentially expressed genes related to the ECM. These include: netrin 4 – a laminin related protein involved in angiogenesis and mural cell adhesion to endothelial cells; collagen 12 – a structural ECM protein; matrilin 2 – a protein containing the von Willebrand factor domain and involved in matrix assembly; and laminin. All of these proteins were either directly identified, or directly related to proteins identified in our mass spectrometry experiments. This provides confidence that the DE genes identified in our sequencing analysis correlate with actual protein expression.

As an alternative to focusing on individual DE genes, we performed hierarchical clustering to identify groups of genes with similar temporal expression patterns and further identified the shared functional characteristics of the genes in those groups (Figure 6-2). Of note, genes related to inflammation and wound healing - and corresponding signaling pathways (TNF-mediated and NIK/NF-κB) - were increasingly down regulated throughout the 10-day transition period identified above. It is likely that part of the stabilizing effect FBs have on ECs is to dampen the inflammatory response and induce a more stable phenotype, especially at the later stages of vascular morphogenesis. In-line with our observations, the most highly up-regulated genes were related to the developmental process and regeneration. Interestingly, positive regulation of cell communication – including the gene for PDGFB – was highly up-regulated. This growth factor is important for the attraction of stabilizing mural cells to the vascular wall (see Chapter 1) and likely contributes to the physical contact interactions between ECs and FBs we observed in our system. Finally, we note that genes related to the apoptotic process were highly up-regulated at later stages for ECs. This too is in-line with our experimental observations. Whereas co-culture with FB significantly enhanced EC viability when compared to mono-culture conditions, EC viability decreased for extended culture periods in our fluidic system. At 3 weeks, the vasculature remained viable and functional, but increased cell death was noticeable. In future studies we will explore additional factors, such as continuous physiological shear flow, to further increase the stability of our system.

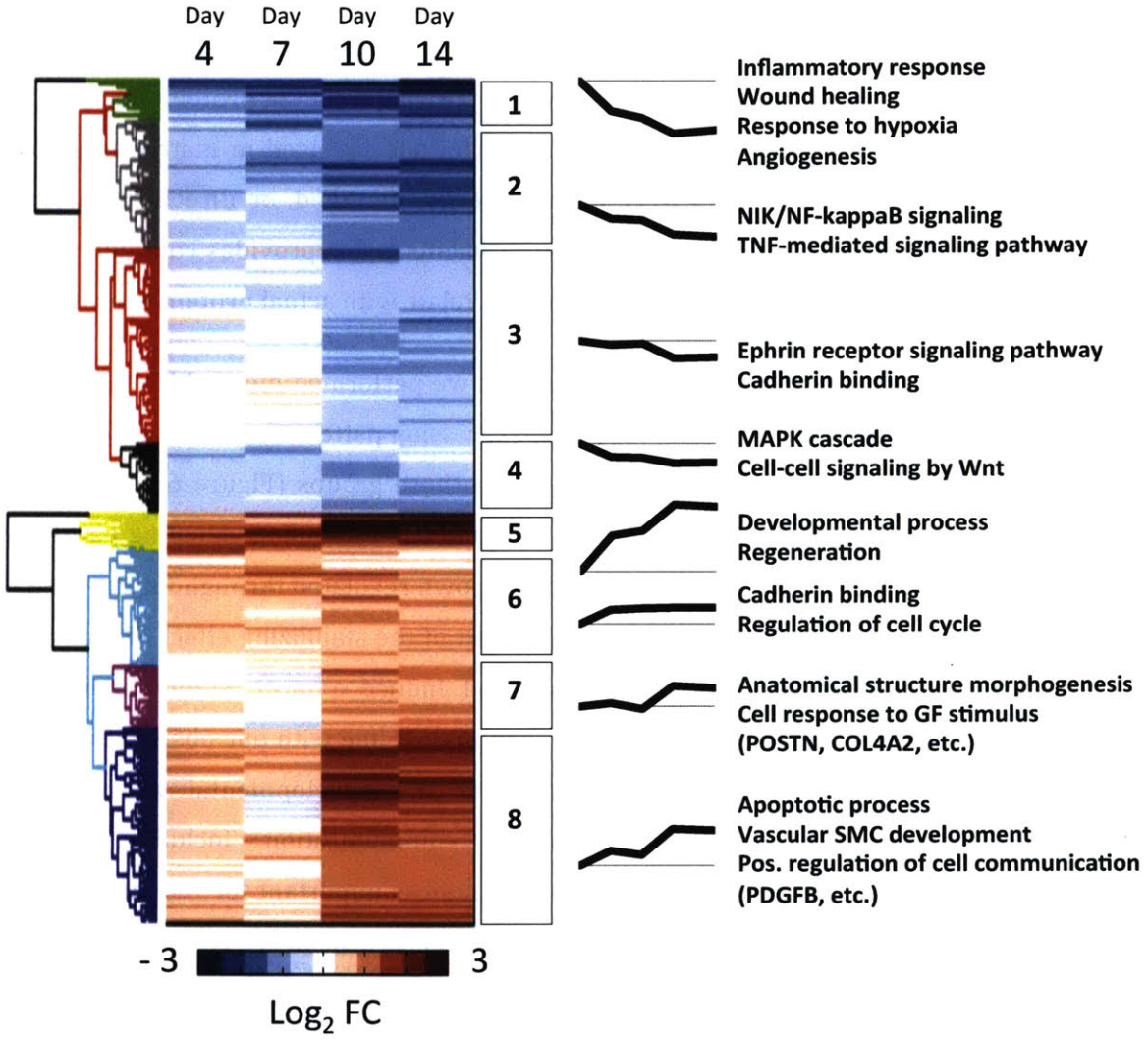

Figure 6-2 EC hierarchical clustering. Log_2FC values calculated with respect to day 1 for normalization. Line plots represent group averages of Log_2FC values with respect to time.

Principal component analysis (PCA) is a method used to identify and visualize patterns in data sets with large numbers of variables and is thus helpful for genome-wide expression studies[196]. Using PCA (Figure 6-3), we again observed a sharp phenotypic transition between day 7 and day 10, represented by the large separation along the PC1 axis. Genes contributing to the positive PC1 axis are related to down-regulation of the inflammatory response. This is in agreement with our findings from clustering analysis. Interestingly, mono-culture ECs occupy the most extreme position along the positive PC2 axis – composed

of genes relating to up-regulation of the inflammatory response. This further strengthens the implication that the EC phenotypic state associated with initial 3D hydrogel encapsulation is un-stable, and that interactions with stabilizing support cells are necessary for vascular morphogenesis to progress.

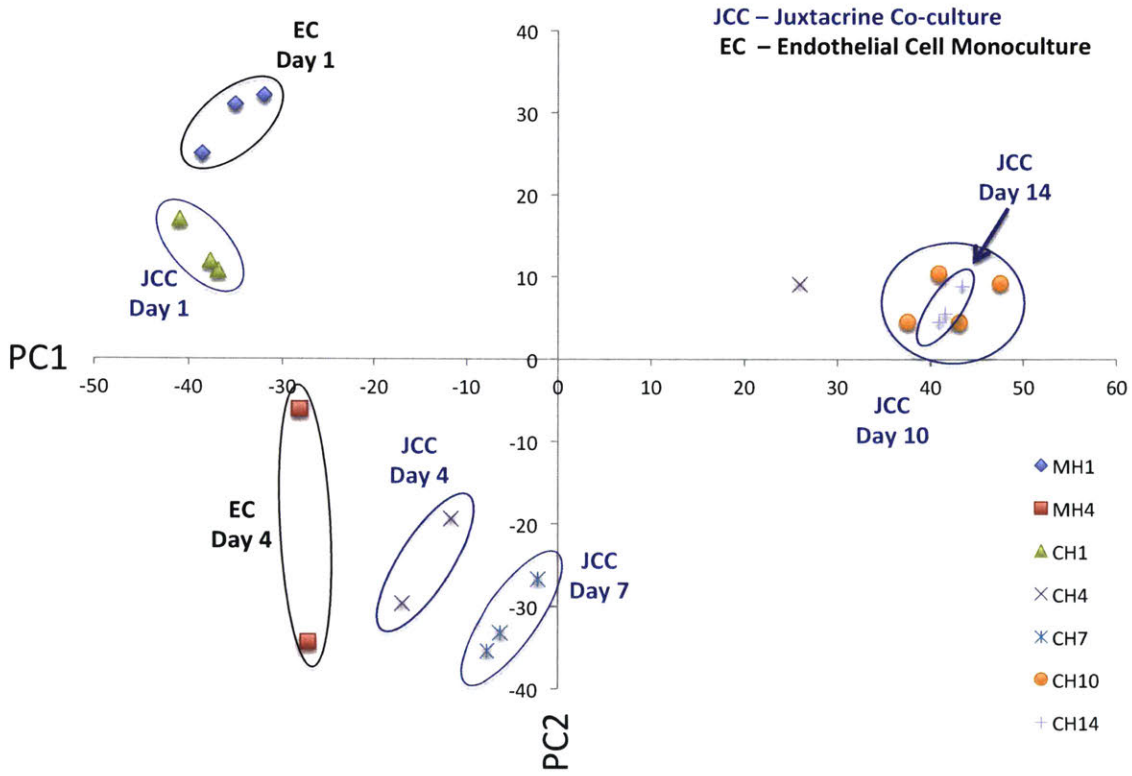

Figure 6-3 EC Principle Component Analysis (PCA). JCC condition is EC isolated from co-culture with FB. EC condition is EC cultured alone. Positive PC1 axis composed of genes related to down-regulation of inflammatory response. Positive PC2 axis composed of genes relating to up-regulation of inflammatory response.

6.2.2 Fibroblast RNA Expression

The maximum number of DE genes for FB occurs on day 10, with 1016 up-regulated and 1059 down-regulated genes (inset of Figure 6-4 a and c).

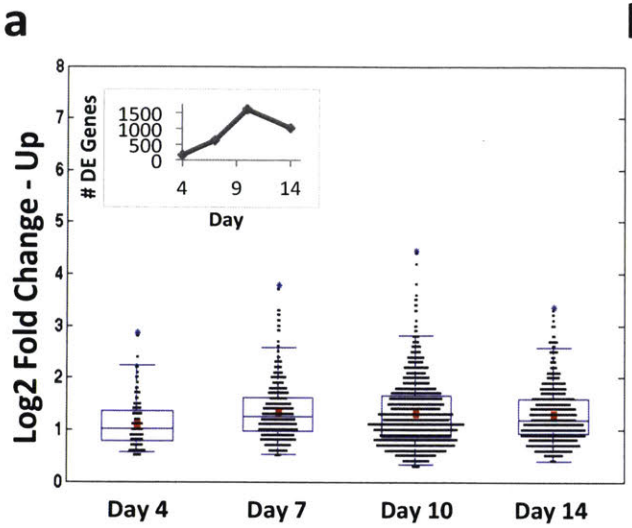

b

Vasculature Development

Gene	Log2FC	Day
NOTCH3	3.0751	10
TYMP	2.9434	10
E2F7	2.9392	7
APOE	2.7801	14
ADM2	2.7558	10

Extracellular Matrix Component

Gene	Log2FC	Day
FBN2	2.545	10
LOXL1	2.2506	10
SMOC1	2.1918	10
LAMB3	1.9307	10
COL5A3	1.8947	14

Cell Matrix Adhesion

Gene	Log2FC	Day
CDKN2A	2.3523	10
ITGA3	2.0432	10
DAPK3	1.9931	10
COL5A3	1.8947	14
ITGA1	1.7763	14

Cell-Cell Adhesion

Gene	Log2FC	Day
TNFSF4	3.4996	10
NOTCH3	3.0751	10
CSTA	2.9782	10
PCDH7	2.8745	10
CLDN11	2.8528	4

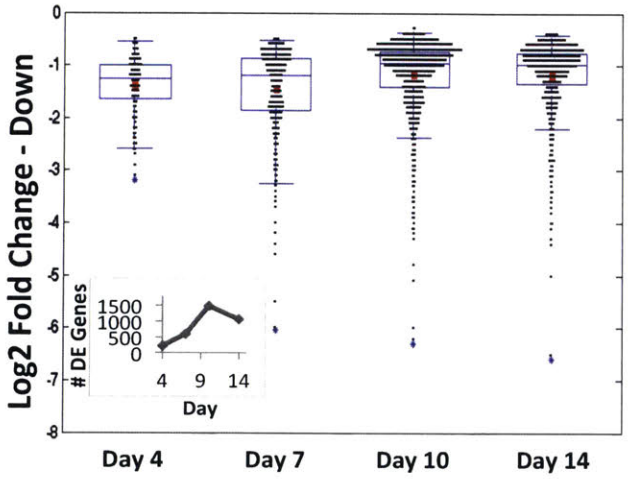

d

Vasculature Development

Gene	Log2FC	Day
SCG2	-4.3776	10
FGF10	-3.963	10
THBS1	-3.8872	10
CCL2	-3.7032	10
DCN	-3.0343	14

Extracellular Matrix Component

Gene	Log2FC	Day
DCN	-3.0343	14
ELN	-2.8994	14
MFAP4	-2.8427	7
MATN2	-2.7919	14
ANG	-2.7678	7

Cell Matrix Adhesion

Gene	Log2FC	Day
THBS1	-3.8872	10
CCR7	-2.3957	10
SNED1	-1.9151	7
CTGF	-1.8882	4
GREM1	-1.7347	4

Cell-Cell Adhesion

Gene	Log2FC	Day
SERPINE2	-4.2949	7
CCL2	-3.7032	10
CXCL12	-2.9382	10
DPP4	-2.9047	10
WNT5A	-2.7442	4

Figure 6-4 FB RNA expression. (a,c) distribution of differentially expressed genes with adjusted p-value < 0.05. Boxplots are overlayed with vertical histograms of the distributions for each day. Log_2FC values calculated with respect to day 1 for normalization. Red box in box-plot represents mean. Blue asterisk denotes maximum Log_2FC value for a given day. Inset – total number of differentially expressed genes at each day. (b,d) top 5 (Log_2FC) differentially expressed genes related to specific categories as labeled. Full gene names can be found in Appendix 3.

Hierarchical clustering analysis reveals that for FB as well, the most significantly down-regulated genes were related to inflammation and wound healing (Figure 6-5). As expected for fibroblasts, genes in the most highly up-regulated cluster were related to ECM organization. Interestingly, an additional up-regulated cluster is associated with focal adhesions and the positive regulation of cytoskeleton organization – likely related to the active force generation we measured with AFM and TFM (Chapter 4).

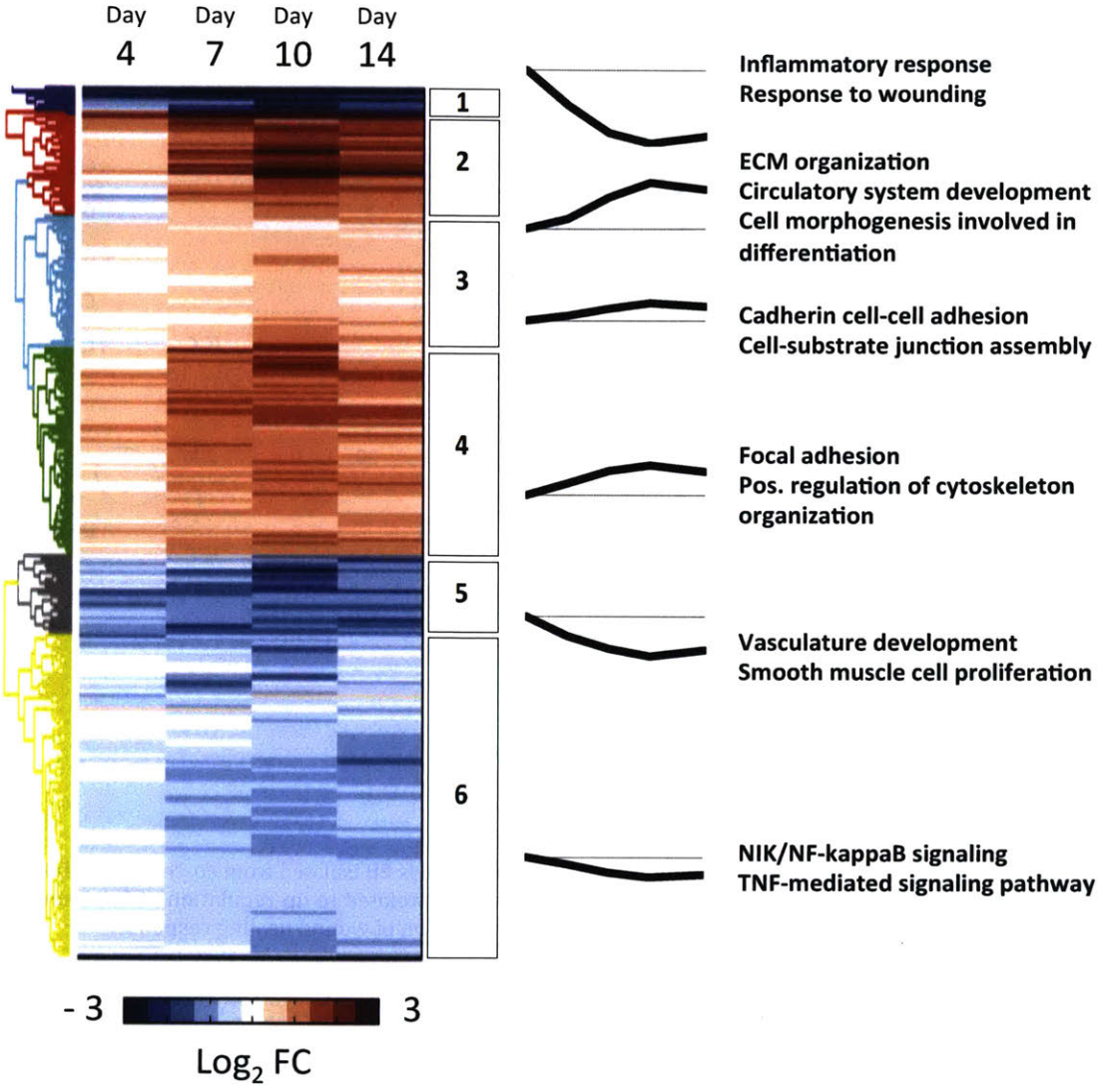

Figure 6-5 FB hierarchical clustering. Log_2FC values calculated with respect to day 1 for normalization. Line plots represent group averages of Log_2FC values with respect to time.

The PCA plot (Figure 6-6) distinctly shows that the major phenotypic transition for FB occurs between days 4 and 7. The separation occurs along the positive PC1 axis, which is driven by the up-regulation of genes related to ECM and focal adhesion. Interestingly as well, the mono-culture FB conditions are separated from co-culture conditions along the positive PC2 axis. As with EC mono-culture, this separation is associated with up-regulation of the wound healing response.

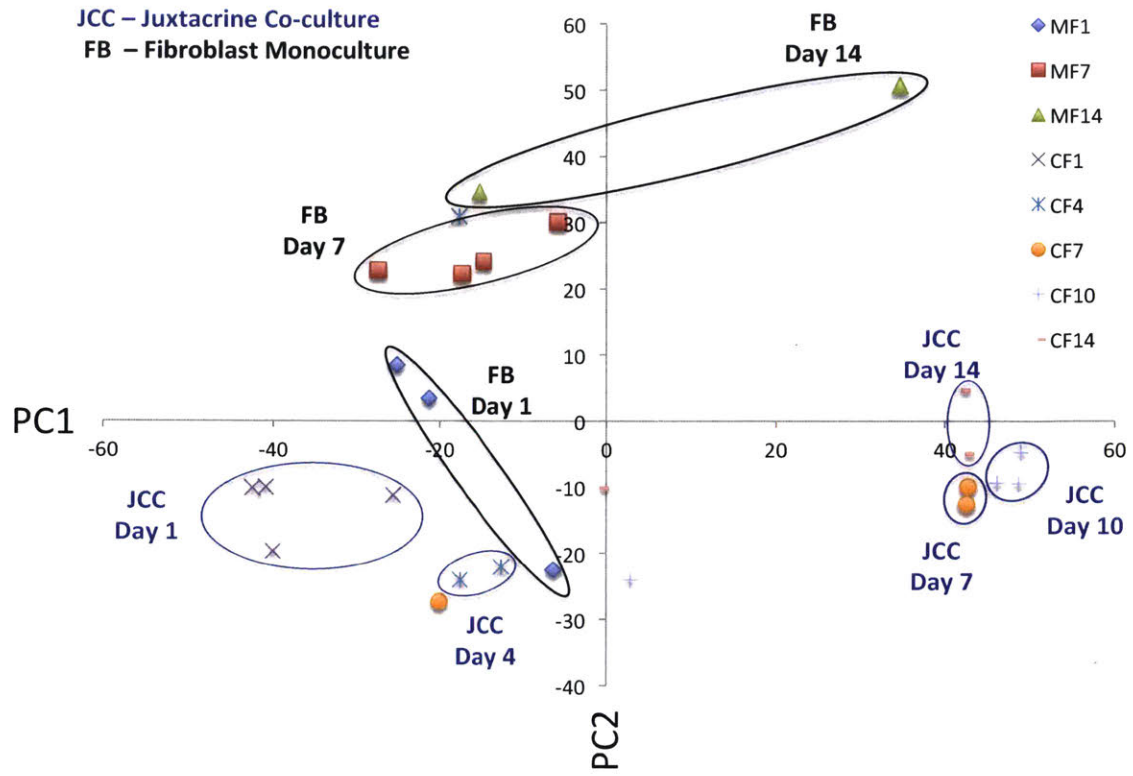

Figure 6-6 FB Principle Component Analysis (PCA). JCC condition is FB isolated from co-culture with EC. FB condition is FB cultured alone. Positive PC1 axis composed of genes related to up-regulation of ECM and focal adhesion. Positive PC2 axis composed of genes relating to up-regulation of wound healing response.

Finally, we investigated the phenotypic source for the close juxtacrine morphological interactions observed between FBs and ECs. We first confirmed the high expression of alpha smooth muscle actin (Figure 6-7a), a gene associated with the contractile phenotype and consistent with the elongated shape assumed by the FBs. Looking more broadly at the genes associated with vascular related contractile cells – myofibroblasts, pericytes, and vascular smooth muscle cells – we found that the expression profile of FBs in our system most closely resembled that of vascular smooth muscle cells (VSMC). These cells surround, support, and stabilize arterioles with diameters of roughly 30 microns and above - dimensions consistent with the vessels in our system.

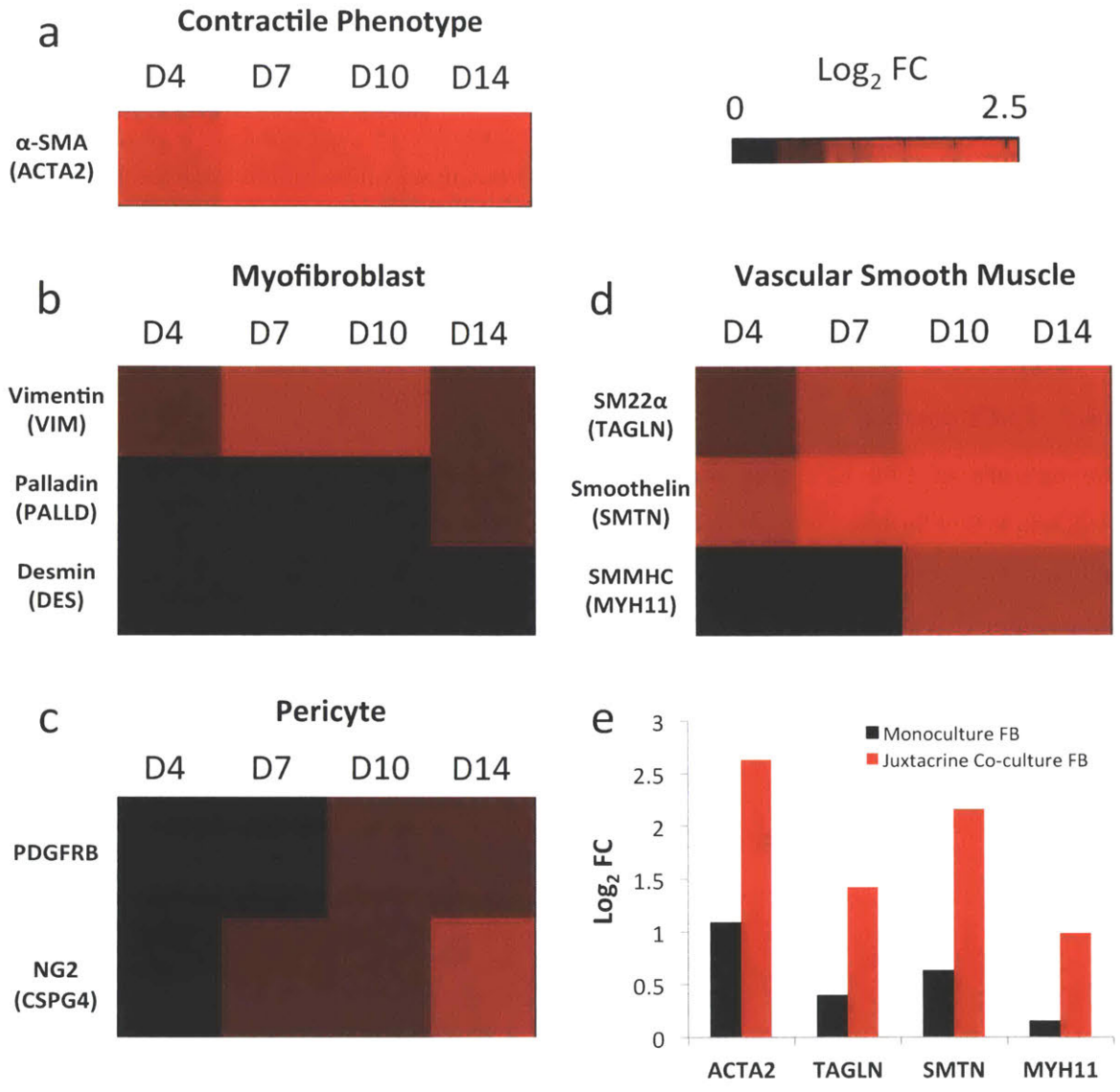

Figure 6-7 FB phenotype identification. (a) expression of alpha smooth muscle actin gene. (b-d) expression of genes associated with contractile sub-phenotypes. (e) comparison of vascular smooth muscle cell gene expression between co-culture and mono-culture FB. Log_2FC values calculated with respect to day 1 for normalization.

Interestingly, we compared the expression levels of VSMC specific markers between juxtacrine co-culture and mono-culture FBs, and found they were significantly higher in the case of co-culture with ECs (Figure 6-7e). Thus, ECs interacted with FBs to promote a FB phenotype that in-turn enhanced EC stabilization.

6.3 Methods

6.3.1 Tissue Dissociation

To isolate cells for RNA-sequencing, the extracted tissue was dissociated with 2.5% trypsin (Gibco) for 1 hr in an incubator with occasional mixing. The trypsin was then diluted 50X, and the cells were passed through a 35 micron strainer in preparation for FACS sorting (See Appendix 2 for a detailed protocol).

6.3.2 FACS Sorting

The mixture of GFP ECs and non-fluorescent FBs were then separated using the BD FACSAria II Cell Sorter. Independent populations of un-mixed cells were used as controls to calibrate the sorting parameters (figure 6-8). After sorting, the ECs and FBs were independently pelleted, re-suspended in 1 ml Trizol, and stored at -80° C, so that further processing of all experimental conditions and replicates could be performed simultaneously.

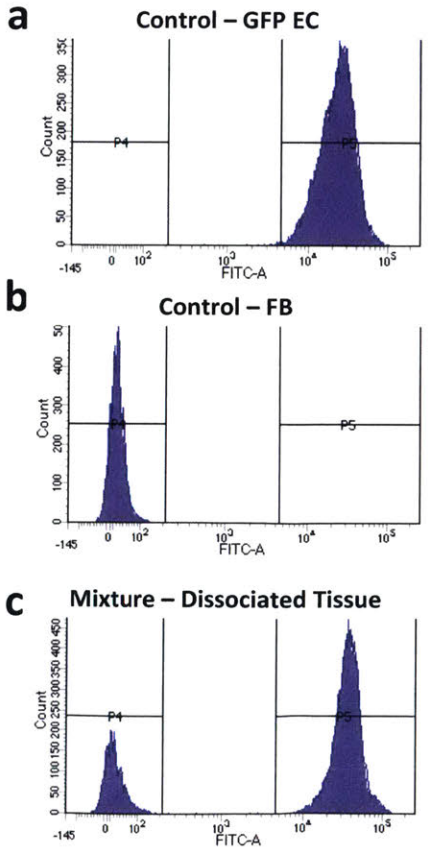

Figure 6-8 FACS sorting representative data. (a) positive control (GFP HUVEC). (b) negative control (non-fluorescent FB). (c) sorting into two populations for RNA sequencing.

6.3.3 RNA Isolation

RNA was isolated with TRIzol (Invitrogen), by following the manufacturers instructions for RNA isolation. See TRIzol Reagent User Guide at company website: (https://tools.thermofisher.com/content/sfs/manuals/trizol_reagent.pdf).

6.3.4 Sequencing

3' digital gene expression libraries (3'DGE) were prepared based on a protocol derived from Soumillon et al.[197]

6.3.5 Data Analysis

Post-sequencing, quality-control on each of the libraries was be performed to assess coverage depth, enrichment for messenger RNA (exon/intron and exon/intergenic density ratios), fraction of rRNA reads and number of detected genes using bespoke scripts. Sequences were aligned against the human genome hg19 using bwa [https://www.ncbi.nlm.nih.gov/pubmed/19451168]. Gene expression was estimated based on reads mapping near the 3' end of transcripts using ESAT [https://www.ncbi.nlm.nih.gov/pubmed/27470110], based on the Refseq annotation. Results were summarized as counts per million mapped reads (CPMs), merged across samples, log-transformed and subjected to hierarchical clustering and visualization. Differential expression analysis was performed in the R v. 3.2.3 statistical environment using the DESeq2 package[198]. Sequencing library size factors and gene-specific count dispersion parameters were estimated for each library.

Differences in gene expression between conditions (expressed as log2-transformed fold-changes in expression levels) were estimated under a general linear model (GLM) framework fitted on the read counts, modeled under a negative binomial distribution. Differential expression significance was assessed using a Wald test on the fitted count data (all these steps were performed using the DESeq() function in DESeq2)[198]. Independent

filtering based on the mean of normalized count of the differentially-expressed genes was turned off as well as Cook's distance-based filtering which assess how much the fit of the distribution would be impacted by removing an individual sample[198,199]. P-values were adjusted for multiple-comparison testing using the Benjamini-Hochberg procedure[200].

Hierarchical clustering was performed with the Matlab (Mathworks) "clustergram" function, using 'Dendrogram' value of 5, and 'Linkage' mode 'complete'.

Principal components were extracted from log-regularized count data using DESeq2.

7 Preliminary Developments and Future Work

7.1 Introduction

One of the most significant advantages of this fluidic based platform is the ability to apply and maintain physiological flows through the engineered vasculature. Coupled with the ability to quantitatively assess vascular form and function in real-time, it promises to be a useful tool for disease modeling and drug screening as a more efficient and cost-effective alternative or supplement to animal studies. By tailoring the model to the physiology of an individual patient, we can further enhance its clinical usefulness. This chapter presents preliminary findings and proposes future directions for the continued development of this platform into a physiological, continuous flow assay for patient specific, organ specific disease modeling and drug screening.

7.2 Flow

We performed preliminary flow studies in which we applied a constant pressure head of 2 cm H_2O across the tissue for 7 days after the vasculature was completely formed, from day 7 to day 14. We quantified the 3D morphological and functional properties for the flow condition and the static control condition at day 14, and compared these to the values previously reported for day 7.

Both the vascular density and volume fraction decreased for the tissues exposed to flow by day 14 (35.5 $\pm$ 8.28 vs 45.6 $\pm$ 4.87 lumens per mm^2, and 8.1 $\pm$ 0.48 vs 13.6 $\pm$ 3.32 %, respectively; Figure 7-1a-b). The static control also exhibited decreased vascular density compared to day 7 (39.6 $\pm$ 6.96 lumens per mm$^{2)}$ – but to a lesser degree – and was statistically unchanged with regard to volume fraction (14.4 $\pm$ 1.92 %). This suggests that some pruning of vessels occurred during the second week of culture, and this effect was enhanced by the presence of flow.

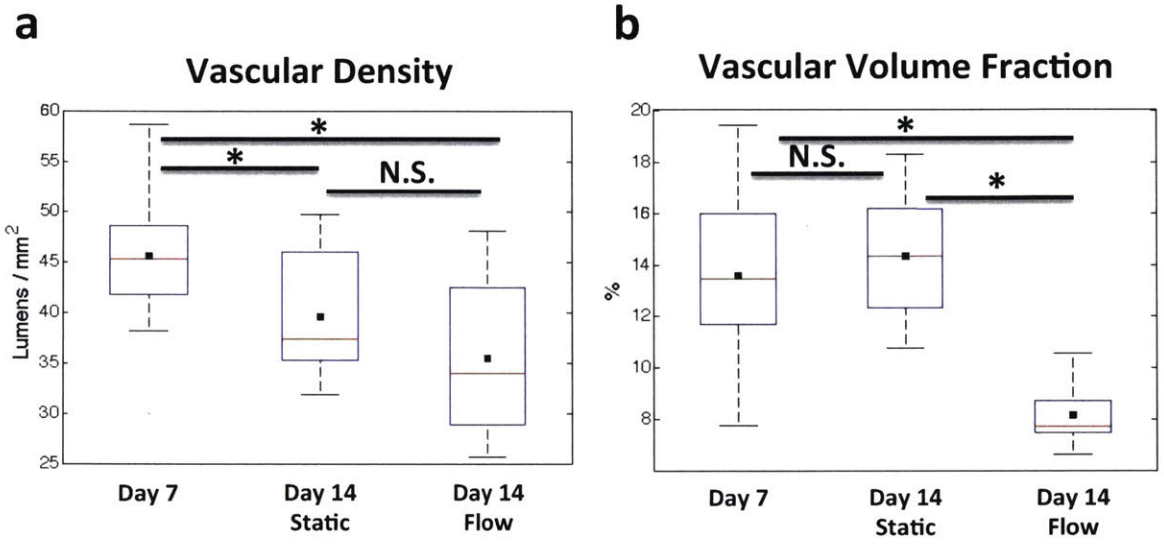

Figure 7-1 Tissue scale vascular morphology measurements - Flow. Constant flow through vasculature initiated at day 7 and maintained for additional 7 days. Static devices were cultured for entire 2 weeks without flow. (a) vascular density, (b) vascular volume fraction. Black square represents mean value. * signifies p-value < 0.01 for 2-tailed t-test.

At the scale of individual vessels, we found that the average vessel diameter decreased for both the static (30.1 microns) and flow (28.8 microns) conditions at day 14, compared to day 7 (33.2 microns) (Figure 7-2a). There was no significant change in average vessel length (Figure 7-2b).

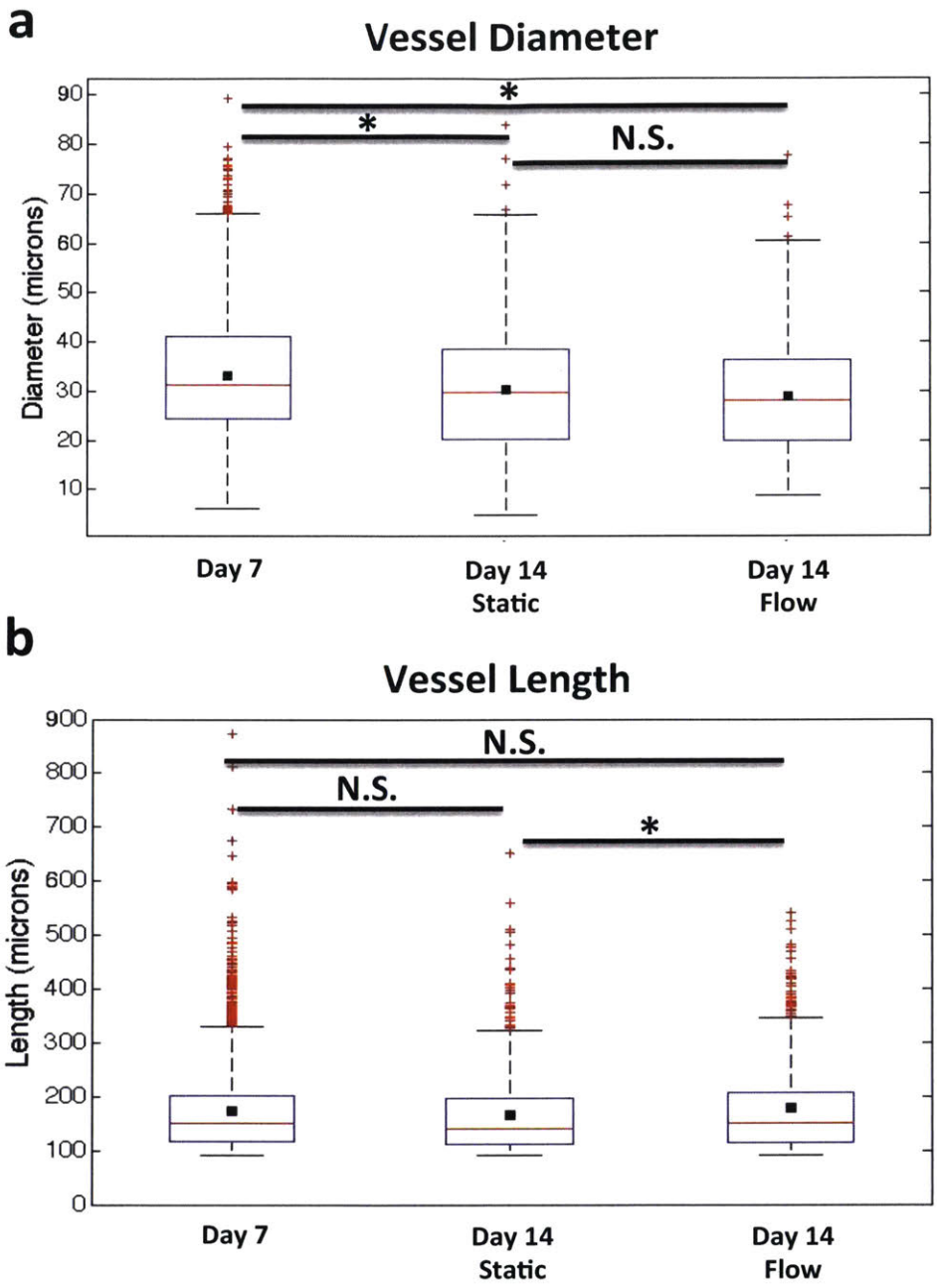

Figure 7-2 Single vessel morphology measurements - Flow. Constant flow through vasculature initiated at day 7 and maintained for additional 7 days. Static devices were cultured for entire 2 weeks without flow. (a) vessel diameter, (b) vessel length. Black square represents mean value. * signifies p-value < 0.01 for 2-tailed t-test.

We also quantified the effects of flow on vascular function and found that the permeability at day 14 was higher for the vasculature exposed to flow, as compared to the static condition (4.81e-7 $\pm$ 1.34e-7 cm/s vs. 1.84e-7 $\pm$ 0.78e-7; Figure 7-3).

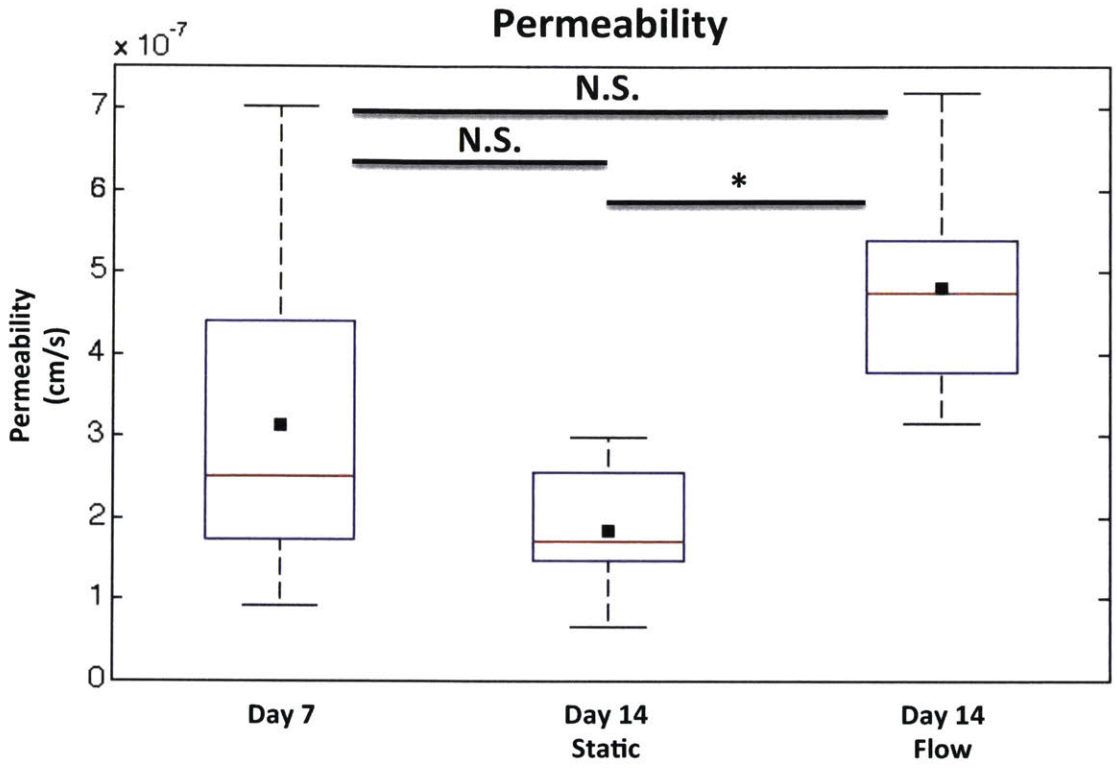

Figure 7-3 Permeability measurements – Flow. Constant flow through vasculature initiated at day 7 and maintained for additional 7 days. Static devices were cultured for entire 2 weeks without flow. Black square represents mean value. * signifies p-value < 0.01 for 2-tailed t-test.

This result is counter-intuitive, since the effects of chronic shear have been shown to induce vascular stability and would seemingly lead to a decrease in permeability[201]. To address this, we note that the vascular response to flow is not binary, but is dependent on the magnitude of flow rates, velocities, and shear stresses. A thorough examination of the effects of flow should include a range of applied flow rates and would likely expose regimes with different morphological and functional responses. Future improvements to the flow apparatus to increase the - now limited - throughput (2 flow devices vs. 12 static devices per experiment) are necessary to increase our ability to perform these experiments and collect results with significant confidence. In any event, these results demonstrate that flow can affect the morphological and functional behavior of the vasculature in our system, and may need to be incorporated in future studies if the model is to accurately represent the *in vivo* conditions for applications such as disease modeling and drug screening.

7.3 Stem Cell Derived Vasculature

To enhance the clinical usefulness of our platform, we validated our ability to generate functional vasculature from patient derived cells. We replaced HUVECs with Human Induced Pluripotent Stem-Cell Derived ECs (HIPSC-ECs), and successfully formed perfusable vasculature with similar morphological characteristics (Figure 7-4).

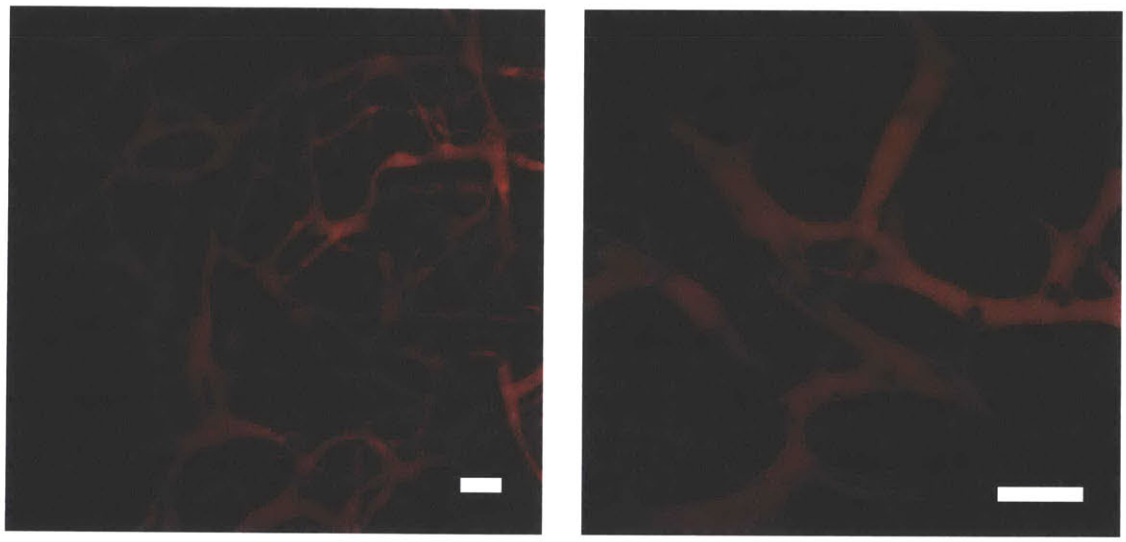

Figure 7-4 Human induced pluripotent stem cell EC (HIPSC-EC) microvasculature. Microvasculature formed in fluidic device with HIPSC-EC. Non-fluorescent ECs perfused with red 70 kDa dextran for visualization. Scale = 100 μm.

In future studies, it will be useful to (1) generate and compare engineered vasculature from HIPSC-ECs derived from different donors, (2) use HIPSC-ECs from diseased patients to model specific pathologies, (3) include stromal and parenchymal cells derived from HIPSCs from the same donor.

7.4 Vascularized Organ Model

We developed and validated a modular technique to vascularize an engineered tissue containing organ specific cell clusters. To demonstrate the concept, we first incorporated inorganic, PEG, beads into the hydrogel along with the ECs and FBs (Figure 7-5a). Perfusable vasculature successfully formed around the beads, un-inhibited by their presence (Figure 7-5b). The vessels were localized to the interstitial regions between the beads, and thus bead density was found to affect the overall vascular morphology. Confocal

image slices of the tissue resemble histological samples in which interstitial microvessels are interspersed among the parenchymal tissue (Figure 7-5c). Every bead was located within 200 microns of the nearest microvessel – a typical physiological characteristic necessary to sustain tissue survival and function.

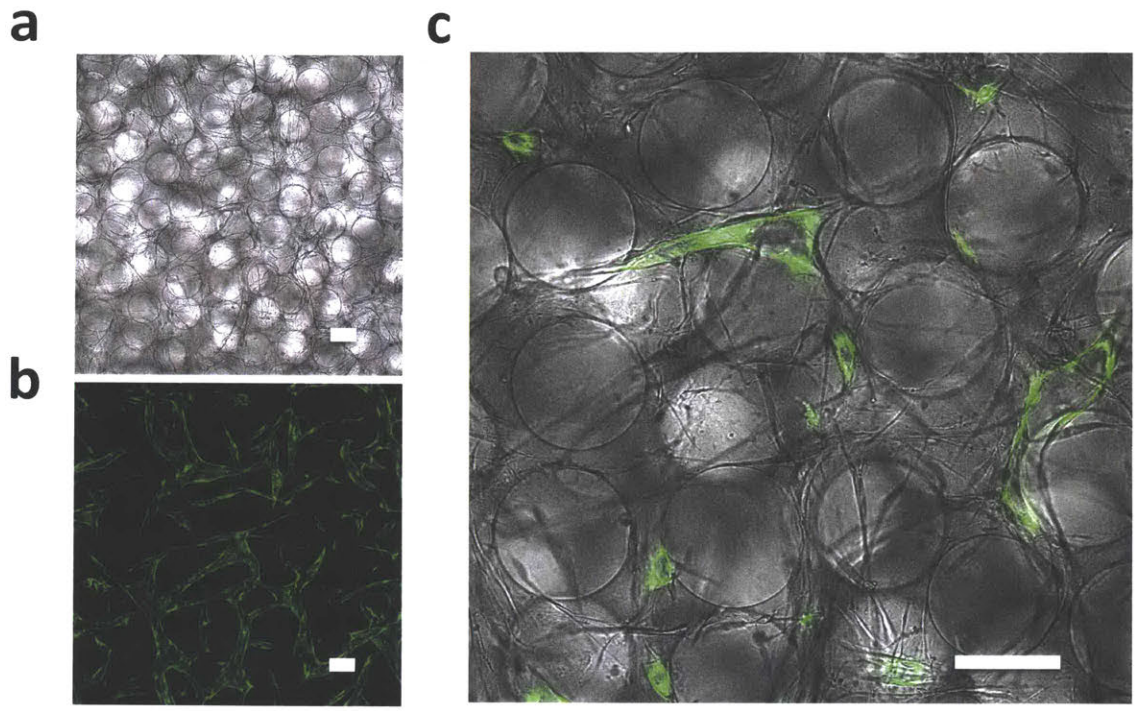

Figure 7-5 Vascularized tissue with encapsulated synthetic hydrogel beads. (a) 100 micron PEG beads encapsulated in fibrin gel. (b) perfusable vasculature forms around PEG beads. (c) single slice showing open vascular lumens in interstitial space between PEG beads. Scale = 100 μm.

By encapsulating parenchymal cells inside the beads, we could – in the future – incorporate clusters of any organ specific cell-type, or combinations of cell-types within a fully vascularized tissue construct. In this way, we have de-coupled the process of engineering vascularized organ constructs into the independent processes of (1) vascularizing a hydrogel, and (2) encapsulating cells in biocompatible hydrogel beads. The former step was validated in this thesis, and the encapsulation of numerous cell types in organic and inorganic beads has been demonstrated elsewhere[202,203]. With this method, we can also modulate the types of parenchymal cells and their densities.

As an alternative to encapsulating the parenchymal cells in beads, we tested our ability to directly culture parenchymal cell clusters in the same hydrogel as the vascular cells. We

cultured pancreatic islets with diameters ranging from 100 – 200 microns together with ECs and FBs and successfully formed perfusable vasculature around the islets (Figure 7-6).

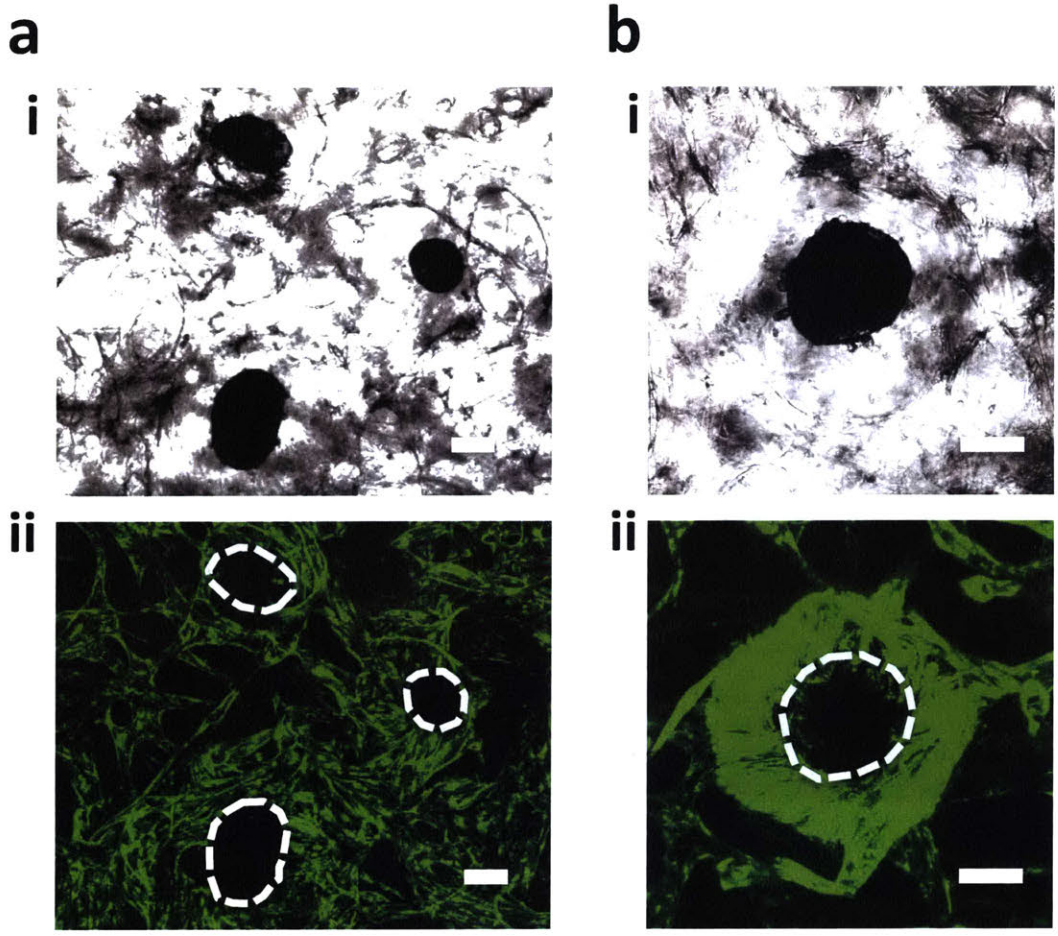

Figure 7-6 Vascularized tissue with encapsulated pancreatic islets. (ai) transmitted light image of pancreatic islets encapsulated in vascularized fibrin gel. Islets appear black. (aii) GFP (HUVEC) channel of same image as (ai) showing vasculature surrounding islets. Islets identified by white dash outlines. (b) magnified image of single islet from (a). Scale = 100 μm.

This technique can potentially be used to vascularize other tissue constructs containing large cell clusters such as tumors or organoids of various origin within a perfusable fluidic device. It is important to note that the vasculature, in our system, did not penetrate the islets as it does in physiological pancreatic tissue. A key focus of future research will be to identify the necessary conditions to achieve that result. It may be useful to initially incorporate ECs in the islets and allow them to self organize from within.

7.5 Metabolomics Analysis

We collected the supernatant from the fluidic devices and successfully analyzed the metabolites generated by the vascularized tissue using mass spectrometry. We found positive and negative changes in 16 metabolites with a range of 1 to 6 orders of magnitude (Table 7-1 and Table 7-2). The ability to identify and quantify metabolic products in our system will enable us to perform quantitative drug testing experiments, in which we apply known drugs and characterize how they are metabolized by the organ of interest.

Table 7-1 Upregulated metabolites. Mass spectrometry analysis of metabolites in supernatant collected from fluidic devices after 7 days of vascularization. Fold change with respect to day 1 values.

Fold Change	p-value (corrected)	Formula	Compound name
2660562.5	1.87E-09	C13 H18 O4	Penicillin O
2344003.8	1.91E-09	C11 H14 O4	Sinapyl alcohol
2209544.2	7.66E-10	C12 H26 O3	8,8-Dimethoxy-2,6-dimethyl-2-octanol
1741256.2	1.49E-09	C8 H19 N	Octylamine
863983.4	1.91E-09	C9 H13 N O3	L-Adrenaline
831403.75	5.34E-12	C7 H11 N3 O2	N(pi)-Methyl-L-histidine
2.00862	2.57E-04	C6 H13 N O2	L-Leucine

Table 7-2 Downregulated metabolites. Mass spectrometry analysis of metabolites in supernatant collected from fluidic devices after 7 days of vascularization. Fold change with respect to day 1 values.

Fold Change	p-value (corrected)	Formula	Compound name
-1793102.90	3.64E-13	C10 H18 O5	2-hydroxy-decanedioic acid
-1292231.90	7.16E-10	C11 H20 N2 O3	L-isoleucyl-L-proline
-1130116.40	2.35E-11	C12 H23 N O4	Isovalerylcarnitine
-1105739.50	4.80E-12	C11 H15 N5 O4	1-Methyladenosine
-1086210.90	8.24E-12	C9 H9 N O3	Hippuric acid
-3.72	3.67E-05	C6 H6 N2 O	Nicotinamide
-2.28	1.04E-04	C19 H14 O5 S	Phenolsulfonphthalein
-2.14	4.54E-04	C24 H30 O6	Estra-1,3,5(10)-triene-3,6alpha, 17beta-triol triacetate
-2.10	1.81E-04	C11 H9 N O2	Indoleacrylic acid

7.6 Methods

7.6.1 Flow

Constant perfusion of the vasculature was maintained for 7 days by connecting a custom-made acrylic flow apparatus to the device through insertion into the medium access ports (Figure 7-7a).

The flow apparatus comprised two independent medium reservoirs – one each for the upstream and downstream sides of the vasculature. Male leuer connectors at the bottom of the reservoirs ensured secure attachment with the device. The gel filling ports were plugged to ensure a continuous pressure gradient from upstream to downstream, and to prevent the leakage of medium. A 2-cm height difference was established between the two reservoirs to initiate flow through the vasculature (Figure 7-7c). As medium filled into the downstream reservoir, it was immediately pumped back into the upstream reservoir with a custom-made pump to maintain the constant pressure head (Figure 7-7d). Without the use

of a pump, we calculated that the initial pressure head would decay by 10% after 1 h of flow.

An acrylic lid was placed on the flow apparatus to prevent contamination of the medium. Holes drilled into the lid – one above each reservoir – provided access to syringe needles attached to the pump tubing. The insertion depth of the syringe needle in the downstream reservoir was used to adjust the overall pressure head. Note that the lid was not attached securely to the flow apparatus, such that the medium in the reservoirs was still exposed to atmospheric pressure.

By setting the pump flow rate higher than the flow rate of medium through the vasculature, we ensured that medium would not accumulate in the downstream reservoir.

Flow was initiated after 7 days of culture and continuous perfusion was maintained for an additional 7 days. The entire system – device, reservoir, and pump – was kept in an incubator, and the medium was replaced every 2 days.

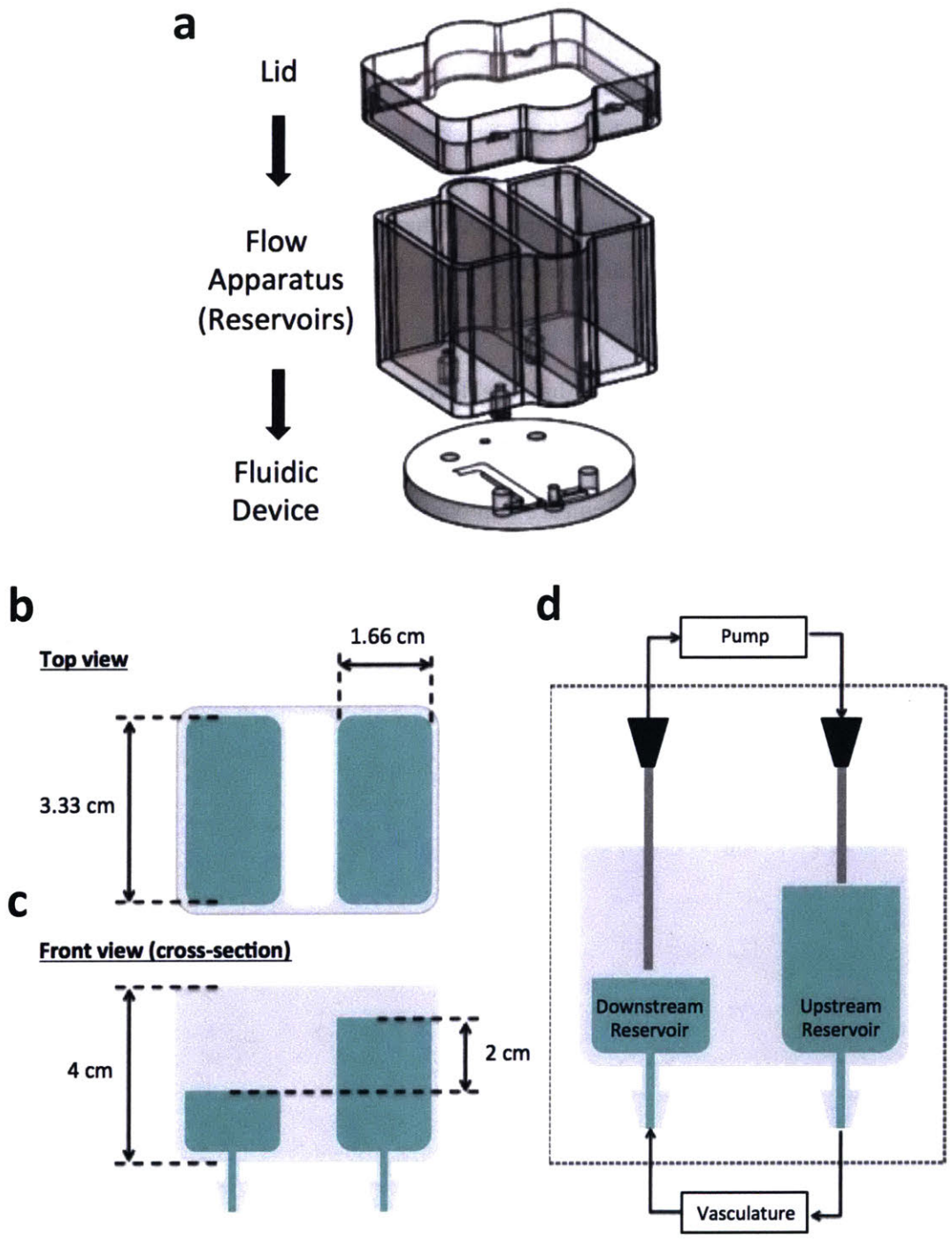

Figure 7-7 Continuous flow system. (a) custom-made acrylic flow apparatus interfaces with medium access ports in fluidic device. Apparatus contains two independent reservoirs: upstream and downstream. (c) flow is induced by pressure head due to height difference between reservoirs. (d) external pump maintains continuous flow by returning medium from downstream to upstream reservoir after if passes through vasculature.

7.6.2 IPSC-EC Vasculature

Human IPSC-ECs were purchased from Cellular Dynamics (CDI) and cultured in Maintenance Medium as per the manufacturer's instructions. Briefly, the Maintenance Medium consists of Vasculife VEGF Medium (Lifeline Cell Technology) without FBS and supplemented with EC Medium Supplement from CDI. All other culture techniques used were the same as for HUVEC.

Experimental procedures for forming vascular networks with IPSC-ECs in fluidic devices were the same as for HUVEC. Notably, during cell encapsulation in fibrin gel (see Section 2.3.5), IPSC-ECs were re-suspended in EGM-2MV rather than Maintenance Medium, because Maintenance Medium was found to interfere with fibrin gel polymerization. After polymerization, Maintenance Medium was again used for the remainder of the experiments.

7.6.3 Seeding PEG Beads in Fluidic Device

PEG beads were fabricated using a custom PDMS-based microfluidic flow channel system. Briefly, a precursor solution of 8-arm PEG norbornene (MW 20 kDa, JenKem) was flowed through the main channel and a perpendicular stream of mineral oil was used to cut the PEG solution into spherical droplets with 100 micron diameter. The droplets were photo-polymerized by irradiation with UV light at an average intensity of 30 mW/cm^2 for 2 minutes. The beads were washed to remove the mineral oil. For fibrin gel encapsulation, the beads were resuspended in EGM-2MV with 4 U/ml thrombin and added to the cell suspension. The initial cell and bead suspension densities were adjusted to ensure the desired final encapsulation densities (4 M/ml EC; 2 M/ml FB). The fibrinogen suspension was maintained at 6 mg/ml and mixed 1:1 with the cell and bead suspension. This standard protocol was used whenever additional elements were encapsulated in the hydrogel (i.e. beads, islets, additional cell types, etc.). We tested two different bead densities: (1) 400k /ml, corresponding to a 1:10 ratio with ECs, and (2) 40k /ml, corresponding to a 1:100 ratio with ECs.

7.6.4 Seeding Islets in Fluidic Device

Rat islets were purchased from Joslin Diabetes Center where they were isolated using a well established perfusion protocol. Subsequently, they were cultured in suspension in RPMI 1640 growth medium supplemented with 10% FCS and 1% Pen-Strep. Islets were

encapsulated together with ECs and FBs in a fibrin gel and seeded in the fluidic device as described above for PEG beads. Due to the relative scarcity of islets procured, we seeded roughly 10 islets per fluidic device.

7.6.5 Metabolite Analysis

200 microliters of supernatant was collected from 5 independent fluidic devices during the daily medium change, and was combined to generate a 1 ml sample for mass spectroscopy analysis of metabolites.

LC-MS analyses were performed on an Agilent 6530 Accurate-Mass LC-QTOF mass spectrometer with an Agilent Jet Stream electrospray ionization (ESI) source and a MassHunter workstation (version B.06). The mass spectrometer was interfaced with an Agilent 1290 ultra-HPLC system. The column was an Agilent Extend-C18 (2.1 × 50 mm, 1.8 μm; Agilent Technologies). The column compartment temperature was set at 40°C. The QTOF instrument was calibrated daily before runs using the standard tuning solution from Agilent Technologies. ESI mass spectra were acquired in positive ion mode for total and free DCF measurements. Mass data were collected between a mass-to-charge ratio (m/z) of 70 and 1000 at either two scans per second or four scans per second. The settings were as follows: ion spray voltage, 3800 V; heated capillary temperature, 350°C; drying gas, 8 l/min; nebulizer, 30 psi; sheath gas temperature, 380°C; and sheath gas flow, 12 l/min. Two reference masses (m/z 121.0509, $C_5H_4N_4$; and m/z 922.0098, $C_{18}H_{18}O_6N_3P_3F_{24}$) were infused continuously to allow constant mass correction during the run. Variation of retention times and m/z values was ≤0.2 minutes and <5 ppm mass error, respectively, and the relative standard deviations of peak areas were <20%. Mobile phases consisted of double-distilled water containing 0.1% FA (A) and ACN containing 0.1% FA (B). Linear gradients were from 2% to 95% B over 12 minutes at a flow rate of 0.4 ml/min.

Mass Profile Professional and Meltin software were used to identify the small molecules.

Appendix 1 – Gene Names

	Gene Name		Gene Name
FBN2	fibrillin 2(FBN2)	NID2	nidogen 2(NID2)
TNFSF4	tumor necrosis factor superfamily member 4(TNFSF4)	LAMA5	laminin subunit alpha 5(LAMA5)
VCAM1	vascular cell adhesion molecule 1(VCAM1)	IL7R	interleukin 7 receptor(IL7R)
SMOC1	SPARC related modular calcium binding 1(SMOC1)	NTN4	netrin 4(NTN4)
CTGF	connective tissue growth factor(CTGF)	ARVCF	armadillo repeat gene deleted in velocardiofacial syndrome(ARVCF)
ANG	angiogenin(ANG)	E2F7	E2F transcription factor 7(E2F7)
DCN	decorin(DCN)	APOE	apolipoprotein E(APOE)
IL18R1	interleukin 18 receptor 1(IL18R1)	CXCL12	C-X-C motif chemokine ligand 12(CXCL12)
GAS6	growth arrest specific 6(GAS6)	COL12A1	collagen type XII alpha 1 chain(COL12A1)
SLIT2	slit guidance ligand 2(SLIT2)	APOD	apolipoprotein D(APOD)
TGFBI	transforming growth factor beta induced(TGFBI)	CDKN2A	cyclin dependent kinase inhibitor 2A(CDKN2A)
CLDN11	claudin 11(CLDN11)	FGF10	fibroblast growth factor 10(FGF10)
CD34	CD34 molecule(CD34)	LOXL1	lysyl oxidase like 1(LOXL1)
EPHB1	EPH receptor B1(EPHB1)	ADM2	adrenomedullin 2(ADM2)
CCR7	C-C motif chemokine receptor 7(CCR7)	CLDN5	claudin 5(CLDN5)
MATN2	matrilin 2(MATN2)	ENPP2	ectonucleotide pyrophosphatase/phosphodiesterase 2(ENPP2)
CSTA	cystatin A(CSTA)	WNT5A	Wnt family member 5A(WNT5A)
HPSE	heparanase(HPSE)	SCG2	secretogranin II(SCG2)
TYMP	thymidine phosphorylase(TYMP)	TESK2	testis-specific kinase 2(TESK2)
SNED1	sushi, nidogen and EGF like domains 1(SNED1)	GREM1	gremlin 1, DAN family BMP antagonist(GREM1)
THBS1	thrombospondin 1(THBS1)	CST3	cystatin C(CST3)
COL5A3	collagen type V alpha 3 chain(COL5A3)	NOV	nephroblastoma overexpressed(NOV)
SELP	selectin P(SELP)	PCDH7	protocadherin 7(PCDH7)
LAMB3	laminin subunit beta 3(LAMB3)	ACKR3	atypical chemokine receptor 3(ACKR3)
ITGA1	integrin subunit alpha 1(ITGA1)	DPP4	dipeptidyl peptidase 4(DPP4)
ANXA2P2	annexin A2 pseudogene 2(ANXA2P2)	CCL2	C-C motif chemokine ligand 2(CCL2)
ITGA3	integrin subunit alpha 3(ITGA3)	SERPINE2	serpin family E member 2(SERPINE2)
LAMC2	laminin subunit gamma 2(LAMC2)	CD74	CD74 molecule(CD74)
EGFL7	EGF like domain multiple 7(EGFL7)	CD44	CD44 molecule (Indian blood group)(CD44)
ELN	elastin(ELN)	NOTCH3	notch 3(NOTCH3)
DAPK3	death associated protein kinase 3(DAPK3)	F3	coagulation factor III, tissue factor(F3)
MFAP4	microfibrillar associated protein 4(MFAP4)		

Appendix 2 – Protocols

Cell Encapsulation in Fluidic Device

Reagents from Sigma:

Fibrinogen

F8630-1G

Thrombin

T4648-1KU

Preparation:

Dissolve thrombin and freeze at 100 U/ml

Dissolve fibrinogen in PBS to 6 mg/ml

- Allow to dissolve for several hours (~2-4) in the water bath, agitating occasionally by hand
- Syringe filter the solution (0.22 micron)
- This solution can be kept at 4 degrees, but should be used within 1 week (or until it becomes cloudy)

Procedure:

1. Prepare 50 ul aliquots (1 per device to be filled) from 6 mg/ml fibrinogen stock solution in 500 ul eppindorf tubes and **keep over ice**.
2. Dilute thrombin stock solution in cell medium: 40 ul thrombin solution in 1 ml medium (4 U/ml)
3. Prepare ECs and resuspend in the thrombin solution above at 16 million cells per ml: **keep over ice.**
4. Prepare FBs and resuspend in the thrombin solution above at 8 million cells per ml: **keep over ice.**
5. Combine equal amounts of EC and FB suspensions
6. Add 50 ul from thrombin/cell suspension into one eppindorf tube containing fibrinogen solution prepared above. Mix gently by pipette aspiration 8-10 times **over ice. (Make sure to uniformly mix cell suspension again before filling each device.)**
7. Pipette 100 ul cell/gel suspension and fill device half from top, half from bottom **(when filling bottom continue filling as much as possible before gel bursts into media channel – gel should start to bulge out)**
8. Place in humidity box for 25-30 minutes and leave at room temperature
9. Remove from humidity box and fill device with fresh warm medium

Tissue Dissociation for RNA-seq

Materials:

- PBS (7ml)
- Trypsin 2.5% (2ml)
- EGM-2MV (20ml)
- Eppindorf w/0.2ml media (x2)
- Blue cap FACS tube
- scalpel
- 12-well plate

1. Image devices
2. Rinse 2X with PBS
3. Cut PDMS with scalpel along medium channels and remove section
4. Add 1 ml warm Trypsin 2.5% into 12 well-plate well
5. Scrape gel with scalpel into well
6. Mix thoroughly with pipette
7. Incubate for 20 minutes
8. Mix thoroughly with pipette
9. Incubate for 10 minutes (30 min total)
10. Mix thoroughly with pipette to break up tissue
11. Add 1 ml warm Trypsin 2.5%
12. Incubate for 15 minutes (45 min total)
13. Mix thoroughly with pipette
14. Incubate for 15 minutes (60 min total)
15. Mix thoroughly with pipette
16. Incubate for 10 minutes (70 min total)
17. Mix thoroughly with pipette
18. Add 5 ml fresh media to 15 ml Falcon tube and coat sides
19. Transfer cells to falcon tube
20. Collect remaining cells with 1 ml fresh media (X3)
21. Spin down – 8 min; 200g
22. Aspirate to 1ml – mix
23. Top off tube to 10 ml with fresh medium
24. Spin down – 8 min; 300g
25. Aspirate down to 0.5 ml - mix
26. Filter through blue cap into FACS tube
27. Collect remaing cells with 0.2 ml and pass through filter
28. FACS sort into 1.5 ml Eppindorf tube with 0.2 ml EGM-2MV

Freeze

1. Top off tubes to 1.5ml with PBS
2. Place each tube into 50 ml falcon

3. Spin down @300 rcf for 10 minutes
4. Aspirate to 0.1 ml
5. Add 0.9 ml Trizol, mix
6. Label and store at -80 C

Tissue Preparation for Mass Spectrometry

1. Rinse 2X with PBS
2. Image Devices
3. Aspirate all PBS in channels
4. Cut out gels
5. If available, mechanically homogenize tissue
6. Soak in 5ml of 0.5% Triton X100/11 mM ammonium hydroxide (Decellurization buffer) for 30 min on shaker at 4C
    a. 11 mM ammonium hydroxide: 7.59 µl in 10 ml
7. Replace with fresh Decellurization buffer and shake for additional 30 min at 4C
8. Replace with PBS and shake for 10 min at 4C
9. Transfer gels to low retention eppindorf tube [cryo-vial if freezing] and parafilm, add 1.5 ml PBS, incubate on a wheel for 10 min at 4C
10. Spin down at 16,000G for 5 min, remove supernatant, re-suspend with large orifice tip
11. Repeat steps 8-9
12. Repeat washing step 8 with water instead of PBS
13. Spin down, aspirate
14. (OPTIONAL) Flash freeze

Adapted from Naba et. al., JOVE protocol

15. Prepare 100 mM Ammonium bicarbonate (NH_4HCO_3) in HPLC-grade water
    a. Add 79 mg to 10 ml
16. Prepare 8 M urea in 100 mM NH_4HCO_3
    a. Weigh 4.8048 g and add 100 mM NH_4HCO_3 to 10 ml
17. Prepare 500 mM DTT in HPLC-grade H20
    a. Add 100 ul to one tube
18. Resuspend pellet with 50 ul 8M urea
19. Add 1 ul 500 mM DTT
20. **Incubate for 2 hr at 1400 rpm/37 C (make sure tube is sealed)**
21. Prepare 500 mM iodoacetamide in HPLC-H20
    a. Add 600 ul to vial and mix thouroughly
22. Cool sample to RT
23. Add 2.5 ul 500 mM iodoacetamide
24. **Incubate in dark at RT for 30 min**
25. Prepare 100 mM NH_4HCO_3 pH 8.0
    a. Add HCL to 100 mM NH_4HCO_3 as needed
26. Add 150 ul NH_4HCO_3 pH 8.0
27. Add 2 ul PNGaseF
28. **Incubate for 2 hr at 1400 rpm/37 C**
29. Prepare 0.5 ug/ul LysC in HPLC-H20
    a. Add 40 ul HPLC-H20 to one vial
30. Add 2 ul LysC

31. **Incubate for 2 hr at 1400 rpm/37 C**
32. Prepare 0.5 ug/ml trypsin
    a. Add 40 ul Resuspension buffer to one vial
    b. Heat at 30C for 15 min
33. Add 6 ul 0.5 ug/ml trypsin
34. **Incubate O/N at 1400 rpm/37 C**
35. Add 3 ul 0.5 ug/ml trypsin
36. **Incubate for 2 hr at 1400 rpm/37 C**
37. Prepare 50% trifluoro-acetic acid (TFA) in HPLC-H20
    a. Pipette 250 ul HPLC-H20 into glass vial
    b. Add 250 ul TFA
38. Add 1 ul and test on pH strip
39. Repeat until pH < 2.0
40. Centrifuge at 16,000G for 5 min at RT
41. Collect supernatant in clean low-retention tube
42. Store at -20C

Appendix 3 – Imagej Macro Scripts

2D – Network Length – Epifluorescent Microcope Images

```
//Input is an epi-fluorescent 2D image

//User is prompted to open folder containing multiple images for processing

dir = getDirectory("Choose a Directory ");

list = getFileList(dir);

networkLength = newArray();

//For each image:

for (j=0; j<list.length; j++) {

        path = dir+list[j];

        open(path);

//Perform image processing

        run("Subtract Background...", "rolling=50");

        run("Enhance Contrast...", "saturated=1");

        run("Unsharp Mask...", "radius=100 mask=0.60");

        setOption("BlackBackground", false);

//Binarize

        run("Make Binary");

        run("Dilate");

        run("Dilate");

        run("Dilate");

        run("Dilate");

        run("Dilate");

//Skeletonize

        run("Skeletonize (2D/3D)");
```

```
//Analyze Skeleton
        run("Analyze Skeleton (2D/3D)", "prune=none prune");
        run("Close All");
        a = newArray();
//Calculate longest connected network
        for (i=0; i<nResults; i++) {
                b = getResult("# Branches",i)*getResult("Average Branch Length",i);
                a = Array.concat(a,b);
        }
        Array.getStatistics(a, min, max, mean, std);
        networkLength = Array.concat(networkLength,max);
  close("Results");
  print(networkLength[j]);
}
```

//Network length is the longest connected network for each image; if no units were //stored in the original image properties, values will be reported in pixels.

2D – Network Length – Confocal Microscope Images

//Input is a a .tif confocal image stack with 2 channels: (1) HUVEC, (2) Dextran; Note: //only the HUVEC channel is needed for this algorithm.

//User is prompted to open folder containing multiple .tif image stacks for processing

```
dir = getDirectory("Choose a Directory ");
list = getFileList(dir);
networkLength = newArray();
```

//For each image stack:

```
for (j=0; j<list.length; j++) {
        path = dir+list[j];
```

```
        open(path);
        run("Split Channels");
//Process HUVEC channel, slice by slice
        selectWindow("C1-" + list[j]);
        rename("HUVEC");
//Standard thresholding algorithm:
                for (i=0; i<nSlices; i++) {
                run("8-bit");
                run("Subtract Background...", "rolling=1000 sliding slice");
                run("Enhance Contrast", "saturated=5");
                for(k=0; k<10; k++) run("Despeckle", "slice");
                run("Gaussian Blur...", "sigma=3.0 slice");
                setAutoThreshold("Triangle");
                setAutoThreshold("Triangle dark");
                getThreshold(lower, upper );
                setThreshold(lower, upper );
                run("Convert to Mask", "only");
                run("Next Slice [>]");
                }
//2D projection
        run("Z Project...", "projection=[Max Intensity]");
//Skeletonize
        run("Skeletonize (2D/3D)");
//Analyze skeleton
        run("Analyze Skeleton (2D/3D)", "prune=none prune");
        run("Close All");
```

```
        a = newArray();
//Calculate longest connected network
        for (i=0; i<nResults; i++) {
                b = getResult("# Branches",i)*getResult("Average Branch Length",i);
                a = Array.concat(a,b);
        }
        Array.getStatistics(a, min, max, mean, std);
        networkLength = Array.concat(networkLength,max);
  close("Results");
  print(networkLength[j]);
}
```

2D Perfusability

```
//Input is a .tif confocal image stack with 2 channels: (1) HUVEC, (2) Dextran
//User is prompted to open folder containing multiple .tif image stacks for processing
dir = getDirectory("Choose a Directory ");
list = getFileList(dir);
//For each image stack:
for (j=0; j<list.length; j++) {
if (endsWith(list[j],"tif")) {
        path = dir+list[j];
        open(path);
        run("Split Channels");
        selectWindow("C1-" + list[j]);
        rename("HUVEC");
        selectWindow("C2-" + list[j]);
```

```
        rename("Dextran");
//Process HUVEC channel
        selectWindow("HUVEC");
//2D Projection
        run("Z Project...", "projection=[Max Intensity]");
        run("8-bit");
        run("Subtract Background...", "rolling=1000 sliding slice");
        run("Enhance Contrast", "saturated=10");
        for(k=0; k<5; k++) run("Despeckle", "slice");
        run("Gaussian Blur...", "sigma=3.0 slice");
//Binarize
        setAutoThreshold("Triangle");
        setAutoThreshold("Triangle dark");
        getThreshold(lower, upper );
        setThreshold(lower, upper );
        run("Convert to Mask", "only");

        rename("vessels.tif");
//Define Interstitial Region
        run("Duplicate...", "duplicate");
        rename("interstitial.tif");
        run("Invert");
        run("Create Selection");
        roiManager("add");
//Define Vessel Region
        selectWindow("vessels.tif");
```

```
        run("Create Selection");
        roiManager("add");
//Process Dextran Channel
        selectWindow("Dextran");
//2D Projection
        run("Z Project...", "projection=[Average Intensity]");
//Measure average dextran intensity in interstitial region, and use to threshold image
        roiManager("measure");
        int_ave = getResult("Mean", 0);
        setAutoThreshold("Default dark");
        setThreshold(int_ave, 4095);
        setOption("BlackBackground", false);
        run("Convert to Mask");
//Measure average intensity of binarized dextran image within Vessel Region
//Note: for fully perfused vasculature, average binary intensity in vascular region
//would be 255; for fully non-perfused vasculature, average binary intensity in
 //vascular region would be 0

        roiManager("measure");
        Perfusability = getResult("Mean", 3)/255;
        run("Close All");
        roiManager("delete");
        selectWindow("Results");
        run("Close");
        print(Perfusability);
        }
```

```
}
//Perfusability is reported as a number between 0 and 1
```

3D Perfusability

```
Perfusability_Array = newArray();
//Input is a .tif confocal image stack with 2 channels: (1) HUVEC, (2) Dextran
//User is prompted to open folder containing multiple .tif image stacks for processing
dir = getDirectory("Choose a Directory ");
list = getFileList(dir);
for (j=0; j<list.length; j++) {
        if (endsWith(list[j],"tif")) {
                path = dir+list[j];
                open(path);
                run("Split Channels");
                selectWindow("C1-" + list[j]);
                rename("HUVEC");

                selectWindow("C2-" + list[j]);
                rename("Dextran");
//Process dextran channel, slice by slice
                for (i=0; i<nSlices; i++) {
                run("8-bit");
                run("Subtract Background...", "rolling=1000 sliding slice");
                run("Enhance Contrast", "saturated=5");
                for(k=0; k<10; k++) run("Despeckle", "slice");
                run("Gaussian Blur...", "sigma=3.0 slice");
```

```
//Threshold and Binarize
                setAutoThreshold("Triangle");
                setAutoThreshold("Triangle dark");
                getThreshold(lower, upper );
                setThreshold(lower, upper );
                run("Convert to Mask", "only");
                run("Next Slice [>]");
                }
//Reslice in XZ-plane
                run("Reslice [/]...", "output=1.000 start=Bottom avoid");
                rename("Dextran_Reslice");
//Process HUVEC channel, slice by slice
                selectWindow("HUVEC");
                for (i=0; i<nSlices; i++) {
                run("8-bit");
                run("Subtract Background...", "rolling=1000 sliding slice");
                run("Enhance Contrast", "saturated=5");
                for(k=0; k<10; k++) run("Despeckle", "slice");
                run("Gaussian Blur...", "sigma=3.0 slice");
//Threshold and binarize
                setAutoThreshold("Triangle");
                setAutoThreshold("Triangle dark");
                getThreshold(lower, upper );
                setThreshold(lower, upper );
                run("Convert to Mask", "only");
                run("Next Slice [>]");
```

```
                }
//Reslice in XZ-plane
                run("Reslice [/]...", "output=1.000 start=Bottom avoid");
                run("Invert", "stack");
                rename("HUVEC_Reslice");
                run("Set Measurements...", "area mean");
                setSlice(1);
//Identify vessel outlines from HUVEC channel
                run("Analyze Particles...", "  show=Outlines include add stack");
//Measure binarized dextran pixel intensity within vessel outlines
                selectWindow("Dextran_Reslice");
                roiManager("measure");
Total_Area = 0;
Zero_Area = 0;
for (l=0; l<nResults; l++) {
b = getResult("Area", l);
Total_Area = Total_Area + b;
a = getResult("Mean", l);
//If no dextran from thresholded image is found within vessel region, that region is
//considered non-perfusable
        if (a == 0) {
        Zero_Area = Zero_Area + b;
  }
}
Perfusability = (Total_Area - Zero_Area) / Total_Area;
Perfusability_Array = Array.concat(Perfusability_Array, Perfusability);
```

```
run("Close All");
selectWindow("Results");
run("Close");
roiManager("delete");
}
}
Array.show("Perfusability",Perfusability_Array)
//Perfusability is reported as a fraction of perfused volume divided by total vascular //volume
```

Barrier Function

```
//Input is a .tif confocal image stack with 2 channels: (1) HUVEC, (2) Dextran
//User is prompted to open folder containing multiple .tif image stacks for processing
dir = getDirectory("Choose a Directory ");
list = getFileList(dir);
//For each image stack:
for (j=0; j<list.length; j++) {

        if (endsWith(list[j],"tif")) {
                path = dir+list[j];
                open(path);
                run("Split Channels");
                selectWindow("C1-" + list[j]);
                rename("HUVEC");
                selectWindow("C2-" + list[j]);
                rename("Dextran");
//Process HUVEC channel
```

```
        selectWindow("HUVEC");
//2D projection
        run("Z Project...", "projection=[Max Intensity]");
        run("8-bit");
        run("Subtract Background...", "rolling=1000 sliding slice");
        run("Enhance Contrast", "saturated=10");
        for(k=0; k<5; k++) run("Despeckle", "slice");
        run("Gaussian Blur...", "sigma=3.0 slice");
//Threshold and binarize
        setAutoThreshold("Triangle");
        setAutoThreshold("Triangle dark");
        getThreshold(lower, upper );
        setThreshold(lower, upper );
        run("Convert to Mask", "only");
        rename("vessels.tif");
        run("Duplicate...", "duplicate");
//Define interstitial region
        rename("interstitial.tif");
        run("Invert");
        run("Create Selection");
        roiManager("add");
//Process dextran channel
        selectWindow("Dextran");
//2D projection
        run("Z Project...", "projection=[Average Intensity]");
//Measure average intensity of dextran in interstitial region
```

```
        roiManager("measure");
        run("Close All");
        roiManager("delete");
        selectWindow("Results");
        }
}
```

3D Binary Reconstruction

```
//Input is a confocal image stack of vasculature filled with fluorescently labeled tracer
//Only the tracer (dextran) channel should be used for this thresholding algorithm
//Processing is performed on each slice individually
for (i=0; i<nSlices; i++) {
        run("8-bit");
        run("Subtract Background...", "rolling=1000 sliding slice");
        run("Enhance Contrast", "saturated=5");
        for(k=0; k<10; k++) run("Despeckle", "slice");
        run("Gaussian Blur...", "sigma=3.0 slice");
        setAutoThreshold("Triangle");
        setAutoThreshold("Triangle dark");
        getThreshold(lower, upper );
        setThreshold(lower, upper );
        run("Convert to Mask", "only");
        run("Next Slice [>]");
}
```

Vascular Density and Vascular Volume Fraction

```
//Input is a .tif confocal image stack of vasculature filled with fluorescently labeled
//tracer. Only the tracer (dextran) channel should be used for this thresholding
//algorithm.
//User is prompted to open folder containing multiple .tif image stacks for processing.
dir = getDirectory("Choose a Directory ");
list = getFileList(dir);
VolFraction = newArray();
NumLumens = newArray();
for (j=0; j<list.length; j++) {
        if (endsWith(list[j],"tif")) {
        path = dir+list[j];
        open(path);
//For each image stack:
//Process, threshold, and binarize - slice by slice
for (i=0; i<nSlices; i++) {
        run("8-bit");
        run("Subtract Background...", "rolling=1000 sliding slice");
        run("Enhance Contrast", "saturated=10");
        for(k=0; k<5; k++) run("Despeckle", "slice");
        run("Gaussian Blur...", "sigma=3.0 slice");
        setAutoThreshold("Triangle");
        setAutoThreshold("Triangle dark");
        getThreshold(lower, upper );
        setThreshold(lower, upper );
        run("Convert to Mask", "only");
```

```
        run("Next Slice [>]");
}
//Identify vascular lumens for each slice in XZ-plane
//Calculate # lumens and % vascularized area for each slice
run("Reslice [/]...", "output=1.000 start=Bottom avoid");
rename("lumens.tif");
run("Invert", "stack");
run("Set Measurements...", "area");
run("Analyze Particles...", "size=50-Infinity display summarize stack");
selectWindow("Results");
run("Close");
selectWindow("Summary of lumens.tif");
IJ.renameResults("Results");
        a = newArray();
        c = newArray();
//Retrieve % vascularized area for each XZ-slice
//Retrieve # lumens for each XZ-slice
        for (i=0; i<nResults; i++) {
                b = getResult("%Area",i);
                a = Array.concat(a,b);
                d = getResult("Count",i);
                c = Array.concat(c,d);
        }
//Calculate average % vascularized area over all slices
        Array.getStatistics(a, min, max, mean, std);
        VolFraction = Array.concat(VolFraction,mean);
```

```
//Calculate average # lumens over all slices and normalize by cross-sectional area
        getDimensions(width, height, channels, slices, frames);
        getPixelSize(unit, pixelWidth, pixelHeight);
        totalarea = (width*pixelWidth*height*pixelHeight)/1000000;
        Array.getStatistics(c, minc, maxc, meanc, stdc);
        NumLumens = Array.concat(NumLumens,meanc/totalarea);
        selectWindow("Results");
        saveAs("Text", path + "Morph_Quant.txt");
        run("Close All");
        }
}
Array.show("VolFraction",VolFraction)
Array.show("NumVessels",NumLumens)
```

Permeability

```
//Input is a .tif confocal image stack of vasculature filled with fluorescently labeled
//tracer.
//Only the tracer (dextran) channel should be used for this thresholding algorithm.

//***User MUST manually enter the time intervals - in minutes - between the two
//images taken as an array (one for each ROI being processed) - "dt" ***
dt = newArray(12, 12, 12);
//Drift correction:  External drift correction should be applied so that individual stack
//slices of an ROI match-up at both time points.  If no appreciative drift occurred,
//enter the full stack range below
```

```
//Drift corrected stack sizes (z1 - z2) - t1
z1list = newArray(1, 2, 1);
z2list = newArray(50, 50, 50);
//Drift corrected stack sizes (z1 - z2) - t2
z1list_t2 = newArray(1, 1, 1);
z2list_t2 = newArray(50, 49, 50);

//User is prompted to open folder containing multiple .tif image stacks for processing
dir = getDirectory("Choose a Directory for t1 ");
list = getFileList(dir);
dir_1 = getDirectory("Choose a Directory for t2 ");
list_1 = getFileList(dir_1);
s = 0;
for (j=0; j<list.length; j++) {
        if (endsWith(list[j],"tif")) {
        path = dir+list[j];
        z1 = z1list[s];
        z2 = z2list[s];
        open(path);
        c = " range="+z1+"-"+z2;
        run("Duplicate...", "duplicate"+c);
        rename("original.tif");
        run("Duplicate...", "duplicate");

//For each image stack:
//Process, threshold, and binarize - slice by slice
```

```
for (i=0; i<nSlices; i++) {
        run("8-bit");
        run("Subtract Background...", "rolling=1000 sliding slice");
        run("Enhance Contrast", "saturated=5");
        for(k=0; k<10; k++) run("Despeckle", "slice");
        run("Gaussian Blur...", "sigma=3.0 slice");
        setAutoThreshold("Triangle");
        setAutoThreshold("Triangle dark");
        getThreshold(lower, upper );
        setThreshold(lower, upper );
        run("Convert to Mask", "only");
        run("Next Slice [>]");
}
run("Reslice [/]...", "output=1.000 start=Bottom avoid");
rename("interstitial.tif");
run("Duplicate...", "duplicate");
rename("lumens.tif");
run("Invert", "stack");

//Measure morphological properties
run("Set Measurements...", "area perimeter");
run("Analyze Particles...", "size=1-Infinity display summarize stack");
selectWindow("Summary of lumens.tif");
saveAs("Text", path + "Summary of lumens.txt");
IJ.renameResults("Results");
        aa = newArray();
```

```
	bb = newArray();
	for (i=0; i<nResults; i++) {
		b = getResult("%Area",i);
		d = getResult("Count",i);
		f = getResult("Perim.",i);
		h = getResult("Total Area",i);
		aa = Array.concat(aa,((h/(b/100))-h));
		bb = Array.concat(bb,(d*f));
	}

//Calculate Interstitial Volume / Vascular Surface Area
	Array.getStatistics(aa, minaa, maxaa, meanaa, stdaa);
	Array.getStatistics(bb, minbb, maxbb, meanbb, stdbb);
	V_S = meanaa/meanbb;
	print("V / S = " + V_S);
	selectWindow("Results");
run("Close");

//Define Vascular Region

run("Set Measurements...", "area mean");
selectWindow("lumens.tif");
setSlice(1);
for (l=0; l<nSlices; l++) {
run("Create Selection");
roiManager("add");
```

```
run("Next Slice [>]");
}
roiManager("save", path + "lumen_ROI.zip");

//Calculate initial average dextran intensity in vascular region
selectWindow("original.tif");
run("Reslice [/]...", "output=1.000 start=Bottom avoid");
rename("originalReslice.tif");
roiManager("measure");
roiManager("delete");
nn = nResults;
run("Summarize");
Perm_Lumens = getResult("Mean", nn);
print("Perm_Lumens = " + Perm_Lumens);
IJ.renameResults("Lumens");
selectWindow("Lumens");
saveAs("Text", path + "Permeability_Lumens.txt");
run("Close");

//Define interstitial region
selectWindow("interstitial.tif");
setSlice(1);
for (m=0; m<nSlices; m++) {
run("Create Selection");
roiManager("add");
run("Next Slice [>]");
```

```
}
roiManager("save", path + "interstitial_ROI.zip");

//Calculate initial average dextran intensity in interstitial region
selectWindow("originalReslice.tif");
roiManager("measure");
nn = nResults;
run("Summarize");
Perm_Interstitial = getResult("Mean", nn);
print("Perm_Interstitial = " + Perm_Interstitial);
IJ.renameResults("Interstitial");
selectWindow("Interstitial");
saveAs("Text", path + "Permeability_Interstitial.txt");
run("Close");

//Process t2 time-point
path_1 = dir_1+list_1[s];
z1 = z1list_t2[s];
z2 = z2list_t2[s];
open(path_1);
c = " range="+z1+"-"+z2;
run("Duplicate...", "duplicate"+c);
run("Reslice [/]...", "output=1.000 start=Bottom avoid");

////Calculate final average dextran intensity in interstitial region
roiManager("measure");
```

```
roiManager("delete");

nn = nResults;

run("Summarize");

Perm_Interstitial_t2 = getResult("Mean", nn);

print("Perm_Interstitial_t2 = " + Perm_Interstitial_t2);

IJ.renameResults("Interstitial_Perm_t2");

selectWindow("Interstitial_Perm_t2");

saveAs("Text", path + "Permeability_Interstitial_t2.txt");

run("Close");

run("Close All");


//Calculate permeability

permeability = (V_S*((Perm_Interstitial_t2 -
Perm_Interstitial)/(dt[s]*60))*(1/(Perm_Lumens - Perm_Interstitial)))/10000;

print("Permeability = " + permeability);

s = s + 1;

}

else {

}

run("Close All");

}

//Permeability is reported in cm/s
```

8 References

1. Whisler, J. A. Engineered, perfusable, human microvascular networks on a microfluidic chip. (2013).

2. Whisler, J. A., Chen, M. B. & Kamm, R. D. Control of Perfusable Microvascular Network Morphology Using a Multiculture Microfluidic System. *Tissue Eng. Part C Methods* **20,** 543–552 (2014).

3. Chen, M. B., Whisler, J. A., Jeon, J. S. & Kamm, R. D. Mechanisms of tumor cell extravasation in an in vitro microvascular network platform. *Integr. Biol. Quant. Biosci. from Nano to Macro* **5,** 1262–1271 (2013).

4. Chen, M. B. *et al.* On-chip human microvasculature assay for visualization and quantification of tumor cell extravasation dynamics. *Nat. Protoc.* **12,** 865–880 (2017).

5. Risau, W. & Flamme, I. Vasculogenesis. *Annu. Rev. Cell Dev. Biol.* **11,** 73–91 (1995).

6. Risau, W. Mechanisms of angiogenesis. *Nature* **386,** 671–674 (1997).

7. Jain, R. K. Molecular regulation of vessel maturation. *Nat. Med.* **9,** 685–693 (2003).

8. Folkman, J. & Haudenschild, C. Angiogenesis in vitro., *Publ. online 11 December 1980; | doi10.1038/288551a0* **288,** 551 (1980).

9. Montesano, R. & Orci, L. Tumor-promoting phorbol esters induce angiogenesis in vitro. *Cell* **42,** 469–77 (1985).

10. Davis, G. E., Stratman, A. N., Sacharidou, A. & Koh, W. in *International review of cell and molecular biology* **288,** 101–165 (2011).

11. Davis, G. E. & Camarillo, C. W. An α2β1 Integrin-Dependent Pinocytic Mechanism Involving Intracellular Vacuole Formation and Coalescence Regulates Capillary Lumen and Tube Formation in Three-Dimensional Collagen Matrix. *Exp. Cell Res.* **224,** 39–51 (1996).

12. Bayless, K. J. & Davis, G. E. The Cdc42 and Rac1 GTPases are required for capillary lumen formation in three-dimensional extracellular matrices. *J. Cell Sci.* **115,** 1123–36 (2002).

13. Bell, S. E. *et al.* Differential gene expression during capillary morphogenesis in 3D collagen matrices: regulated expression of genes involved in basement membrane matrix assembly, cell cycle progression, cellular differentiation and G-protein signaling. *J. Cell Sci.* **114,** 2755–73 (2001).

14. Vailhé, B., Vittet, D. & Feige, J.-J. In Vitro Models of Vasculogenesis and Angiogenesis. *Lab. Investig.* **81,** 439–452 (2001).

15. Shin, Y. *et al.* Microfluidic assay for simultaneous culture of multiple cell types on

surfaces or within hydrogels. *Nat. Protoc.* **7,** 1247–1259 (2012).

16. Zhang, B. *et al.* Biodegradable scaffold with built-in vasculature for organ-on-a-chip engineering and direct surgical anastomosis. *Nat. Mater.* **15,** 669–678 (2016).

17. Schimek, K. *et al.* Integrating biological vasculature into a multi-organ-chip microsystem. *Lab Chip* **13,** 3588–3598 (2013).

18. Namdee, K., Thompson, A. J., Charoenphol, P. & Eniola-Adefeso, O. Margination Propensity of Vascular-Targeted Spheres from Blood Flow in a Microfluidic Model of Human Microvessels. *Langmuir* **29,** 2530–2535 (2013).

19. Hattori, K. *et al.* Microfluidic perfusion culture chip providing different strengths of shear stress for analysis of vascular endothelial function. *J. Biosci. Bioeng.* **118,** 327–332 (2014).

20. Ye, X. *et al.* A biodegradable microvessel scaffold as a framework to enable vascular support of engineered tissues. *Biomaterials* **34,** 10007–10015 (2013).

21. Thomas, A., Daniel Ou-Yang, H., Lowe-Krentz, L., Muzykantov, V. R. & Liu, Y. Biomimetic channel modeling local vascular dynamics of pro-inflammatory endothelial changes. *Biomicrofluidics* **10,** 14101 (2016).

22. Lewis, D. M. *et al.* Endothelial progenitor cell recruitment in a microfluidic vascular model. *Biofabrication* **7,** 45010 (2015).

23. Huang, R. *et al.* Investigation of Tumor Cell Behaviors on a Vascular Microenvironment-Mimicking Microfluidic Chip. *Sci. Rep.* **5,** 17768 (2015).

24. Sato, M. *et al.* Microcirculation-on-a-Chip: A Microfluidic Platform for Assaying Blood- and Lymphatic-Vessel Permeability. *PLoS One* **10,** e0137301 (2015).

25. Zhang, B., Peticone, C., Murthy, S. K. & Radisic, M. A standalone perfusion platform for drug testing and target validation in micro-vessel networks. *Cit. Biomicrofluidics* **7,** (2013).

26. Kohn, J. C. *et al.* Cooperative effects of matrix stiffness and fluid shear stress on endothelial cell behavior. *Biophys. J.* **108,** 471–478 (2015).

27. Zervantonakis, I. K. *et al.* Three-dimensional microfluidic model for tumor cell intravasation and endothelial barrier function. *Proc. Natl. Acad. Sci. U. S. A.* **109,** 13515–20 (2012).

28. Nagao, R. J. *et al.* Decellularized Human Kidney Cortex Hydrogels Enhance Kidney Microvascular Endothelial Cell Maturation and Quiescence. *Tissue Eng. Part A* ten.tea.2016.0213 (2016). doi:10.1089/ten.tea.2016.0213

29. Mu, X., Zheng, W., Xiao, L., Zhang, W. & Jiang, X. Engineering a 3D vascular network in hydrogel for mimicking a nephron. *Lab Chip* **13,** 1612–1618 (2013).

30. Liu, J. *et al.* Open Source 3D-Printing Approach for Economic and Fast Engineering of

Perfusable Vessel-Like Channels Within Cell-Laden Hydrogels. *3D Print. Addit. Manuf.* **3,** 22–31 (2016).

31. Roberts, M. A. *et al.* Stromal Cells in Dense Collagen Promote Cardiomyocyte and Microvascular Patterning in Engineered Human Heart Tissue. *Tissue Eng. Part A* **22,** 633–644 (2016).

32. Zheng, Y. *et al.* In vitro microvessels for the study of angiogenesis and thrombosis. *Proc. Natl. Acad. Sci. U. S. A.* **109,** 9342–9347 (2012).

33. Rao, R. R. *et al.* Dual-Phase Osteogenic and Vasculogenic Engineered Tissue for Bone Formation. *Tissue Eng. Part A* **21,** 530–540 (2015).

34. Hasan, A., Paul, A., Memic, A. & Khademhosseini, A. A multilayered microfluidic blood vessel-like structure. *Biomed. Microdevices* **17,** 1–13 (2015).

35. Wong, K. H. K., Truslow, J. G., Khankhel, A. H., Chan, K. L. S. & Tien, J. Artificial lymphatic drainage systems for vascularized microfluidic scaffolds. *J. Biomed. Mater. Res. Part A* **101A,** 2181–2190 (2013).

36. Kim, J. A. *et al.* Collagen-based brain microvasculature model in vitro using three-dimensional printed template. *Biomicrofluidics* **9,** 24115 (2015).

37. Price, G. M. *et al.* Effect of mechanical factors on the function of engineered human blood microvessels in microfluidic collagen gels. *Biomaterials* **31,** 6182–6189 (2010).

38. Buchanan, C. F., Verbridge, S. S., Vlachos, P. P. & Rylander, M. N. Flow shear stress regulates endothelial barrier function and expression of angiogenic factors in a 3D microfluidic tumor vascular model. *Cell Adh. Migr.* **8,** 517–524 (2014).

39. Linville, R. M., Boland, N. F., Covarrubias, G., Price, G. M. & Tien, J. Physical and Chemical Signals That Promote Vascularization of Capillary-Scale Channels. *Cell. Mol. Bioeng.* **9,** 73–84 (2016).

40. Wong, K. H. K., Truslow, J. G. & Tien, J. The role of cyclic AMP in normalizing the function of engineered human blood microvessels in microfluidic collagen gels. *Biomaterials* **31,** 4706–4714 (2010).

41. Wang, X.-Y. *et al.* An artificial blood vessel implanted three-dimensional microsystem for modeling transvascular migration of tumor cells. *Lab Chip* **15,** 1178–1187 (2015).

42. Nishiguchi, A., Matsusaki, M. & Akashi, M. in 95–129 (Springer Japan, 2014). doi:10.1007/978-4-431-55139-3_5

43. Mannino, R. G. *et al.* 'Do-it-yourself in vitro vasculature that recapitulates in vivo geometries for investigating endothelial-blood cell interactions'. *Sci. Rep.* **5,** 12401 (2015).

44. Takei, T., Sakai, S., Ono, T., Ijima, H. & Kawakami, K. Fabrication of endothelialized tube in collagen gel as starting point for self-developing capillary-like network to construct three-dimensional organs in vitro. *Biotechnol. Bioeng.* **95,** 1–7 (2006).

45. Kolesky, D. B. *et al.* 3D Bioprinting of Vascularized, Heterogeneous Cell-Laden Tissue Constructs. *Adv. Mater.* **26,** 3124–3130 (2014).

46. Kang, T.-Y. *et al.* Construction of Large-Volume Tissue Mimics with 3D Functional Vascular Networks. *PLoS One* **11,** e0156529 (2016).

47. Miller, J. S. *et al.* Rapid casting of patterned vascular networks for perfusable engineered three-dimensional tissues. *Nat. Mater.* **11,** 768–774 (2012).

48. Kageyama, T. *et al. In Situ* Cross-Linkable Gelatin-CMC Hydrogels Designed for Rapid Engineering of Perfusable Vasculatures. *ACS Biomater. Sci. Eng.* **2,** 1059–1066 (2016).

49. Kang, Y., Mochizuki, N., Khademhosseini, A., Fukuda, J. & Yang, Y. Engineering a vascularized collagen-β-tricalcium phosphate graft using an electrochemical approach. *Acta Biomater.* **11,** 449–458 (2015).

50. Arrigoni, C. *et al.* Rational Design of Prevascularized Large 3D Tissue Constructs Using Computational Simulations and Biofabrication of Geometrically Controlled Microvessels. *Adv. Healthc. Mater.* **5,** 1617–1626 (2016).

51. Song, J. W. & Munn, L. L. Fluid forces control endothelial sprouting. *Proc. Natl. Acad. Sci. U. S. A.* **108,** 15342–15347 (2011).

52. Galie, P. A. *et al.* Fluid shear stress threshold regulates angiogenic sprouting. *Proc. Natl. Acad. Sci. U. S. A.* **111,** 7968–7973 (2014).

53. Shin, Y. *et al.* In vitro 3D collective sprouting angiogenesis under orchestrated ANG-1 and VEGF gradients. *Lab Chip* **11,** 2175–2181 (2011).

54. Song, J. W., Bazou, D. & Munn, L. L. Microfluidic model of angiogenic sprouting. *Methods Mol. Biol.* **1214,** 243–254 (2015).

55. Song, J. W., Daubriac, J., Tse, J. M., Bazou, D. & Munn, L. L. RhoA mediates flow-induced endothelial sprouting in a 3-D tissue analogue of angiogenesis. *Lab Chip* **12,** 5000–5006 (2012).

56. Lee, H., Kim, S., Chung, M., Kim, J. H. & Jeon, N. L. A bioengineered array of 3D microvessels for vascular permeability assay. *Microvasc. Res.* **91,** 90–98 (2014).

57. Kim, J. *et al.* Engineering of a Biomimetic Pericyte-Covered 3D Microvascular Network. *PLoS One* **10,** e0133880 (2015).

58. Kim, S., Lee, H., Chung, M. & Jeon, N. L. Engineering of functional, perfusable 3D microvascular networks on a chip. *Lab Chip* **13,** 1489–1500 (2013).

59. Vernon, R. B. & Sage, E. H. A novel, quantitative model for study of endothelial cell migration and sprout formation within three-dimensional collagen matrices. *Microvasc. Res.* **57,** 118–133 (1999).

60. Heiss, M. *et al.* Endothelial cell spheroids as a versatile tool to study angiogenesis in vitro. *FASEB J.* **29,** 3076–3084 (2015).

61. Chan, J. M. *et al.* Engineering of In Vitro 3D Capillary Beds by Self-Directed Angiogenic Sprouting. *PLoS One* **7,** e50582 (2012).

62. Mason, B. N., Starchenko, A., Williams, R. M., Bonassar, L. J. & Reinhart-King, C. A. Tuning three-dimensional collagen matrix stiffness independently of collagen concentration modulates endothelial cell behavior. *Acta Biomater.* **9,** 4635–4644 (2013).

63. Nakatsu, M. N. *et al.* Angiogenic sprouting and capillary lumen formation modeled by human umbilical vein endothelial cells (HUVEC) in fibrin gels: the role of fibroblasts and Angiopoietin-1. *Microvasc. Res.* **66,** 102–112 (2003).

64. Ceccarelli, J., Cheng, A. & Putnam, A. J. Mechanical Strain Controls Endothelial Patterning During Angiogenic Sprouting. *Cell. Mol. Bioeng.* **5,** 463–473 (2012).

65. Bongio, M., Lopa, S., Gilardi, M., Bersini, S. & Moretti, M. A 3D vascularized bone remodeling model combining osteoblasts and osteoclasts in a CaP nanoparticle-enriched matrix. *Nanomedicine* **11,** 1073–1091 (2016).

66. Hsu, Y.-H., Moya, M. L., Hughes, C. C. W., George, S. C. & Lee, A. P. A microfluidic platform for generating large-scale nearly identical human microphysiological vascularized tissue arrays. *Lab Chip* **13,** 2990–2998 (2013).

67. Jeon, J. S. *et al.* Generation of 3D functional microvascular networks with human mesenchymal stem cells in microfluidic systems. *Integr. Biol.* **6,** 555–563 (2014).

68. Belair, D. G. *et al.* Human vascular tissue models formed from human induced pluripotent stem cell derived endothelial cells. *Stem Cell Rev.* **11,** 511–525 (2015).

69. Moya, M. L., Hsu, Y.-H., Lee, A. P., Hughes, C. C. W. & George, S. C. In Vitro Perfused Human Capillary Networks. *Tissue Eng. Part C Methods* **19,** 730–737 (2013).

70. Rosenfeld, D. *et al.* Morphogenesis of 3D vascular networks is regulated by tensile forces. *Proc. Natl. Acad. Sci.* **113,** 3215–3220 (2016).

71. Bichsel, C. A., Hall, S. R. R., Schmid, R. A., Guenat, O. T. & Geiser, T. Primary Human Lung Pericytes Support and Stabilize In Vitro Perfusable Microvessels. *Tissue Eng. Part A* **21,** 2166–2176 (2015).

72. Whisler, J. A., Chen, M. B. & Kamm, R. D. Control of perfusable microvascular network morphology using a multiculture microfluidic system. *Tissue Eng. Part C. Methods* **20,** 543–52 (2014).

73. Diaz-Santana, A., Shan, M. & Stroock, A. D. Endothelial cell dynamics during anastomosis in vitro. *Integr. Biol.* **7,** 454–466 (2015).

74. Rhodin, J. A. G., Rhodin & G., J. A. in *Comprehensive Physiology* 1–31 (John Wiley & Sons, Inc., 1980). doi:10.1002/cphy.cp020201

75. Augustin, H. G., Kozian, D. H. & Johnson, R. C. Differentiation of endothelial cells: Analysis of the constitutive and activated endothelial cell phenotypes. *BioEssays* **16,**

901–906 (1994).

76. Aird, W. C. Phenotypic Heterogeneity of the Endothelium: I. Structure, Function, and Mechanisms. *Circ. Res.* **100,** 158–173 (2007).

77. Chi, J.-T. *et al.* Endothelial cell diversity revealed by global expression profiling. *Proc. Natl. Acad. Sci. U. S. A.* **100,** 10623–8 (2003).

78. Nolan, D. J. *et al.* Molecular Signatures of Tissue-Specific Microvascular Endothelial Cell Heterogeneity in Organ Maintenance and Regeneration. *Dev. Cell* **26,** 204–219 (2013).

79. Cines, D. B. *et al.* Endothelial cells in physiology and in the pathophysiology of vascular disorders. *Blood* **91,** 3527–61 (1998).

80. Ala, A., Dhillon, A. P. & Hodgson, H. J. Role of cell adhesion molecules in leukocyte recruitment in the liver and gut. *Int. J. Exp. Pathol.* **84,** 1–16 (2003).

81. Bodnar, R. J., Rodgers, M. E., Chen, W. C. W. & Wells, A. Pericyte Regulation of Vascular Remodeling Through the CXC Receptor 3. *Arterioscler. Thromb. Vasc. Biol.* **33,** 2818–2829 (2013).

82. Rohringer, S. *et al.* Mechanisms of vasculogenesis in 3D fibrin matrices mediated by the interaction of adipose-derived stem cells and endothelial cells. *Angiogenesis* **17,** 921–933 (2014).

83. Jaffe, E. A., Nachman, R. L., Becker, C. G. & Minick, C. R. Culture of Human Endothelial Cells Derived from Umbilical Veins. IDENTIFICATION BY MORPHOLOGIC AND IMMUNOLOGIC CRITERIA. *J. Clin. Invest.* **52,** 2745–2756 (1973).

84. Katt, M. E., Xu, Z. S., Gerecht, S. & Searson, P. C. Human Brain Microvascular Endothelial Cells Derived from the BC1 iPS Cell Line Exhibit a Blood-Brain Barrier Phenotype. *PLoS One* **11,** e0152105 (2016).

85. Sobrino, A. *et al.* 3D microtumors in vitro supported by perfused vascular networks. *Sci. Rep.* **6,** 31589 (2016).

86. Barreto-Ortiz, S. F. *et al.* A Novel In Vitro Model for Microvasculature Reveals Regulation of Circumferential ECM Organization by Curvature. *PLoS One* **8,** e81061 (2013).

87. Sun, W. *et al.* Co-culture of outgrowth endothelial cells with human mesenchymal stem cells in silk fibroin hydrogels promotes angiogenesis. *Biomed. Mater.* **11,** 35009 (2016).

88. Arulmoli, J. *et al.* Combination scaffolds of salmon fibrin, hyaluronic acid, and laminin for human neural stem cell and vascular tissue engineering. *Acta Biomater.* (2016). doi:10.1016/j.actbio.2016.07.043

89. Hanjaya-Putra, D. *et al.* Controlled activation of morphogenesis to generate a functional human microvasculature in a synthetic matrix. *Blood* **118,** 804–815

(2011).

90. Sasagawa, T., Shimizu, T., Yamato, M. & Okano, T. Endothelial colony-forming cells for preparing prevascular three-dimensional cell-dense tissues using cell-sheet engineering. *J. Tissue Eng. Regen. Med.* n/a-n/a (2013). doi:10.1002/term.1858

91. Belair, D. G., Schwartz, M. P., Knudsen, T. & Murphy, W. L. Human iPSC-derived endothelial cell sprouting assay in synthetic hydrogel arrays. *Acta Biomater.* **39,** 12–24 (2016).

92. Ii, M. in *Methods in molecular biology (Clifton, N.J.)* **660,** 9–27 (2010).

93. Mead, L. E., Prater, D., Yoder, M. C. & Ingram, D. A. in *Current Protocols in Stem Cell Biology* **Chapter 2,** Unit 2C.1 (John Wiley & Sons, Inc., 2008).

94. Zhou, T. *et al.* Generation of human induced pluripotent stem cells from urine samples. *Nat. Protoc.* **7,** 2080–2089 (2012).

95. Park, I.-H., Lerou, P. H., Zhao, R., Huo, H. & Daley, G. Q. Generation of human-induced pluripotent stem cells. *Nat. Protoc.* **3,** 1180–1186 (2008).

96. Wilson, H. K., Canfield, S. G., Shusta, E. V & Palecek, S. P. Concise review: tissue-specific microvascular endothelial cells derived from human pluripotent stem cells. *Stem Cells* **32,** 3037–45 (2014).

97. Durr, E. *et al.* Direct proteomic mapping of the lung microvascular endothelial cell surface in vivo and in cell culture. *Nat. Biotechnol.* **22,** 985–992 (2004).

98. Milici, A. J., Furie, M. B. & Carley, W. W. The formation of fenestrations and channels by capillary endothelium in vitro. *Proc. Natl. Acad. Sci. U. S. A.* **82,** 6181–5 (1985).

99. Stolz, D. B. & Jacobson, B. S. Macro- and microvascular endothelial cells in vitro: maintenance of biochemical heterogeneity despite loss of ultrastructural characteristics. *In Vitro Cell. Dev. Biol.* **27A,** 169–82 (1991).

100. Geevarghese, A. & Herman, I. M. Pericyte-endothelial crosstalk: implications and opportunities for advanced cellular therapies. *Transl. Res.* **163,** 296–306 (2014).

101. Shepro, D. & Morel, N. M. Pericyte physiology. *FASEB J.* **7,** 1031–8 (1993).

102. Sims, D. E. & Westfall, J. A. Analysis of relationships between pericytes and gas exchange capillaries in neonatal and mature bovine lungs. *Microvasc. Res.* **25,** 333–42 (1983).

103. Sims, D. E. Recent advances in pericyte biology--implications for health and disease. *Can. J. Cardiol.* **7,** 431–43 (1991).

104. Bergers, G. & Song, S. The role of pericytes in blood-vessel formation and maintenance. *Neuro. Oncol.* **7,** 452–464 (2005).

105. Díaz-Flores, L. *et al.* Pericytes. Morphofunction, interactions and pathology in a

quiescent and activated mesenchymal cell niche. *Histol. Histopathol.* **24,** 909–69 (2009).

106. Ribatti, D., Nico, B. & Crivellato, E. The role of pericytes in angiogenesis. *Int. J. Dev. Biol.* **55,** 261–268 (2011).

107. Barreto-Ortiz, S. F. *et al.* Fabrication of 3-dimensional multicellular microvascular structures. *FASEB J.* **29,** 3302–3314 (2015).

108. Waters, J. P. *et al.* In vitro Self-Assembly of Human Pericyte-Supported Endothelial Microvessels in Three-Dimensional Coculture: A Simple Model for Interrogating Endothelial-Pericyte Interactions. *J. Vasc. Res.* **50,** 324–331 (2013).

109. Andrejecsk, J. W. *et al.* Paracrine exchanges of molecular signals between alginate-encapsulated pericytes and freely suspended endothelial cells within a 3D protein gel. *Biomaterials* **34,** 8899–8908 (2013).

110. Sarveswaran, K. *et al.* Synthetic Capillaries to Control Microscopic Blood Flow. *Sci. Rep.* **6,** 21885 (2016).

111. van der Meer, A. D., Orlova, V. V, ten Dijke, P., van den Berg, A. & Mummery, C. L. Three-dimensional co-cultures of human endothelial cells and embryonic stem cell-derived pericytes inside a microfluidic device. *Lab Chip* **13,** 3562–3568 (2013).

112. Wang, G., Jacquet, L., Karamariti, E. & Xu, Q. Origin and differentiation of vascular smooth muscle cells. *J. Physiol.* **593,** 3013–3030 (2015).

113. Rensen, S. S. M., Doevendans, P. A. F. M. & van Eys, G. J. J. M. Regulation and characteristics of vascular smooth muscle cell phenotypic diversity. *Neth. Heart J.* **15,** 100–8 (2007).

114. Gartner, L. P. *Textbook of histology.*

115. Michel, J.-B., Li, Z. & Lacolley, P. Smooth muscle cells and vascular diseases. doi:10.1093/cvr/cvs172

116. Liu, Y. *et al.* Engineering tissues with a perfusable vessel-like network using endothelialized alginate hydrogel fiber and spheroid-enclosing microcapsules. *Heliyon* **2,** e00067 (2016).

117. Yoshida, H., Matsusaki, M. & Akashi, M. Multilayered Blood Capillary Analogs in Biodegradable Hydrogels for In Vitro Drug Permeability Assays. *Adv. Funct. Mater.* **23,** 1736–1742 (2013).

118. Slany, A. *et al.* Plasticity of fibroblasts demonstrated by tissue-specific and function-related proteome profiling. *Clin. Proteomics* **11,** 41 (2014).

119. Chang, H. Y. *et al.* Diversity, topographic differentiation, and positional memory in human fibroblasts. *Proc. Natl. Acad. Sci. U. S. A.* **99,** 12877–82 (2002).

120. Rodemann, H. P. & Rennekampff, H.-O. in *Tumor-Associated Fibroblasts and their*

Matrix 23–36 (Springer Netherlands, 2011). doi:10.1007/978-94-007-0659-0_2

121. Alberts, B. *et al. Molecular biology of the cell.* (Garland Science, 2002).

122. Abercrombie, M. Fibroblasts. *J. Clin. Pathol. Suppl. (R. Coll. Pathol).* **12,** 1–6 (1978).

123. Shiga, K. *et al.* Cancer-Associated Fibroblasts: Their Characteristics and Their Roles in Tumor Growth. *Cancers (Basel).* **7,** 2443–2458 (2015).

124. McAnulty, R. J. Fibroblasts and myofibroblasts: Their source, function and role in disease. *Int. J. Biochem. Cell Biol.* **39,** 666–671 (2007).

125. Griffith, C. K. *et al.* Diffusion Limits of an *in Vitro* Thick Prevascularized Tissue. *Tissue Eng.* **11,** 257–266 (2005).

126. Newman, A. C., Nakatsu, M. N., Chou, W., Gershon, P. D. & Hughes, C. C. W. The requirement for fibroblasts in angiogenesis: fibroblast-derived matrix proteins are essential for endothelial cell lumen formation. *Mol. Biol. Cell* **22,** 3791–3800 (2011).

127. Rinn, J. L., Bondre, C., Gladstone, H. B., Brown, P. O. & Chang, H. Y. Anatomic Demarcation by Positional Variation in Fibroblast Gene Expression Programs. *PLoS Genet.* **2,** e119 (2006).

128. Kim, J. *et al.* Engineering of a Biomimetic Pericyte-Covered 3D Microvascular Network. *PLoS One* **10,** e0133880 (2015).

129. Shamis, Y. *et al.* Fibroblasts Derived from Human Pluripotent Stem Cells Activate Angiogenic Responses In Vitro and In Vivo. *PLoS One* **8,** e83755 (2013).

130. Hematti, P. Mesenchymal stromal cells and fibroblasts: a case of mistaken identity? *Cytotherapy* **14,** 516–521 (2012).

131. Haniffa, M. A., Collin, M. P., Buckley, C. D. & Dazzi, F. Mesenchymal stem cells: the fibroblasts' new clothes? *Haematologica* **94,** 258–263 (2009).

132. Kalluri, R. The biology and function of fibroblasts in cancer. *Nat. Rev. Cancer* **16,** 582–598 (2016).

133. Ghajar, C. M. *et al.* The effect of matrix density on the regulation of 3-D capillary morphogenesis. *Biophys. J.* **94,** 1930–41 (2008).

134. Cox, T. R. & Erler, J. T. Remodeling and homeostasis of the extracellular matrix: implications for fibrotic diseases and cancer. *Dis. Model. Mech.* **4,** 165–178 (2011).

135. Edgar, L. T., Underwood, C. J., Guilkey, J. E., Hoying, J. B. & Weiss, J. A. Extracellular matrix density regulates the rate of neovessel growth and branching in sprouting angiogenesis. *PLoS One* **9,** e85178 (2014).

136. Boyd, N. L. *et al.* Dissecting the Role of Human Embryonic Stem Cell–Derived Mesenchymal Cells in Human Umbilical Vein Endothelial Cell Network Stabilization in Three-Dimensional Environments. *Tissue Eng. Part A* **19,** 211–223 (2012).

137. Rao, R. R., Peterson, A. W., Ceccarelli, J., Putnam, A. J. & Stegemann, J. P. Matrix composition regulates three-dimensional network formation by endothelial cells and mesenchymal stem cells in collagen/fibrin materials. *Angiogenesis* **15,** 253–264 (2012).

138. Yamamura, N., Sudo, R., Ikeda, M. & Tanishita, K. Effects of the Mechanical Properties of Collagen Gel on the *In Vitro* Formation of Microvessel Networks by Endothelial Cells. *Tissue Eng.* **13,** 1443–1453 (2007).

139. Huynh, J. *et al.* Age-Related Intimal Stiffening Enhances Endothelial Permeability and Leukocyte Transmigration. *Sci. Transl. Med.* **3,** (2011).

140. Krishnan, R. *et al.* Substrate stiffening promotes endothelial monolayer disruption through enhanced physical forces. *Am. J. Physiol. Cell Physiol.* **300,** C146-54 (2011).

141. Lesman, A. *et al.* Engineering vessel-like networks within multicellular fibrin-based constructs. *Biomaterials* **32,** 7856–7869 (2011).

142. Rao, R. R. *et al.* Effects of hydroxyapatite on endothelial network formation in collagen/fibrin composite hydrogels in vitro and in vivo. *Acta Biomater.* **10,** 3091–3097 (2014).

143. Singh, R. K., Seliktar, D. & Putnam, A. J. Capillary morphogenesis in PEG-collagen hydrogels. *Biomaterials* **34,** 9331–9340 (2013).

144. Senger, D. R. & Davis, G. E. Angiogenesis. *Cold Spring Harb. Perspect. Biol.* **3,** a005090–a005090 (2011).

145. Yurchenco, P. D. Basement membranes: cell scaffoldings and signaling platforms. *Cold Spring Harb. Perspect. Biol.* **3,** a004911 (2011).

146. M, M. P. Basement Membrane Proteins: Structure, Assembly, and Cellular Interactions. *Crit. Rev. Biochem. Mol. Biol.* **27,** 93–127 (1992).

147. Davis, G. E. & Senger, D. R. Endothelial Extracellular Matrix: Biosynthesis, Remodeling, and Functions During Vascular Morphogenesis and Neovessel Stabilization. *Circ. Res.* **97,** 1093–1107 (2005).

148. Timpl, R. Structure and biological activity of basement membrane proteins. *Eur J Biochem* **180,** 487–5502 (1989).

149. Kalluri, R. Angiogenesis: Basement membranes: structure, assembly and role in tumour angiogenesis. *Nat. Rev. Cancer* **3,** 422–433 (2003).

150. Han, S. *et al.* Constructive remodeling of a synthetic endothelial extracellular matrix. *Sci. Rep.* **5,** 18290 (2015).

151. Stratman, A. N. & Davis, G. E. Endothelial Cell-Pericyte Interactions Stimulate Basement Membrane Matrix Assembly: Influence on Vascular Tube Remodeling, Maturation, and Stabilization. *Microsc. Microanal.* **18,** 68–80 (2012).

152. LAURENS, N., KOOLWIJK, P. & DE MAAT, M. P. M. Fibrin structure and wound healing. *J. Thromb. Haemost.* **4,** 932–939 (2006).

153. Yancopoulos, G. D. *et al.* Vascular-specific growth factors and blood vessel formation. *Nature* **407,** 242–248 (2000).

154. Stratman, A. N., Davis, M. J. & Davis, G. E. VEGF and FGF prime vascular tube morphogenesis and sprouting directed by hematopoietic stem cell cytokines. *Blood* (2011).

155. Nicosia, R. F. & Ottinetti, A. Growth of microvessels in serum-free matrix culture of rat aorta. A quantitative assay of angiogenesis in vitro. *Lab. Invest.* **63,** 115–22 (1990).

156. Welch-Reardon, K. M. *et al.* Angiogenic sprouting is regulated by endothelial cell expression of Slug. *J. Cell Sci.* **127,** 2017–28 (2014).

157. Lim, S. H., Kim, C., Aref, A. R., Kamm, R. D. & Raghunath, M. Complementary effects of ciclopirox olamine, a prolyl hydroxylase inhibitor and sphingosine 1-phosphate on fibroblasts and endothelial cells in driving capillary sprouting. *Integr. Biol. Quant. Biosci. from Nano to Macro* **5,** 1474–1484 (2013).

158. Bersini, S. *et al.* Human in vitro 3D co-culture model to engineer vascularized bone-mimicking tissues combining computational tools and statistical experimental approach. *Biomaterials* **76,** 157–172 (2016).

159. Jeon, J. S. *et al.* Human 3D vascularized organotypic microfluidic assays to study breast cancer cell extravasation. *Proc. Natl. Acad. Sci.* **112,** 214–219 (2015).

160. Stoehr, A. *et al.* Spontaneous Formation of Extensive Vessel-Like Structures in Murine Engineered Heart Tissue. *Tissue Eng. Part A* **22,** 326–335 (2016).

161. Sekiya, S., Shimizu, T. & Okano, T. Vascularization in 3D tissue using cell sheet technology. *Regen. Med.* **8,** 371–377 (2013).

162. Levenberg, S. *et al.* Engineering vascularized skeletal muscle tissue. *Nat. Biotechnol.* **23,** 879–884 (2005).

163. Sasagawa, T. *et al.* Design of prevascularized three-dimensional cell-dense tissues using a cell sheet stacking manipulation technology. *Biomaterials* **31,** 1646–1654 (2010).

164. Kaufman-Francis, K., Koffler, J., Weinberg, N., Dor, Y. & Levenberg, S. Engineered Vascular Beds Provide Key Signals to Pancreatic Hormone-Producing Cells. *PLoS One* **7,** e40741 (2012).

165. Lee, H., Park, W., Ryu, H. & Jeon, N. L. A microfluidic platform for quantitative analysis of cancer angiogenesis and intravasation. *Biomicrofluidics* **8,** 54102 (2014).

166. Kinstlinger, I. S. & Miller, J. S. 3D-printed fluidic networks as vasculature for engineered tissue. *Lab Chip* **16,** 2025–2043 (2016).

167. Heintz, K. A. *et al.* Fabrication of 3D Biomimetic Microfluidic Networks in Hydrogels. *Adv. Healthc. Mater.* (2016). doi:10.1002/adhm.201600351

168. Kolesky, D. B., Homan, K. A., Skylar-Scott, M. A. & Lewis, J. A. Three-dimensional bioprinting of thick vascularized tissues. *Proc. Natl. Acad. Sci. U. S. A.* **113,** 3179–84 (2016).

169. Zheng, Y., Chen, J. & López, J. A. Flow-driven assembly of VWF fibres and webs in in vitro microvessels. *Nat. Commun.* **6,** 7858 (2015).

170. Bai, J. *et al.* Identification of drugs as single agents or in combination to prevent carcinoma dissemination in a microfluidic 3D environment. *Oncotarget* **6,** 36603–36614 (2015).

171. Phan, D. T. T. *et al.* A vascularized and perfused organ-on-a-chip platform for large-scale drug screening applications. *Lab Chip* **17,** 511–520 (2017).

172. Ma, J. *et al. In vitro* and *in vivo* angiogenic capacity of BM-MSCs/HUVECs and AT-MSCs/HUVECs cocultures. *Biofabrication* **6,** 15005 (2014).

173. Lamah, M., Mortimer, P. S. & Dormandy, J. A. Quantitative study of capillary density in the skin of the foot in peripheral vascular disease. *Br. J. Surg.* **86,** 342–348 (1999).

174. Kampschulte, M. *et al.* Quantitative 3D Micro-CT Imaging of Human Lung Tissue. *RöFo - Fortschritte auf dem Gebiet der Röntgenstrahlen und der Bildgeb. Verfahren* **185,** 869–876 (2013).

175. Krogh, A. The number and distribution of capillaries in muscles with calculations of the oxygen pressure head necessary for supplying the tissue. *J. Physiol.* **52,** 409–415 (1919).

176. Khansari, M. M. *et al.* Assessment of Conjunctival Microvascular Hemodynamics in Stages of Diabetic Microvasculopathy. *Sci. Rep.* **7,** 45916 (2017).

177. Chiu, J.-J. & Chien, S. Effects of disturbed flow on vascular endothelium: pathophysiological basis and clinical perspectives. *Physiol. Rev.* **91,** 327–87 (2011).

178. Miles, F. L., Pruitt, F. L., van Golen, K. L. & Cooper, C. R. Stepping out of the flow: capillary extravasation in cancer metastasis. *Clin. Exp. Metastasis* **25,** 305–324 (2008).

179. Price, G. M. & Tien, J. in *Methods in molecular biology (Clifton, N.J.)* **671,** 281–293 (2011).

180. Yuan, W., Lv, Y., Zeng, M. & Fu, B. M. Non-invasive measurement of solute permeability in cerebral microvessels of the rat. *Microvasc. Res.* **77,** 166–173 (2009).

181. Sudo, R. *et al.* Transport-mediated angiogenesis in 3D epithelial coculture. *FASEB J.* **23,** 2155–2164 (2009).

182. Costa-Almeida, R. *et al.* Fibroblast-Endothelial Partners for Vascularization Strategies

in Tissue Engineering. *Tissue Eng. Part A* **21,** 1055–1065 (2015).

183. Wells, R. G. The Role of Matrix Stiffness in Regulating Cell Behavior. doi:10.1002/hep.22193

184. Eroshenko, N., Ramachandran, R., Yadavalli, V. K. & Rao, R. R. Effect of substrate stiffness on early human embryonic stem cell differentiation. *J. Biol. Eng.* **7,** 7 (2013).

185. Gautier, H. O. B. *et al.* Chapter 12 - Atomic force microscopy-based force measurements on animal cells and tissues. *Methods Cell Biol.* **125,** 211–235 (2015).

186. Lin, D. C., Dimitriadis, E. K. & Horkay, F. Robust Strategies for Automated AFM Force Curve Analysis—I. Non-adhesive Indentation of Soft, Inhomogeneous Materials. *J. Biomech. Eng.* **129,** 430 (2007).

187. Moeendarbary, E. *et al.* The soft mechanical signature of glial scars in the central nervous system. *Nat. Commun.* **8,** 14787 (2017).

188. Duong, H., Wu, B. & Tawil, B. Modulation of 3D fibrin matrix stiffness by intrinsic fibrinogen-thrombin compositions and by extrinsic cellular activity. *Tissue Eng. Part A* **15,** 1865–76 (2009).

189. Arike, L. *et al.* Comparison and applications of label-free absolute proteome quantification methods on Escherichia coli. *J. Proteomics* **75,** 5437–5448 (2012).

190. Grossmann, J. *et al.* Implementation and evaluation of relative and absolute quantification in shotgun proteomics with label-free methods. *J. Proteomics* **73,** 1740–1746 (2010).

191. Robinson, B. K., Cortes, E., Rice, A. J., Sarper, M. & del Río Hernández, A. Quantitative analysis of 3D extracellular matrix remodelling by pancreatic stellate cells. *Biol. Open* (2016).

192. Mohammadi, H., Arora, P. D., Simmons, C. A., Janmey, P. A. & McCulloch, C. A. Inelastic behaviour of collagen networks in cell-matrix interactions and mechanosensation. *J. R. Soc. Interface* **12,** 20141074–20141074 (2014).

193. Naba, A., Clauser, K. R. & Hynes, R. O. Enrichment of Extracellular Matrix Proteins from Tissues and Digestion into Peptides for Mass Spectrometry Analysis. *J. Vis. Exp.* e53057–e53057 (2015). doi:10.3791/53057

194. Naba, A. *et al.* The Matrisome: *In Silico* Definition and *In Vivo* Characterization by Proteomics of Normal and Tumor Extracellular Matrices. *Mol. Cell. Proteomics* **11,** M111.014647 (2012).

195. Lilly, B. & Kennard, S. Differential gene expression in a coculture model of angiogenesis reveals modulation of select pathways and a role for Notch signaling. *Physiol. Genomics* **36,** 69–78 (2008).

196. Ringnér, M. What is principal component analysis? *Nat. Biotechnol.* **26,** 303–304 (2008).

197. Soumillon, M., Cacchiarelli, D., Semrau, S., van Oudenaarden, A. & Mikkelsen, T. S. Characterization of directed differentiation by high-throughput single-cell RNA-Seq. *bioRxiv* (2014).

198. Love, M. I., Huber, W. & Anders, S. Moderated estimation of fold change and dispersion for RNA-seq data with DESeq2. *Genome Biol.* **15,** 550 (2014).

199. Cook, R. D. Detection of Influential Observation in Linear Regression. *Technometrics* **19,** 15–18 (1977).

200. Benjamini, Y. & Hochberg, Y. Controlling the False Discovery Rate: A Practical and Powerful Approach to Multiple Testing. *Source J. R. Stat. Soc. Ser. B* **57,** 289–300 (1995).

201. Baeyens, N. & Schwartz, M. A. Biomechanics of vascular mechanosensation and remodeling. *Mol. Biol. Cell* **27,** 7–11 (2016).

202. Olabisi, R. M. Cell microencapsulation with synthetic polymers. *J. Biomed. Mater. Res. A* **103,** 846–59 (2015).

203. Gasperini, L., Mano, J. F. & Reis, R. L. Natural polymers for the microencapsulation of cells. *J. R. Soc. Interface* **11,** 20140817–20140817 (2014).